PL-TR-96-2271

RESEARCH ON SEISMIC MONITORING AT REGIONAL DISTANCES

W. Dong
R. L. Gibson, Jr.
M. G. Imhof
M. N. Toksöz

Earth Resources Laboratory
Department of Earth, Atmospheric, and
 Planetary Sciences
Massachusetts Institute of Technology
Cambridge, MA 02139

15 October 1996

Scientific Report No. 1

Approved for Public Release; Distribution Unlimited

PHILLIPS LABORATORY
Directorate of Geophysics
AIR FORCE MATERIEL COMMAND
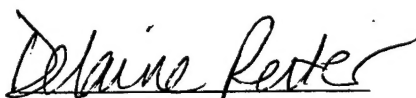**HANSCOM AFB, MA 01731-3010**

19970224 095

SPONSORED BY
Air Force Technical Applications Center
Directorate of Nuclear Treaty Monitoring
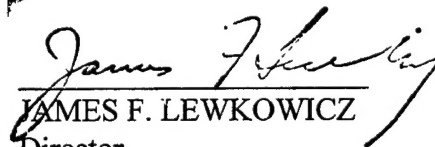Project Authorization T/5101

MONITORED BY
Phillips Laboratory
CONTRACT No. F19628-95-C-0091

The views and conclusions contained in this document are those of the authors and should not be interpreted as representing the official policies, either express or implied, of the Air Force or U.S. Government.

This technical report has been reviewed and is approved for publication.

DELAINE REITER
Contract Manager
Earth Sciences Division

JAMES F. LEWKOWICZ
Director
Earth Sciences Division

This report has been reviewed by the ESD Public Affairs Office (PA) and is releasable to the National Technical Information Service (NTIS).

Qualified requestors may obtain copies from the Defense Technical Information Center. All others should apply to the National Technical Information Service.

If your address has changed, or you wish to be removed from the mailing list, or if the addressee is no longer employed by your organization, please notify PL/IM, 29 Randolph Road, Hanscom AFB, MA 01731-3010. This will assist us in maintaining a current mailing list.

Do not return copies of this report unless contractual obligations or notices on a specific document requires that it be returned.

REPORT DOCUMENTATION PAGE

1. AGENCY USE ONLY (Leave blank)	2. REPORT DATE 15 OCT 1996	3. REPORT TYPE AND DATES COVERED Scientific No. 1

4. TITLE AND SUBTITLE

Research on Seismic Monitoring at Regional Distances

5. FUNDING NUMBERS

F19628-95-C-0091
PE35999F
PR5101
TAGM
WUAI

6. AUTHOR(S)

Wenjie Dong   M. Nafi Toksöz
Richard L. Gibson, Jr.
Matthias G. Imhof

7. PERFORMING ORGANIZATION NAME(S) AND ADDRESS(ES)

Earth Resources Laboratory
Dept. of Earth, Atmospheric, and Planetary Sciences
Massachusetts Institute of Technology
42 Carleton Street
Cambridge, MA 02142

8. PERFORMING ORGANIZATION REPORT NUMBER

63575

9. SPONSORING / MONITORING AGENCY NAME(S) AND ADDRESS(ES)

Phillips Laboratory
29 Randolph Rd.
Hanscom AFB, MA 01731-3010

Contract Manager: Delaine Reiter /GPE

10. SPONSORING / MONITORING AGENCY REPORT NUMBER

PL-TR-96-2271

11. SUPPLEMENTARY NOTES

12a. DISTRIBUTION / AVAILABILITY STATEMENT

Approved for Public Release; Distribution Unlimited

12b. DISTRIBUTION CODE

13. ABSTRACT (Maximum 200 words)

We report two studies related to numerical modeling of seismic wave generation and propagation. In the first, numerical calculations of seismic wave scattering using the multiple multipole technique are compared to laboratory data that we collected in an ultrasonic experiment. The results demonstrate the validity of the multiple multipole approach for seismic wave propagation modeling. The second study investigates seismic radiation from explosively loaded cavities in isotropic and transversely isotropic media. Theoretical calculations of source radiation patterns show that small, decoupled explosions in cylindrical cavities will generate shear waves with amplitude depending on cavity shape (ratio of length to width). The calculations also show the interesting result that locating such a cavity in transversely isotropic media can, in special cases, actually produce less shear wave energy than in an isotropic medium.

14. SUBJECT TERMS

Seismic wave scattering, multipole expansions, nonspherical explosion cavities, nuclear discrimination

15. NUMBER OF PAGES

86

16. PRICE CODE

17. SECURITY CLASSIFICATION OF REPORT	18. SECURITY CLASSIFICATION OF THIS PAGE	19. SECURITY CLASSIFICATION OF ABSTRACT	20. LIMITATION OF ABSTRACT
UNCLASSIFIED	UNCLASSIFIED	UNCLASSIFIED	SAR

TABLE OF CONTENTS

List of Contributing Scientists

Wenjie Dong, Research Scientist, Mobil E&P Technical Center, Dallas, Texas
Richard L. Gibson, Research Scientist, Massachusetts Institute of Technology
Matthias G. Imhof, Postdoctoral Associate, Massachusetts Institute of Technology
M. Nafi Toksöz, Professor of Geophysics, Massachusetts Institute of Technology

List of Previous and Related Contracts

Bibliography of Publications Totally or Partially Sponsored by the Contract

Gibson, R.L., Jr., M.N. Toksöz, and W. Dong, Seismic radiation from explosively loaded cavities in isotropic and transversely isotropic media, accepted by *Bull. Seism. Soc. Am.*,

Gibson, R.L., Jr., M.N. Toksöz, and W. Dong, 1995, Seismic sources and wave propagation in 3-D: Radiation from cylindrical cavities, *Proceedings of the 17th Ann. Seismic Research Symp.*, Scottsdale, AZ, Air Force Phillips Laboratory.

Imhof, M.G. and M.N. Toksöz, 1996, Seismo-acoustic multiple scattering: A comparison of multiple multipole expansions with an ultrasonic experiment, submitted to *J. Acoust. Soc. Am.*

Nolte, B., R.L. Gibson, Jr., and M.N. Toksöz, 1996, Irregular-grid modeling of regional wave propagation, *Proceedings of the 17th Ann. Seismic Research Symp.*, Anapolis, MD, Air Force Phillips Laboratory.

PREFACE

The work we report here has two primary objectives. The first goal is to develop methods for modeling regional wave propagation in laterally varying media, and the second is to develop numerical and theoretical models for radiation of elastic waves from explosion sources. Our report includes a preprint entitled "Seismo-acoustic multiple scattering: A comparison of multiple multipole expansions with an ultrasonic experiment," which has been submitted to the *Journal of the Acoustical Society of America*. This work presents a calibration of the multiple multipole technique with laboratory data that we collected, and demonstrates the validity of the approach. Potential applications include the modeling of path scattering effects on regional seismograms and the effects of heterogeneity in the vicinity of the source. The second section of this report is a preprint of the paper "Seismic radiation from explosively loaded cavities in isotropic and transversely isotropic media," accepted for publication in the *Bulletin of the Seismological Society of America*. It demonstrates that small, decoupled explosions in cylindrical cavities will generate shear waves with amplitude depending on cavity shape (ratio of length to width). In addition, we present the interesting result that locating such a cavity in transversely isotropic media can, in special cases, actually produce *less* shear wave energy than in an isotopic medium.

Acousto-Elastic Multiple Scattering: A Comparison of Ultrasonic Experiments With Multiple Multipole Expansions *

Matthias G. Imhof and M. Nafi Toksöz

Earth Resources Laboratory

Department of Earth, Atmospheric, and Planetary Sciences

Massachusetts Institute of Technology

Cambridge, MA 02139

1

Abstract

The wavefield scattered from only three solid rods submerged in water is very complex. Although the major events can readily be interpreted as direct reflections, the remaining wavefield consists of complicated interactions of the wavefields with the scatterers and the water surface. Forward modelling of the situation is a viable interpretative aid, especially if the method decomposes the wavefields by their respective origins. Multiple multipole expansions have already been used as a versatile tool to model acoustic or elastic multiple scattering problems where homogeneous scatterers were embedded in a homogeneous fullspace. In the present paper, the scheme is expanded to multiple scattering between solids submerged in a fluid. For each scatterer, the waves induced in the fluid are expressed by sets of multipole solutions with different origins. Thus by construction, the scattered wavefields are decomposed by scatterer. Ultrasonic experiments are performed for two different geometries of three submerged rods. To aid the interpretation of the results, the experiments are numerically modelled by the multiple multipoles method.

Introduction

The scattering of acoustic waves from solids submerged in a fluid has received well deserved attention for a long time (Everstine and Au-Yang, 1984; Junger and Feit, 1986). Even for very simple cases, the scattered wavefields become very complex. For example, in the case of several submerged solid objects, the major events can readily be interpreted as direct reflections. However, the remaining wavefield consists of complicated interactions of the wavefields with the scatterers and the water surface. Forward modelling of the situation is a valuable aid to understand these interacting events better. Especially useful are methods which decompose the scattered wavefields by their origin. Thus, forward modelling schemes such as the finite differences method have to be discarded as interpretative tools because they

only yield the total wavefields. Various other methods have been applied. For a few simple geometries, analytic solutions are available, e.g. cylindrical objects (Pao and Mow, 1973). For more complicated geometries, other methods have been used: integral equations (de Hoop, 1990; Luke and Martin, 1995), the T-matrix (Boström, 1980), perturbation schemes (Norris, 1990), or boundary element methods (Jensen *et al.*, 1994) which might be coupled to finite elements (Mathews, 1986; Everstine and Henderson, 1990; Fyfe *et al.*, 1991).

Multiple multipole expansions (MMP) have already been shown to be a versatile tool to solve scattering problems in fluids (Imhof, 1995a) or solids (Imhof, 1995b). In either case, homogeneous scatterers were embedded in a homogeneous fullspace. In the present paper, a combination of the acoustic with the elastic scheme is introduced as an interpretative aid to multiple scattering between solids submerged in a fluid. There are various reasons to use MMP expansions. First, they have been shown to converge faster than more traditional methods (Imhof, 1995a,b). The resulting scheme is very naturally applied to situations of multiple scattering objects. Most important, the scattered fields are by construction decomposed by scatterer. Although we will not exploit it, the wavefield in each solid scatterer is also decomposed into P- and S-waves.

The paper is structured as follows. In an ultrasonic watertank, we measure the scattering between three rods of lucite and the water surface. Even though the situation is rather simple, we find the scattered field to contain complex interactions between the rods and the surface. To aid the interpretation, we derive the acousto-elastic MMP scheme which we use to model the two ultrasonic experiments. A comparison of the experimental and numerical data not only validates the acousto-elastic scheme but also explains various events as internal multiples in the rods or reverberations between the scatterers and the water surface. The numerical data also identifies some events as reflections being diffracted by the other scatterers.

3

Ultrasonic Modelling

A simple fluid-solid scattering experiment is performed in an ultrasonic watertank. Three rods of lucite are submerged in the tank. Two different geometries are used. The first shown in Figure 1 resembles a syncline structure. The second geometry resembles an anticline shown in Figure 2. For both geometries, an acoustic source is placed above the rods. Receivers placed along a line perpendicular to the rods measure the signals reflected from the rods. Although the ultrasonic tank is of finite dimensions ($100 \times 60 \times 50$ cm), the experiment is designed that reflections from the sides and the bottom of the tank are outside the time window of interest. The tank is equipped with a PC-based control and data acquisition system. A schematic thereof is presented in Figure 3. Computer controlled holders allow movement of a source and a receiver along a prescribed path within the tank. For a fixed source - scatterer - receiver geometry, the computer controlled acquisition system allows to perform the same experiment a number of times to improve the signal-to-noise ratio. Without waveform averaging, the smaller events would vanish in the ambient noise which reaches the same amplitude level as the reflections.

Piezoelectric transducers act as source and receiver. The source (Panametrix V323) has a strong nonuniform vertical radiation pattern, as most of its energy is pointed vertically downward as expected from a vertical point force. The receiver (Panametrix V1091) has a receiver pattern very similar to the source radiation pattern. This source-receiver combination tends to emphasize waves propagating in the vertical direction and to suppress waves propagating in the horizontal direction.

The rods have a P-wave velocity $\alpha = 2570$ m/s, a S-wave velocity $\beta = 1200$ m/s, and a density ρ_s of 1180 kg/m^3. The P-wave velocity γ in the water is 1460 m/s, the density ρ_f is 1000 kg/m^3. The width of the first scatterer is 45 mm, the second 60 mm, and the third 30 mm. All scatterers are 20 mm thick. Exiting the source transducer with a sharp pulse, the transducer emits a wavelet of approximately 190 kHz center frequency shown in Figure 4. In

4

the water, the resulting dominant wavelength is around 6 mm. Thus, the scatters are 3 to 10 times larger than the propagating pulse which allows to discriminate between reflections from the top or bottom of the scatterers. The sampling interval is chosen to be 400 ns which yields a corresponding Nyquist frequency of 1.25 MHz. The cutoff-frequencies of the bandpass filter are set to 5 KHz, respectively 300 KHz. For each trace, 512 samples are recorded. The recording is delayed by 120 μs to mute the direct arrivals and to maximize the time window of interest. The traces are averaged over 2048 sweeps to reduce the noise amplitudes. The receiver transducer is placed at 75 different positions along a line perpendicular to the rods. The spacing between the receiver points is 5 mm. The source transducer is located in the center of the receiver spread at position 38.

Figure 5 shows the measured record for the syncline model defined in Figure 1. As expected for a syncline geometry, we obtain the typical butterfly pattern (Haartsen *et al.*, 1994). Figure 6 shows the measured record for the anticline model defined in Figure 2. For both geometries, the major events can readily be interpreted as direct reflections. But the remaining wavefields consist of complicated interactions of the wavefields with the scatterers and the water surface. Despite the simple geometries, it is not obvious how to interpret the different events. As a consequence, we resort to forward-modelling as an interpretative aid.

Theoretical Background

We need to model how the acoustic pulse described by the displacement $\mathbf{u}^{inc}(\mathbf{x}, \omega)$ propagating in the water scatters from submerged solids. To distinguish the different regions, we will use the symbol Γ^d. The fluid domain is denoted by Γ^0. Often, the fluid region will also be called 'background'. The three solid scatterers are denoted by Γ^1, Γ^2, and Γ^3. The boundary between the fluid Γ^0 and, e.g., the solid Γ^1 is denoted by $\partial\Gamma_{01}$.

In the frequency domain, the displacement $\mathbf{u}_f$ of a wave travelling in a two-dimensional,

5

homogeneous fluid is described by

$$\frac{1}{k_f^2}\nabla\nabla\cdot\mathbf{u}_f + \mathbf{u}_f = 0\,, \tag{1a}$$

where we defined the wave number $k_f = \omega/\gamma$ for a particular frequency ω and the propagation velocity γ. The fluid velocity can also be written as $\gamma = \sqrt{\lambda_f/\rho_f}$ where λ_f is the Lamé parameter and ρ_f the density of the fluid. Note that we suppress a common time factor $e^{i\omega t}$. Elastic P-SV waves $\mathbf{u}_s$ travelling in a two dimensional, homogeneous solid are described by

$$\frac{1}{k_s^2}\nabla\nabla\cdot\mathbf{u}_s - \frac{1}{l_s^2}\nabla\times\nabla\times\mathbf{u}_s + \mathbf{u}_s = 0\,, \tag{1b}$$

where we defined the wave numbers $k_s = \omega/\alpha$ and $l_s = \omega/\beta$ for a particular frequency ω and the propagation velocities $\alpha = \sqrt{\lambda_s + 2\mu_s/\rho_s}$ and $\beta = \sqrt{\mu_s/\rho_s}$. The parameter ρ_s, λ_s, and μ_s denote the density and the Lamé parameters of the medium.

Instead of working with the vector forms (1) of the wave equations, we will use the potentials $\Xi(\mathbf{x},\omega)$, $\Phi(\mathbf{x},\omega)$, and $\Psi(\mathbf{x},\omega) = \hat{\mathbf{y}}\Psi(\mathbf{x},\omega)$ which relate to the displacements $\mathbf{u}_f$ and $\mathbf{u}_s$ by

$$\mathbf{u}_f(\mathbf{x},\omega) = \mathbf{u}^\Xi(\mathbf{x},\omega) = \nabla\Xi(\mathbf{x},\omega)\,, \tag{2a}$$

$$\mathbf{u}_s(\mathbf{x},\omega) = \mathbf{u}^\Phi(\mathbf{x},\omega) + \mathbf{u}^\Psi(\mathbf{x},\omega) = \nabla\Phi(\mathbf{x},\omega) + \nabla\times\boldsymbol{\Psi}(\mathbf{x},\omega)\,. \tag{2b}$$

Each scalar potential itself satisfies a scalar wave equation:

$$\nabla^2\Xi(\mathbf{x},\omega) + k_f^2\Xi(\mathbf{x},\omega) = 0\,, \tag{3a}$$

$$\nabla^2\Phi(\mathbf{x},\omega) + k_s^2\Phi(\mathbf{x},\omega) = 0\,, \tag{3b}$$

$$\nabla^2\Psi(\mathbf{x},\omega) + l_s^2\Psi(\mathbf{x},\omega) = 0\,. \tag{3c}$$

Similar to the purely acoustic or elastic cases (Imhof, 1995a,b), we expand the potential

fields due to the $D = 3$ scatterers as

$$\Xi(\mathbf{x}, \omega) = \sum_{d=1}^{D} \sum_{p=1}^{P_d^{\Xi}} \sum_{n=-N_{pd}^{\Xi}}^{+N_{pd}^{\Xi}} a_{pnd} \cdot \xi_{pnd}(\mathbf{x}, \mathbf{x}_{pd}^{\Xi}, k_f) + e^{\Xi}, \tag{4a}$$

$$\Phi_d(\mathbf{x}, \omega) = \sum_{p=1}^{P_d^{\Phi}} \sum_{n=-N_{pd}^{\Phi}}^{+N_{pd}^{\Phi}} b_{pnd} \cdot \phi_{pnd}(\mathbf{x}, \mathbf{x}_{pd}^{\Phi}, k_s) + e_d^{\Phi}, \tag{4b}$$

$$\Psi_d(\mathbf{x}, \omega) = \sum_{p=1}^{P_d^{\Psi}} \sum_{n=-N_{pd}^{\Psi}}^{+N_{pd}^{\Psi}} c_{pnd} \cdot \psi_{pnd}(\mathbf{x}, \mathbf{x}_{pd}^{\Psi}, l_s) + e_d^{\Psi}, \tag{4c}$$

where the subscript $d \leq D$ denotes the index of the scatterer. The expansions $\xi_{pnd}(\mathbf{x}, \mathbf{x}_{pd}^{\Xi}, k_f)$, $\phi_{pnd}(\mathbf{x}, \mathbf{x}_{pd}^{\Phi}, k_s)$, and $\psi_{pnd}(\mathbf{x}, \mathbf{x}_{pd}^{\Psi}, l_s)$ are all solutions to their respective Helmholtz equations (3). For each scatterer d and each expansion, e.g. Φ, we choose a set of P_d^{Φ} expansion centers located at $\mathbf{x}_{pd}^{\Phi}$. At each expansion center $\mathbf{x}_{pd}^{\Phi}$, we place a multipole $\sum_n \phi_{pnd}(\mathbf{x}, \mathbf{x}_{pd}^{\Phi}, k_s)$ of order $-N_{pd} \leq n \leq +N_{pd}$. Because the maximal orders of the multipoles are finite and the resulting expansion is non-orthogonal, we also need to include an error term e_d^{Φ}. The other two potential fields Ξ and Ψ are defined in exactly the same way. This form of the expansion allows to choose different numbers and locations of the expansion centers for each scatterer and each field Ξ, Φ, and Ψ. Also, the maximal orders for the different multipoles can be chosen independently.

An expansion of the form (4) is known as multiple multipole (MMP) expansion because we have in fact a summation over, e.g., P_d^{Φ} multipoles located at $\mathbf{x}_{pd}^{\Phi}$. In the fluid, we choose the propagatory solutions $H_{|n|}^{(1)}(k_f r) e^{in\theta}$ to the Helmholtz equation (3a):

$$\xi_{pnd}(\mathbf{x}, \mathbf{x}_{pd}^{\Xi}, k_f) = H_{|n|}^{(1)}(k_f |\mathbf{x} - \mathbf{x}_{pd}^{\Xi}|) e^{in\theta_{pd}^{\Xi}} \qquad \text{with } \mathbf{x}_{pd}^{\Xi} \text{ inside scatterer } d, \tag{5a}$$

where θ_{pd}^{Ξ} is the angle $\angle(\hat{\mathbf{x}}, \mathbf{x} - \mathbf{x}_{pd}^{\Xi})$ with respect to the unit vector $\hat{\mathbf{x}}$ in the x-direction. Foreseeing the need of a free surface in the fluid phase, we directly add the stationary phase contribution of the field reflected at the surface (Chew, 1988; Imhof, 1995a) to the expansion

function (5a):

$$\xi_{pnd}(\mathbf{x}, \mathbf{x}_{pd}^\Xi, k_f) = H_{|n|}^{(1)}(k_f \, |\mathbf{x} - \mathbf{x}_{pd}^\Xi|) \, e^{in\theta_{pd}^\Xi} - H_{|n|}^{(1)}(k_f \, |\mathbf{x} - \boldsymbol{x}_{pd}^\Xi|) \, e^{-in\varphi_{pd}^\Xi}, \qquad (5b)$$

where $\varphi_{pd}^\Xi = \angle(\hat{\mathbf{x}}, \mathbf{x} - \boldsymbol{x}_{pd}^\Xi)$. The location $\boldsymbol{x}_{pd}^\Xi$ of the corresponding mirror source is obtained by reflection of the expansion center $\mathbf{x}_{pd}^\Xi$ across the free surface.

In the solid, we can choose between two different sets of expansion functions for ϕ_{pnd} and ψ_{pnd}. Either we use the propagatory solutions $H_{|n|}^{(1)}(k_s r) \, e^{in\theta}$ and $H_{|n|}^{(1)}(l_s r) \, e^{in\theta}$, or we choose the standing wave solutions $J_{|n|}(k_s r) \, e^{in\theta}$ and $J_{|n|}(l_s r) \, e^{in\theta}$:

$$\phi_{pnd}(\mathbf{x}, \mathbf{x}_{pd}^\Phi, k_s) = \begin{cases} J_{|n|}(k_s \, |\mathbf{x} - \mathbf{x}_{pd}^\Phi|) \, e^{in\theta_{pd}^\Phi} & \text{if } \mathbf{x}_{pd}^\Phi \text{ is inside scatterer } d \quad , \qquad (6a) \\[2mm] H_{|n|}^{(1)}(k_s \, |\mathbf{x} - \mathbf{x}_{pd}^\Phi|) \, e^{in\theta_{pd}^\Phi} & \text{if } \mathbf{x}_{pd}^\Phi \text{ is outside scatterer } d \quad . \qquad (6b) \end{cases}$$

Similarly, we have:

$$\psi_{pnd}(\mathbf{x}, \mathbf{x}_{pd}^\Psi, l_s) = \begin{cases} J_{|n|}(l_s \, |\mathbf{x} - \mathbf{x}_{pd}^\Psi|) \, e^{in\theta_{pd}^\Psi} & \text{if } \mathbf{x}_{pd}^\Psi \text{ is inside scatterer } d \quad , \qquad (7a) \\[2mm] H_{|n|}^{(1)}(l_s \, |\mathbf{x} - \mathbf{x}_{pd}^\Psi|) \, e^{in\theta_{pd}^\Psi} & \text{if } \mathbf{x}_{pd}^\Psi \text{ is outside scatterer } d \quad . \qquad (7b) \end{cases}$$

The three different wavefields are coupled by the boundary conditions along the interface of the fluid and the solid. The boundary conditions require continuity of the normal displacement $\hat{\mathbf{n}} \cdot \mathbf{u}$, continuity of normal traction $\hat{\mathbf{n}} \cdot \boldsymbol{\sigma} \cdot \hat{\mathbf{n}}$ and vanishing tangential traction $\hat{\mathbf{t}} \cdot \boldsymbol{\sigma} \cdot \hat{\mathbf{n}}$. For a point $\mathbf{x}$ on the interface with the unit normal $\hat{\mathbf{n}}$ and the unit tangential direction $\hat{\mathbf{t}}$, we have

$$\hat{\mathbf{n}} \cdot \left(\mathbf{u}^{inc}(\mathbf{x}, \omega) + \mathbf{u}^\Xi(\mathbf{x}, \omega) \right) = \hat{\mathbf{n}} \cdot \left(\mathbf{u}^\Phi(\mathbf{x}, \omega) + \mathbf{u}^\Psi(\mathbf{x}, \omega) \right) \qquad (8a)$$

$$\hat{\mathbf{n}} \cdot \left(\boldsymbol{\sigma}^{inc}(\mathbf{x}, \omega) + \boldsymbol{\sigma}^\Xi(\mathbf{x}, \omega) \right) \cdot \hat{\mathbf{n}} = \hat{\mathbf{n}} \cdot \left(\boldsymbol{\sigma}^\Phi(\mathbf{x}, \omega) + \boldsymbol{\sigma}^\Psi(\mathbf{x}, \omega) \right) \cdot \hat{\mathbf{n}} \qquad (8b)$$

$$0 = \hat{\mathbf{t}} \cdot \left(\boldsymbol{\sigma}^\Phi(\mathbf{x}, \omega) + \boldsymbol{\sigma}^\Psi(\mathbf{x}, \omega) \right) \cdot \hat{\mathbf{n}} \qquad (8c)$$

where the displacements are defined in (2). The stress tensor in the fluid is given by $\boldsymbol{\sigma}^\Xi(\mathbf{x}, \omega) = \mathbf{I} p(\mathbf{x}, \omega) = -\mathbf{I} k_f^2 \lambda_f \Xi(\mathbf{x}, \omega)$ which also defines the pressure $p(\mathbf{x}, \omega)$. The stress tensors $\boldsymbol{\sigma}^\Phi(\mathbf{x}, \omega)$ and $\boldsymbol{\sigma}^\Psi(\mathbf{x}, \omega)$ are defined in a local coordinate system (r, y, θ) centered at

the expansion center of the multipole.

$$\sigma_{rr}^{\Phi} = -\lambda_s k_s^2 \Phi + 2\mu \frac{\partial^2 \Phi}{\partial r^2} \qquad\qquad \sigma_{rr}^{\Psi} = 2\mu \frac{\partial}{\partial r}\left(\frac{1}{r}\frac{\partial \Psi}{\partial \theta}\right) \tag{9}$$

$$\sigma_{\theta\theta}^{\Phi} = -\lambda_s k_s^2 \Phi + 2\mu \frac{1}{r}\left(\frac{\partial \Phi}{\partial r} + \frac{1}{r}\frac{\partial^2 \Phi}{\partial \theta^2}\right) \qquad \sigma_{\theta\theta}^{\Psi} = 2\mu\left[\frac{1}{r}\left(\frac{1}{r}\frac{\partial \Psi}{\partial \theta} - \frac{\partial^2 \Psi}{\partial r \partial \theta}\right)\right] \tag{10}$$

$$\sigma_{r\theta}^{\Phi} = 2\mu\left[\frac{1}{r}\frac{\partial^2 \Phi}{\partial r \partial \theta} - \frac{1}{r^2}\frac{\partial \Phi}{\partial \theta}\right] \qquad \sigma_{r\theta}^{\Psi} = 2\mu\left[\frac{1}{2r^2}\frac{\partial^2 \Psi}{\partial \theta^2} - \frac{r}{2}\frac{\partial}{\partial r}\left(\frac{1}{r}\frac{\partial \Psi}{\partial r}\right)\right] \tag{11}$$

Note that the components of displacements and of the stress tensors have to be transformed or rotated into the global coordinate frame (x, y, z) in which the unit normal $\hat{\mathbf{n}}$ and the unit tangential direction $\hat{\mathbf{t}}$ are defined.

We solve for the unknown coefficients a_{pnd}, b_{pnd} and c_{pnd} by enforcing the boundary conditions (8) on discrete matching points $\mathbf{x}_m$ along the boundaries of the scatterers. We obtain a linear system of equations

$$
\begin{pmatrix}
-\Xi_{11}^n & -\Xi_{12}^n & -\Xi_{13}^n & \Phi_{11}^n & \Psi_{11}^n & 0 & 0 & 0 & 0 \\
-\Xi_{11}^{nn} & -\Xi_{12}^{nn} & -\Xi_{13}^{nn} & \Phi_{11}^{nn} & \Psi_{11}^{nn} & 0 & 0 & 0 & 0 \\
0 & 0 & 0 & \Phi_{11}^{nt} & \Psi_{11}^{nt} & 0 & 0 & 0 & 0 \\
-\Xi_{21}^n & -\Xi_{22}^n & -\Xi_{23}^n & 0 & 0 & \Phi_{22}^n & \Psi_{22}^n & 0 & 0 \\
-\Xi_{21}^{nn} & -\Xi_{22}^{nn} & -\Xi_{23}^{nn} & 0 & 0 & \Phi_{22}^{nn} & \Psi_{22}^{nn} & 0 & 0 \\
0 & 0 & 0 & 0 & 0 & \Phi_{2}^{nt} & \Psi_{2}^{nt} & 0 & 0 \\
-\Xi_{31}^n & -\Xi_{32}^n & -\Xi_{33}^n & 0 & 0 & 0 & 0 & \Phi_{33}^n & \Psi_{33}^n \\
-\Xi_{31}^{nn} & -\Xi_{32}^{nn} & -\Xi_{33}^{nn} & 0 & 0 & 0 & 0 & \Phi_{33}^{nn} & \Psi_{33}^{nn} \\
0 & 0 & 0 & 0 & 0 & 0 & 0 & \Phi_{33}^{nt} & \Psi_{33}^{nt}
\end{pmatrix}
\cdot
\begin{pmatrix}
\mathbf{a}_1 \\ \mathbf{a}_2 \\ \mathbf{a}_3 \\ \mathbf{b}_1 \\ \mathbf{c}_1 \\ \mathbf{b}_2 \\ \mathbf{c}_2 \\ \mathbf{b}_3 \\ \mathbf{c}_3
\end{pmatrix}
\approx
\begin{pmatrix}
\mathbf{u}_1^n \\ \sigma_1^{nn} \\ 0 \\ \mathbf{u}_2^n \\ \sigma_2^{nn} \\ 0 \\ \mathbf{u}_3^n \\ \sigma_3^{nn} \\ 0
\end{pmatrix}
\tag{12}
$$

where we used the submatrices Ξ_{sd}^n, Φ_{sd}^n, and Ψ_{sd}^n to denote the normal displacements $\hat{\mathbf{n}} \cdot \mathbf{u}$ at the matching points along the scatterer $s \in \{1, 2, 3\}$ due to ξ_{pnd}, ϕ_{pnd}, and ψ_{pnd}. The submatrices Ξ_{sd}^{nn}, Φ_{sd}^{nn}, and Ψ_{sd}^{nn} are the same but for the normal stress $\hat{\mathbf{n}} \cdot \boldsymbol{\sigma} \cdot \hat{\mathbf{n}}$. The submatrices Φ_{sd}^{nt} and Ψ_{sd}^{nt} contain the tangential stresses $\hat{\mathbf{t}} \cdot \boldsymbol{\sigma} \cdot \hat{\mathbf{n}}$. For the sake of clarity,

the index d is used to indicate which scatterer induces the field. The index s indicates along which scatterer the boundary conditions are evaluated and thus on which boundary the matching points $\mathbf{x}_m$ lie. All three scatterers contribute to the scattered field $\Xi(\mathbf{x}_m, \omega)$ in the fluid. Therefore, we have submatrices Ξ_{sd} for each scatterer d and each boundary s. But because, e.g., scatterer 1 has no common boundary with scatterer 2, the fields $\Phi_1(\mathbf{x}_m, \omega)$, $\Psi_1(\mathbf{x}_m, \omega)$ and $\Phi_2(\mathbf{x}_m, \omega)$, $\Psi_2(\mathbf{x}_m, \omega)$ do not interact with each other. Thus for $s \neq d$, the submatrices Φ_{sd} and Ψ_{sd} vanish. The individual scatterers are only coupled by the scattered fields $\Xi_1(\mathbf{x}_m, \omega)$, $\Xi_2(\mathbf{x}_m, \omega)$, and $\Xi_3(\mathbf{x}_m, \omega)$ propagating in the fluid. All multiple scattering is automatically accounted for by the boundary conditions. The only contribution for the fields within, e.g., scatterer 1 are due to the (self) interactions of $\Phi_1(\mathbf{x}_m, \omega)$ and $\Psi_1(\mathbf{x}_m, \omega)$.

Defining the matching points by their location $\mathbf{x}_{ms}$ along the boundary of scatterer s, we can write the submatrices as

$$
\begin{aligned}
\Xi_{sd}^n &= \left[u_n\left(\xi_{pnd}(\mathbf{x}_{ms}, \omega) \right) \right], \quad & \Phi_{sd}^n &= \left[u_n\left(\phi_{pnd}(\mathbf{x}_{ms}, \omega) \right) \right], \quad & \Psi_{sd}^n &= \left[u_n\left(\psi_{pnd}(\mathbf{x}_{ms}, \omega) \right) \right], \\
\Xi_{sd}^{nn} &= \left[\sigma_{nn}\left(\xi_{pnd}(\mathbf{x}_{ms}, \omega) \right) \right], \quad & \Phi_{sd}^{nn} &= \left[\sigma_{nn}\left(\phi_{pnd}(\mathbf{x}_{ms}, \omega) \right) \right], \quad & \Psi_{sd}^{nn} &= \left[\sigma_{nn}\left(\psi_{pnd}(\mathbf{x}_{ms}, \omega) \right) \right], \\
& & \Phi_{sd}^{nt} &= \left[\sigma_{nt}\left(\phi_{pnd}(\mathbf{x}_{ms}, \omega) \right) \right], \quad & \Psi_{sd}^{nt} &= \left[\sigma_{nt}\left(\psi_{pnd}(\mathbf{x}_{ms}, \omega) \right) \right].
\end{aligned}
\tag{13}
$$

Similarly, the vectors $\mathbf{u}_s^n$ and $\boldsymbol{\sigma}_s^{nn}$ on the right hand side represent the incident wavefield in the fluid evaluated at the matching points $\mathbf{x}_{ms}$:

$$
\mathbf{u}_s^n = \left[u_n^{inc}(\mathbf{x}_{ms}, \omega) \right], \qquad\qquad \boldsymbol{\sigma}_s^{nn} = \left[\sigma_{nn}^{inc}(\mathbf{x}_{ms}, \omega) \right].
\tag{14}
$$

Finally, the vectors $\mathbf{a}_d$, $\mathbf{b}_d$ and $\mathbf{c}_d$ contain the unknown coefficients a_{pnd}, b_{pnd} and c_{pnd}. Because the MMP expansions (4) are commonly non-orthogonal, the system (12) is made overdetermined by choosing more matching points than needed. It is then solved in the least-squares sense by QR decomposition (Strang, 1988) using Givens updating (Schwarz, 1989).

10

Numerical Modelling

To interpret the ultrasonic results, we model the scattering problems depicted in Figures 1 and 2. Three rods of lucite are submerged in water. The rods have a P-wave velocity $\alpha = 2570\,\text{m/s}$, a S-wave velocity $\beta = 1200\,\text{m/s}$, and a density ρ_s of $1180\,\text{kg/m}^3$. In the water, the P-wave velocity γ and the density ρ_f are $1460\,\text{m/s}$, respectively $1000\,\text{kg/m}^3$. A vertical point force excites an acoustic wave which propagates downwards and interacts with the elastic scatterers. The source pulse is modulated by a Ricker wavelet (Ricker, 1977) of 200 kHz. The resulting scattered fields are measured at 75 locations along the surface. Source, scatterers and receivers are separated by at least 30 dominant wavelengths of 6 mm. Due to the resulting long propagation times, many frequencies are needed to calculate the traces. For a sampling interval of 400 ns, we will use 512 frequencies.

To damp resonances, we account for the intrinsic attenuation in the scatterers by making the wave number k complex

$$k = k_r + ia \tag{15}$$

where a is the attenuation coefficient. Alternatively, we use the quality factor Q which relates to the attenuation coefficient a by

$$Q = \frac{\omega}{2ac} \tag{16}$$

where the velocity c is either α or β. Both quality factors Q_p and Q_s are assumed to be 100.

The scattered wavefield in the fluid is expanded as (4a) where we choose $D = 3$, $P_1^\Xi = 4$, $P_2^\Xi = 5$, and $P_3^\Xi = 3$. For each of these multipoles, we choose $N_{pd}^\Xi = 6$. As expansion function, we use (5b) which includes the reflections from the free surface. Figure 7 defines the exact locations of the expansion centers for the syncline model (Figure 1). For the anticline model, the same locations relative to the solids are used for the expansion centers.

The wavefields in the solid scatterers are expanded as (4b) and (4c) for the P-, respectively the S-wave. For scatterer Γ^1, we choose $P_1^\Phi = P_1^\Psi = 12$. For scatterer Γ^2, we use $P_2^\Phi =$

11

$P_2^\Psi = 14$. Finally, for the third scatterer Γ^3 we employ $P_3^\Phi = P_3^\Psi = 10$ expansion centers. At each expansion center, we use only the orders between -3 and 3. Thus, $N_{pd}^\Phi = N_{pd}^\Psi = 3$. Because we placed the expansion centers for the wavefields in the solids *outside* the scatterers (Figure 7), we have to use (6b) and (7b) to describe the P-, respectively the S-waves. For resonating geometries such as the posed problem, the propagatory solutions (6b) and (7b) are superior to the standing wave solutions (6a) and (7a). First, their amplitudes decay faster (Hafner, 1990). But they also force us to illuminate the scatterers from all sides which decouples the multipoles and the interfaces because each multipole illuminates mainly the interface closest to its expansion center. This effect lowers the condition number and thus enhances the stability of the numerical matrix inversion. For both models, 660 expansion functions and 444 matching points (= 1332 equations) are used.

Figures 8 and 13 show the synthetic seismograms as calculated by the MMP expansions for the syncline-, respectively the anticline model. The first $120\,\mu$s are suppressed since they only contain the direct arrival.

Comparison of the Tank Data with the MMP Solutions

The advantage of the MMP solution over the ultrasonic watertank data is that, by construction, the wavefields are decomposed by scatterer. Once the equation system (12) is solved for a particular model, we fix the summation index d to 1, 2, or 3 in expression (4a) when evaluating the seismograms. Remember that the index d denotes the scatterer which emits a particular field. Thus, we can plot the scattered wavefields for each of the three scatterers independently which simplifies the seismograms and allows correlation of events with scatterers.

In the ultrasonic experiment, we use a point source and a point receiver. The models contain no variation perpendicular to the source-receiver plane. Hence, the experiments are in fact $2\frac{1}{2}$-D experiments. However, the numerical MMP scheme is derived and applied to

2-D only. Comparing the experimental results to the numerical ones might be problematic. But Esmersoy (1986) and Lo (1987) showed that the differences between 2-D and $2\frac{1}{2}$-D are negligible as long as the scatterers are in the far field with respect to both the source and the receivers. At the center frequency of 190 kHz, the scatterers are at least 15 wavelengths away from either source or receivers for both geometries. Clearly, the far field condition is satisfied.

Syncline Model

A comparison between the ultrasonic record (Figure 5) and the MMP solution (Figure 8) shows that the arrival times and amplitudes for different events match very well. The main difference between the Figures 5 and 8, the real and the synthetic data, are the strong, repetitive events in the central part of the real seismogram. The cause is the signature of the source tranducer (Figure 4) which rings more than a Ricker wavelet.

The butterfly pattern typical for synclines can easily be seen (Haartsen *et al.*, 1994). As expected, each scatterer reflects twice with opposing polarity corresponding to reflections from the top and from the bottom. The two events are typically 14 μs separated. Toward the end of the traces at 300 μs, reverberations of the reflection from scatterer Γ^2 can be found which bounced between the surface and the scatters Γ^1 and Γ^3. These effects can be seen more clearly in the MMP solution decomposed by scatterer shown in Figures 9 to 11. All synthetic seismograms are scaled similarly which allows to compare the amplitudes between the different figures.

The decomposed MMP solution in Figures 9 to 11 shows that the event around 180 μs in the tank data (Figure 5) is in reality composed of different events. First, there is the direct reflection from scatterer Γ^2. But this reflection was also diffracted through the scatterers Γ^1 and Γ^3 as the seismograms 9 and 11 show. Also, the first multiple reflections from inside Γ^1 and Γ^3 appear nearly at that time. Another interesting set of event appears at 256 μs

and $270\,\mu s$. Figure 9 correlates these two events with scatterer Γ^1. The traveltimes prove them to be reflections from Γ^1 bouncing between the water surface and Γ^1. The prior one reflected twice from the top of Γ^1. The latter one reflected once from the top, once from the bottom. Thus, one would expect another event about $14\,\mu s$ later corresponding a wave bouncing between the bottom of Γ^1 and the water surface. Indeed, a very weak event appears at the expected time in the tank data (Figure 5) and the MMP solutions (Figures 8 and 9). A final subtlety are the multiples arriving around $300\,\mu s$ which justify the stationary phase reflections into the MMP expansion functions (5b). The scattered fields in Figures 9 to 11 show very nicely that these events are a combination of different waves. First, there are waves reflected from Γ^2, then bounced of the water surface and finally rebounded from either Γ^1 or Γ^3. But we also encounter the opposite: waves reflecting from Γ^1 or Γ^3, bouncing of the water surface and finally rebounding from Γ^2. To demonstrate the effect of the multiple scattering, we calculate the acousto-elastic response for each scatterer separately and subtract them from the complete MMP solution (Figure 8). The residual wavefield is shown in Figure 12. The amplitudes in both figures are scaled by the same amount to ease a direct comparison of single scattering versus multiple scattering. Clearly, the two scatterers Γ^1 and Γ^3 speed up the reflection from Γ^2. The remaining events are waves bouncing between the three scatterers and the water surface as well as internal multiples sped up passing through Γ^1 and Γ^3.

Anticline Model

Both the ultrasonic record (Figure 6) and the MMP solution (Figure 13) clearly show the reflections from the top and the bottom of each scatterer. Not surprisingly, scatterer Γ^2 shadows Γ^1 as the rather abrupt change in the reflection-amplitude around $170\,\mu s$ demonstrates. To identify a few other events, we decompose the MMP solution by scatterer. The decomposed seismograms are shown in Figures 14 to 16.

For example, Figure 15 shows that part of the ringing main reflection around $130\,\mu s$ is

caused by multiple scattering inside Γ^2. The bottom reflection even splits into 2 events forming a butterfly pattern which repeats every $14\,\mu s$. At $170\,\mu s$, the main reflection from scatterer Γ^1 appears in the scattered field of Γ^2. This event can be interpreted as reflection from Γ^1 but propagating through Γ^2. Similarly at $190\,\mu s$, Figure 15 shows the reflection of Γ^3 being diffracted through Γ^2. After both events, internal multiples from Γ^1 and Γ^3 show up in the fields scattered from Γ^1 and Γ^3, respectively. Diffractions of these multiples passing through Γ^2 are again present in Figure 15.

To demonstrate the effect of the multiple scattering, we calculate the response of each scatterer alone and subtract it from the complete MMP solution (Figure 13). The residual wavefield is shown in Figure 17. The amplitudes in both figures are scaled by the same amount to allow a direct comparison of single scattering versus multiple scattering. For the first $170\,\mu s$, the events emanated by scatterer Γ^2 are the same for single or multiple scattering. Clearly, the reflection from scatterer Γ^1 separates into two events in the residual seismogram shown in Figure 17. Scatterer Γ^2 not only shadows Γ^1 but also speeds up the arrival time of the reflection passing through the fast solid. The same holds for some of the later events in Figure 17 corresponding to internal multiples. The remaining events are generated by waves bouncing between the three scatterers and the water surface. For example, the reflections around $300\,\mu s$ are caused by multiple scattering between Γ^2, the water surface, and either of Γ^1 or Γ^3.

Summary

Already for simple geometries, the wavefield scattered from solids submerged in water can be rather complex. Furthermore, the scattered wavefield becomes even more complicated if the water surface interacts with the scatters. Especially the syncline experiment, where three lucite rods were submerged in an ultrasonic watertank, demonstrates this point. Although the main reflections are simple to identify, the remaining events are very hard to interpret.

To aid the interpretation, we forward-modelled the situations numerically using the multiple multipole method (MMP). For each submerged solid, the scattered wavefield induced in the fluid is expanded into a MMP expansion (Imhof, 1995a). Similarly, in each solid two MMP expansions are used to describe the P- and S-components of the elastic wavefields. The advantage of the MMP scheme is that the scattered wavefields are, by construction, decomposed by scatterer as well as by mode of propagation. Hence, the wavefields scattered from each solid can be plotted independently which facilitates the correlation of particular events with individual scatterers. Curiously, this allows to distinguish direct reflections from reflections diffracted by another scatterer along their path of propagation.

In conclusion, we found that acousto-elastic multiple multipole expansions are a versatile tool either to directly solve scattering problems or to aid in their interpretation. This work should find uses in a variety of fields, notable in geophysics and oil exploration, as well as in naval underwater applications.

Acknowledgments

References

Boström, A. (1980). Scattering of stationary acoustic waves by an elastic obstacle immersed in a fluid. *J. Acoust. Soc. Am.*, **67**(2), 390–398.

Chew, W. C. (1988). A quick way to approximate a Sommerfeld-Weyl-type integral. *IEEE Transactions on Antennas and Propagation*, **36**(11), 1654–1657.

de Hoop, A. T. (1990). Reciprocity theorems for acoustic wave fields in fluid/solid configurations. *J. Acoust. Soc. Am.*, **87**(5), 1932–1937.

Esmersoy, C. (1986). *The Backpropagated Field Approach to Multidimensional Velocity Inversion*. Ph.D. thesis, Massachusetts Institute of Technology, Cambridge, MA.

Everstine, G. C. and Au-Yang, M. K., editors (1984). *Advances in Fluid-Structure Interaction*. American Society of Mechanical Engineers, New York.

Everstine, G. C. and Henderson, F. M. (1990). Coupled finite element / boundary element approach for fluid-structure interaction. *J. Acoust. Soc. Am.*, **87**, 1938–1947.

Fyfe, K. R., Coyette, J. P., and van Vooren, P. A. (1991). Acoustic and elasto-acoustic analysis using finite element and boundary element methods. *Sound and Vibration*, **25**(12), 16–22.

Haartsen, M. W., Bouchon, M., and Toksöz, M. N. (1994). A study of seismic acoustic wave propagation through a laterally varying medium using the boundary-integral-equation-discrete wave-number method. *J. Acoust. Soc. Am.*, **96**, 3010–3021.

Hafner, C. (1990). *The Generalized Multipole Technique for Computational Electromagnetics*. Artech House, Boston.

Imhof, M. G. (1995a). Multiple multipole expansions for acoustic scattering. *J. Acoust. Soc. Am.*, **97**(2), 754–763.

Imhof, M. G. (1995b). Multiple multipole expansions for elastic scattering. *J. Acoust. Soc. Am.* submitted.

Jensen, F. B., Kuperman, W. A., Porter, M. B., and Schmidt, H. (1994). *Computational Ocean Acoustics*. American Institute of Physics, New York.

Junger, M. C. and Feit, D. (1986). *Sound, Structures, and their Interaction*. MIT Press, Cambridge, MA, 2nd edition.

Lo, T. W. (1987). *Seismic Borehole Tomography*. Ph.D. thesis, Massachusetts Institute of Technology, Cambridge, MA.

Luke, C. J. and Martin, P. A. (1995). Fluid-solid interaction: acoustic scattering by a smooth elastic obstacle. *SIAM Journal on Applied Mathematics*, **55**(4), 904.

Mathews, I. C. (1986). Numerical techniques for three-dimensional steady-state fluid-structure interaction. *J. Acoust. Soc. Am.*, **79**(5), 1317–1325.

Norris, A. N. (1990). Resonant acoustic scattering from solid targets. *J. Acoust. Soc. Am.*, **88**(1), 505–514.

Pao, Y. H. and Mow, C. C. (1973). *Diffraction of Elastic Waves and Dynamic Stress Concentrations*. Crane Russak, New York.

Ricker, N. H., editor (1977). *Transient Waves in Visco-Elastic Media*. Elsevier Scientific Publishers, Amsterdam.

Schwarz, H. R. (1989). *Numerical Analysis*. Wiley, New York.

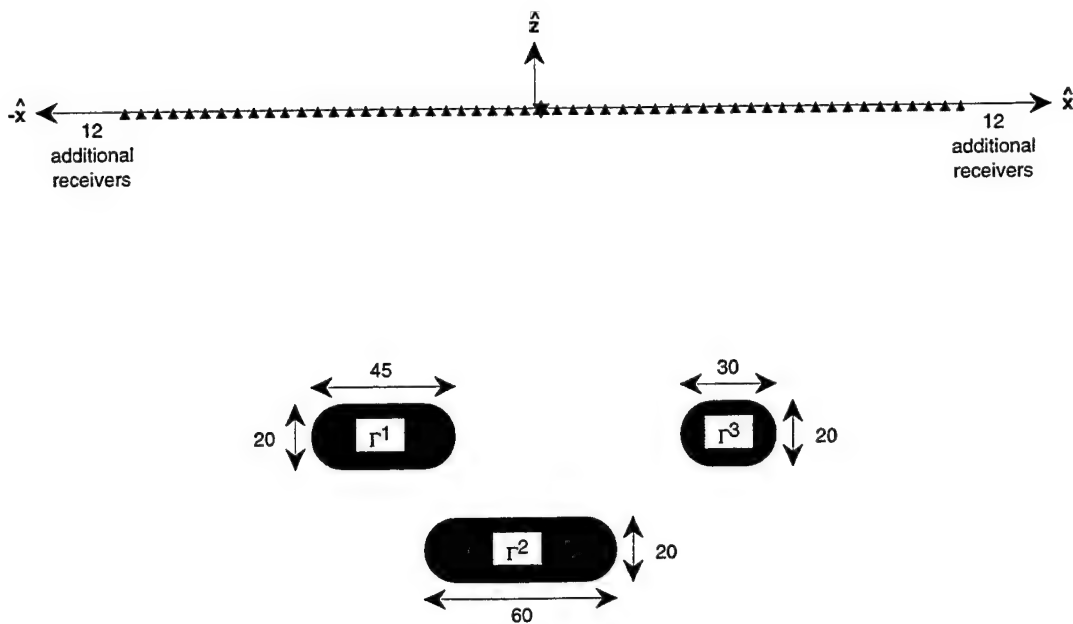Strang, G. (1988). *Linear Algebra and its Applications*. Harcourt, San Diego, CA, 3rd edition.

Figure 1: 'Syncline' model: Three oval rods of lucite are submerged in water. The source-transducer (star) generates a pressure wave which scatters between the rods and the water surface until it is picked up by the 75 receivers (triangles). All dimensions are in millimeters. The respective centers of the scatterers Γ^1, Γ^2, and Γ^3 are located at $(-42.5, -99)$, $(0, -136)$ and $(65, -98)$. Both the source and receiver 38 are positioned at $(8, 0)$. The spacing between the receivers is $5\,\text{mm}$.
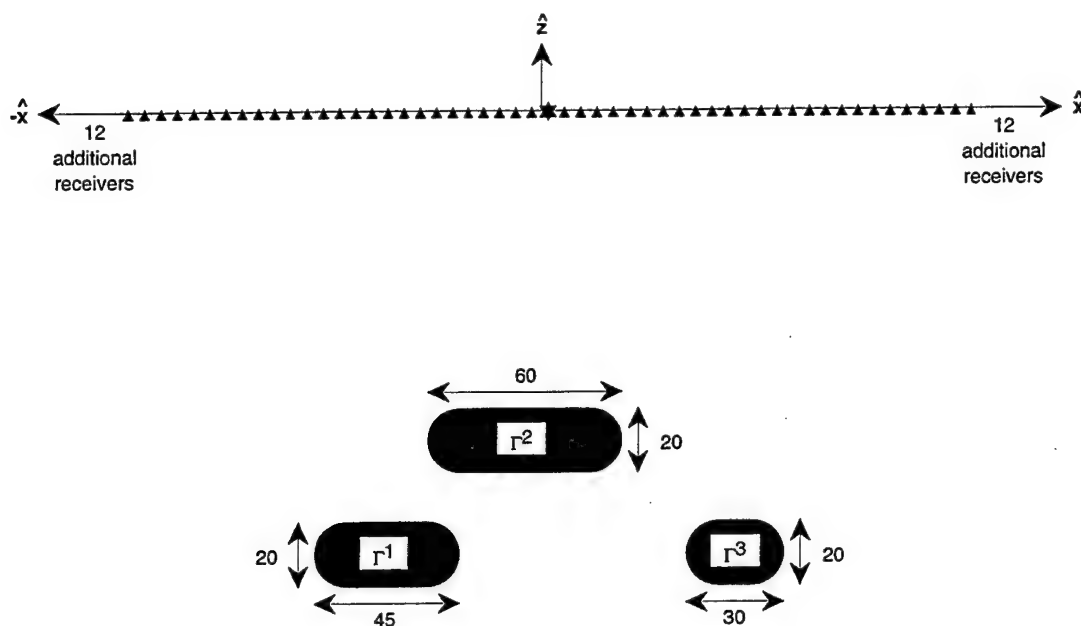
Figure 2: 'Anticline' model where the star denotes the source and the triangles symbolize the receivers. All dimensions are in millimeters. The respective centers of the oval scatterers Γ^1, Γ^2, and Γ^3 are located at $(-42.5, -135)$, $(0, -99)$ and $(65, -138)$. Both the source and receiver 38 are positioned at $(8, 0)$. The spacing between the receivers is $5\,\mathrm{mm}$.
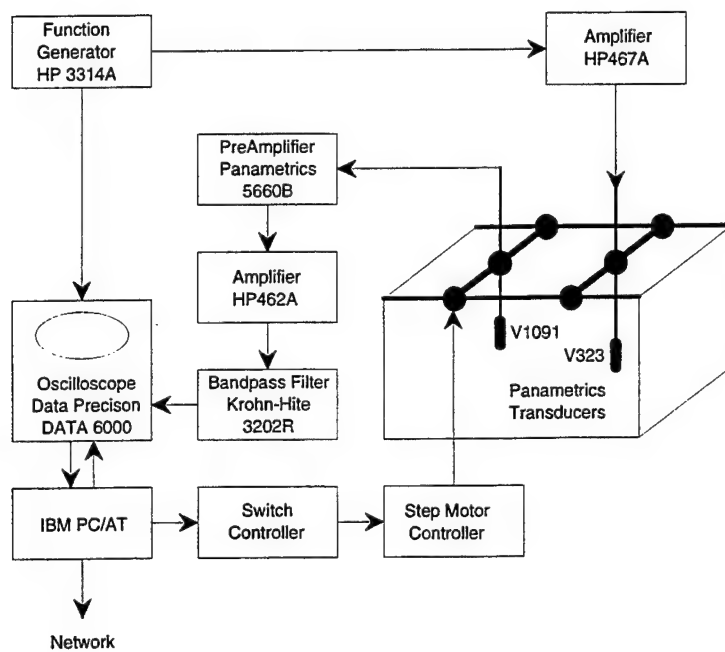
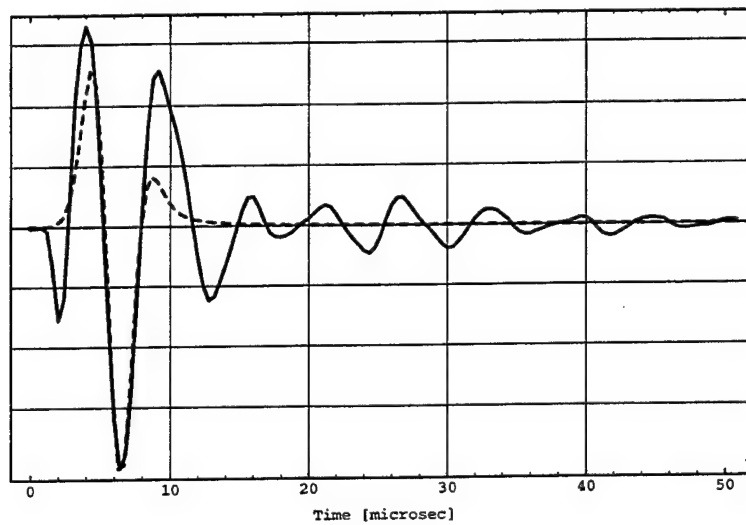Figure 3: Block diagram of the computer-based ultrasonic data-acquisition system.

Figure 4: Wavelets after propagating 30 wavelengths: measured in ultrasonic watertank (solid), Ricker wavelet used for numerical models (dashed).
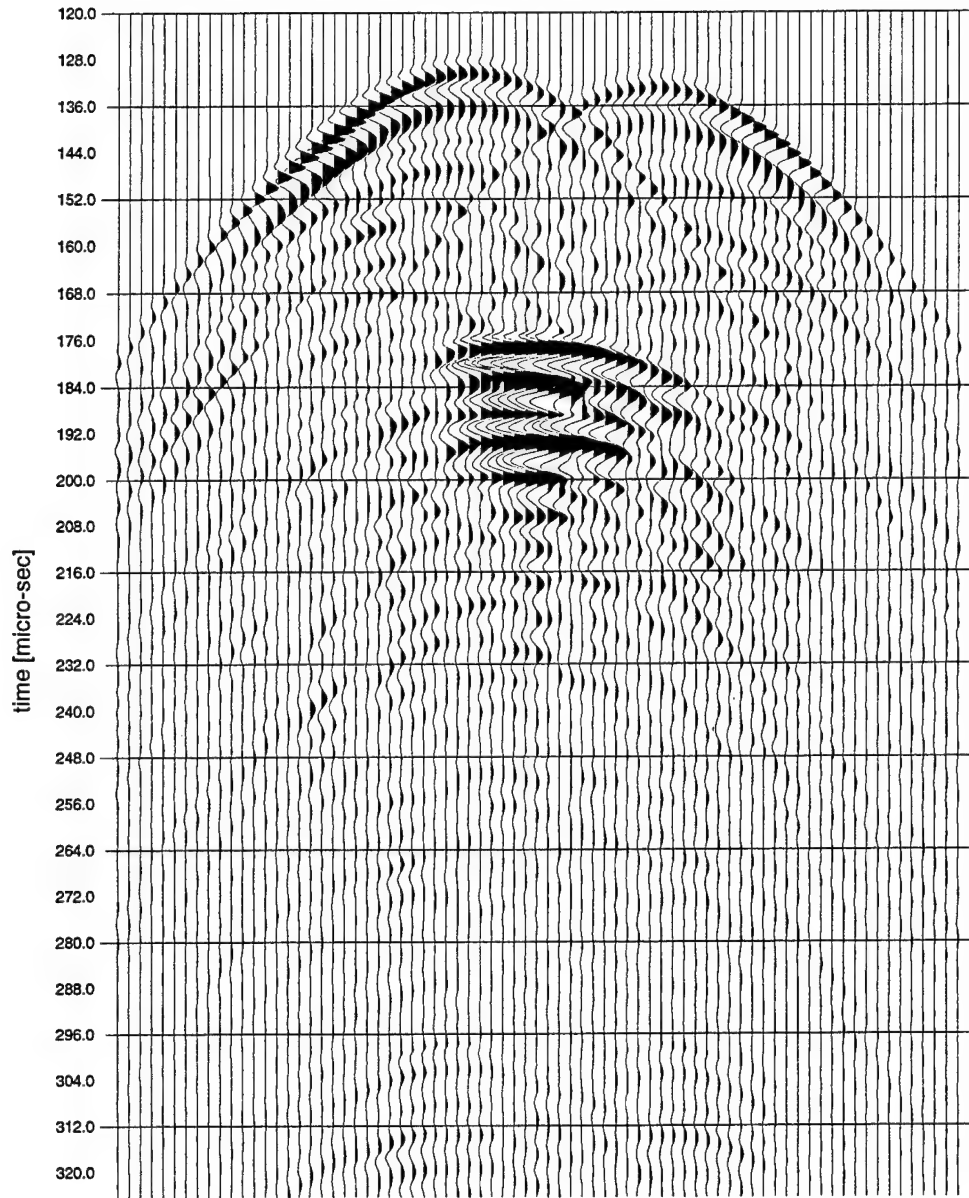
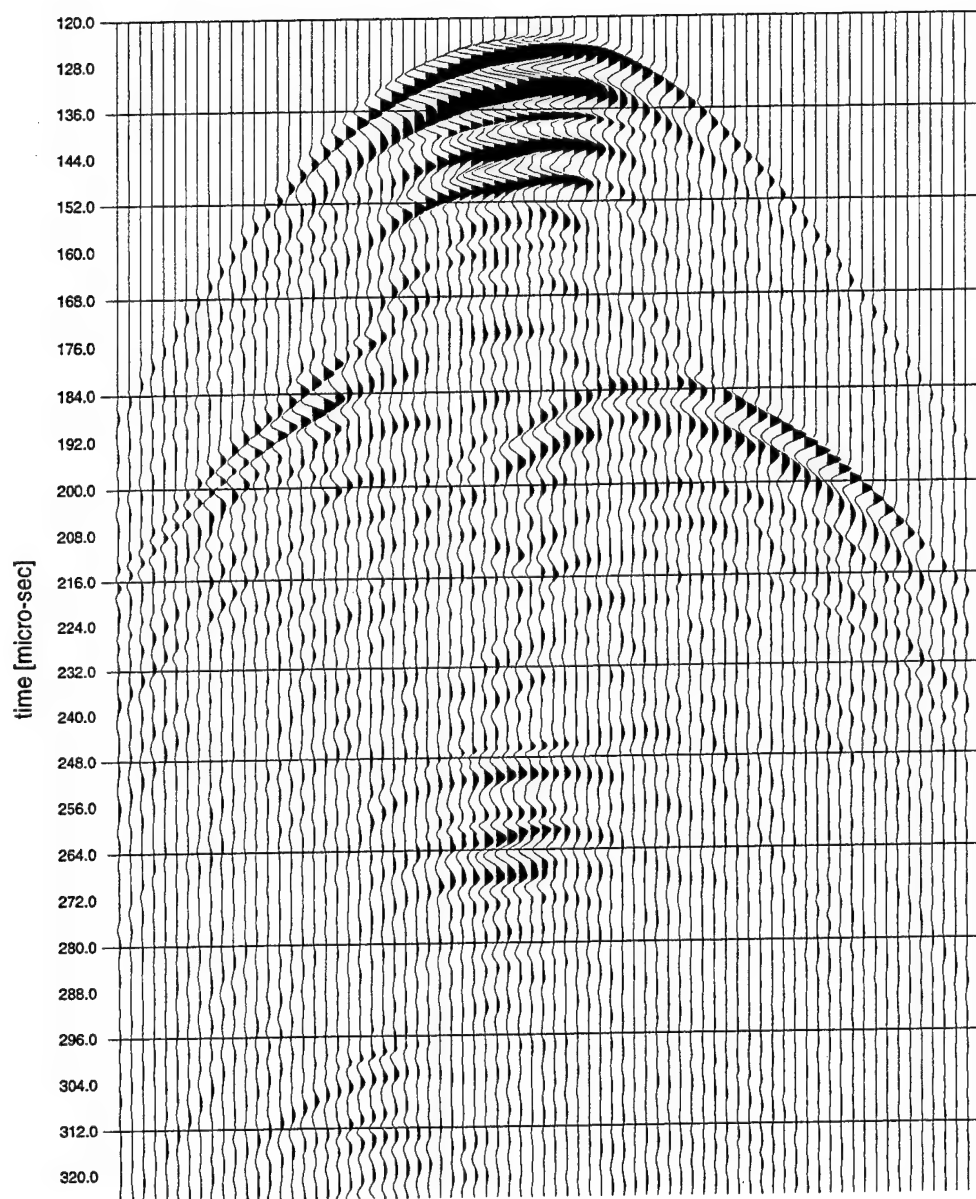Figure 5: The seismogram for the syncline model defined in Figure 1 as measured in the ultrasonic watertank.

Figure 6: The seismogram for the anticline model defined in Figure 2 as measured in the ultrasonic watertank.
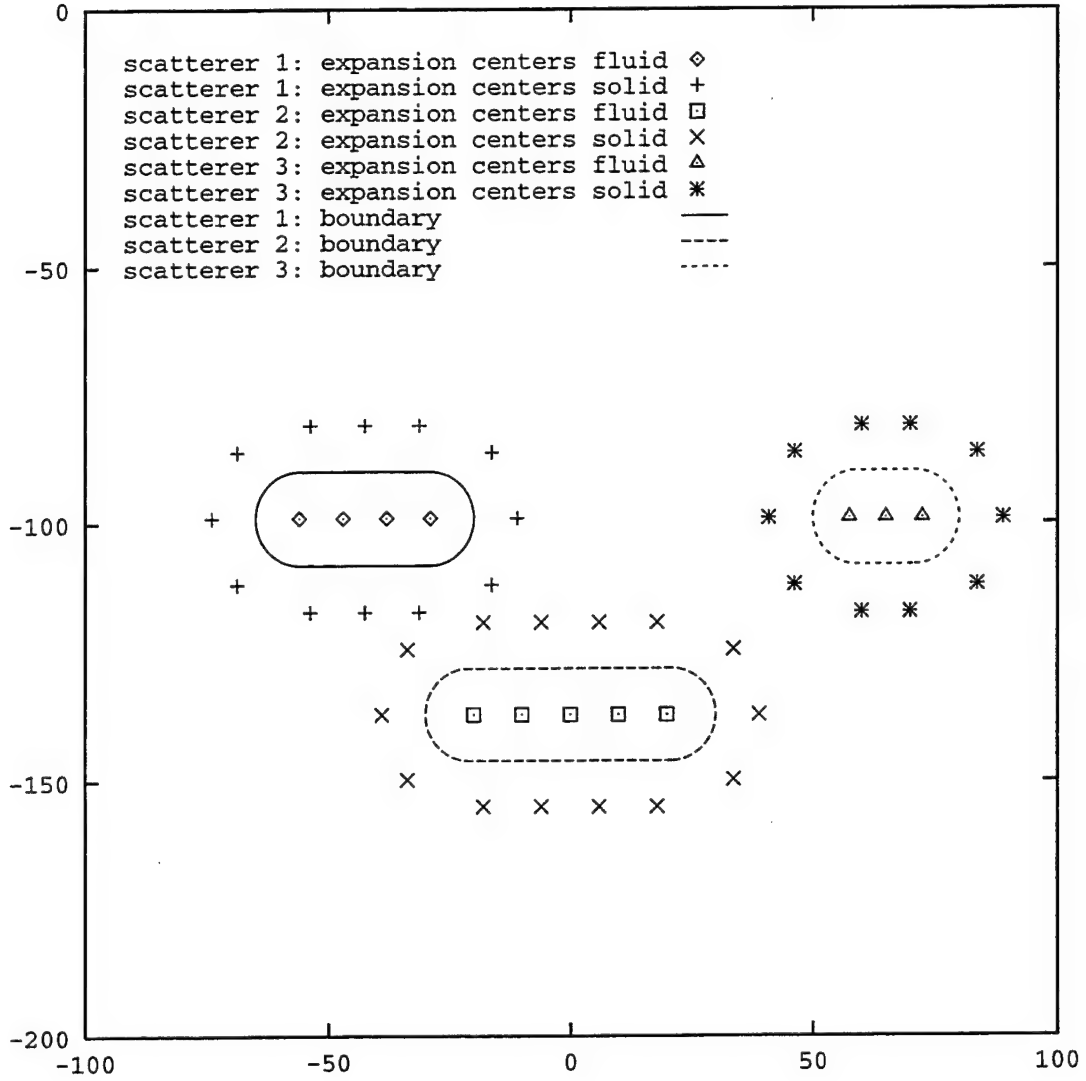
Figure 7: MMP discretization for the syncline model. Shown are the locations of the expansion centers for the multipoles. The multipoles inside the scatterers govern the wavefield in the fluid background. Multipoles are placed all around the scatterers to model the P- and S-waves on the inside. The discretization for the anticline model is the same but upside-down.
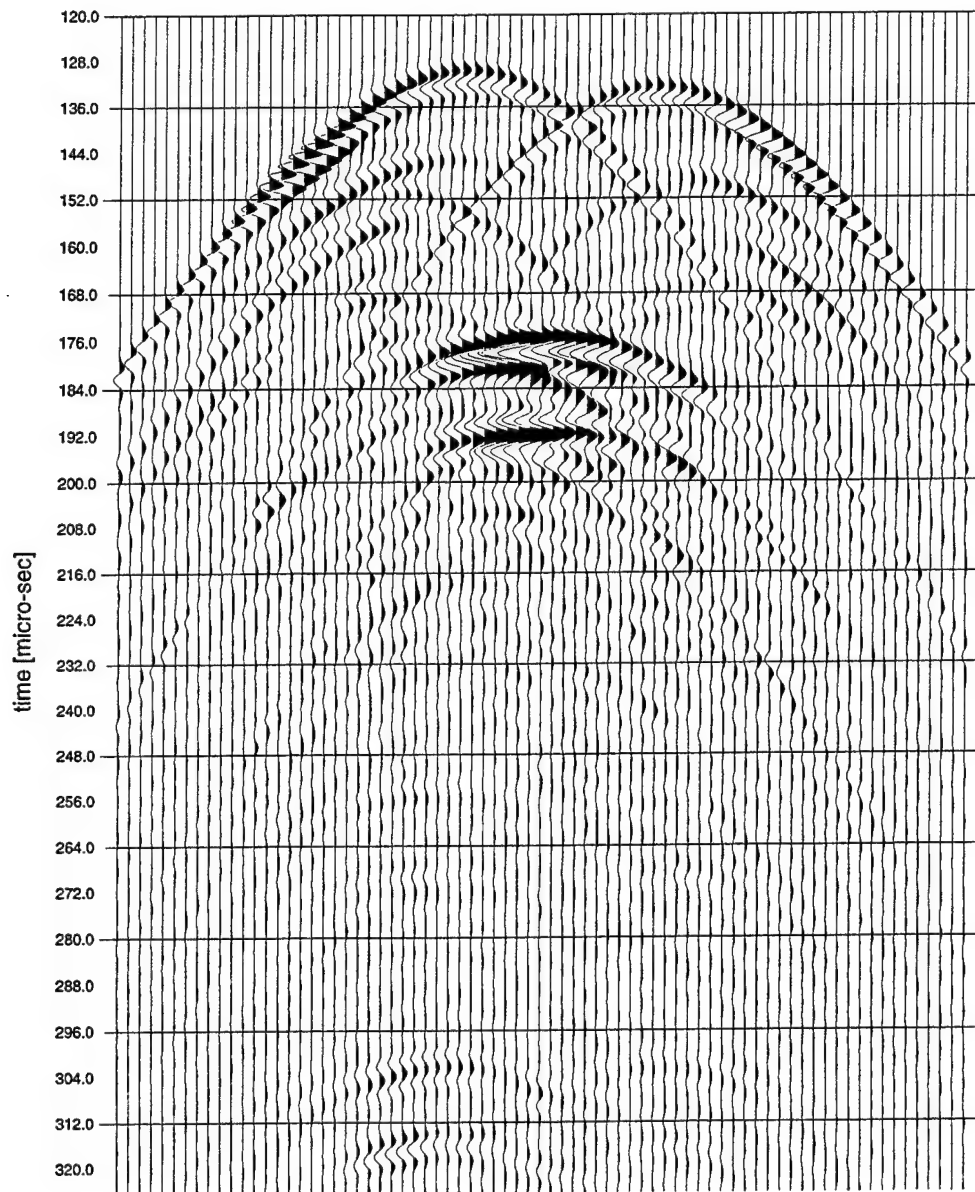
Figure 8: The seismogram for the syncline model (Figure 1) calculated by the MMP method.
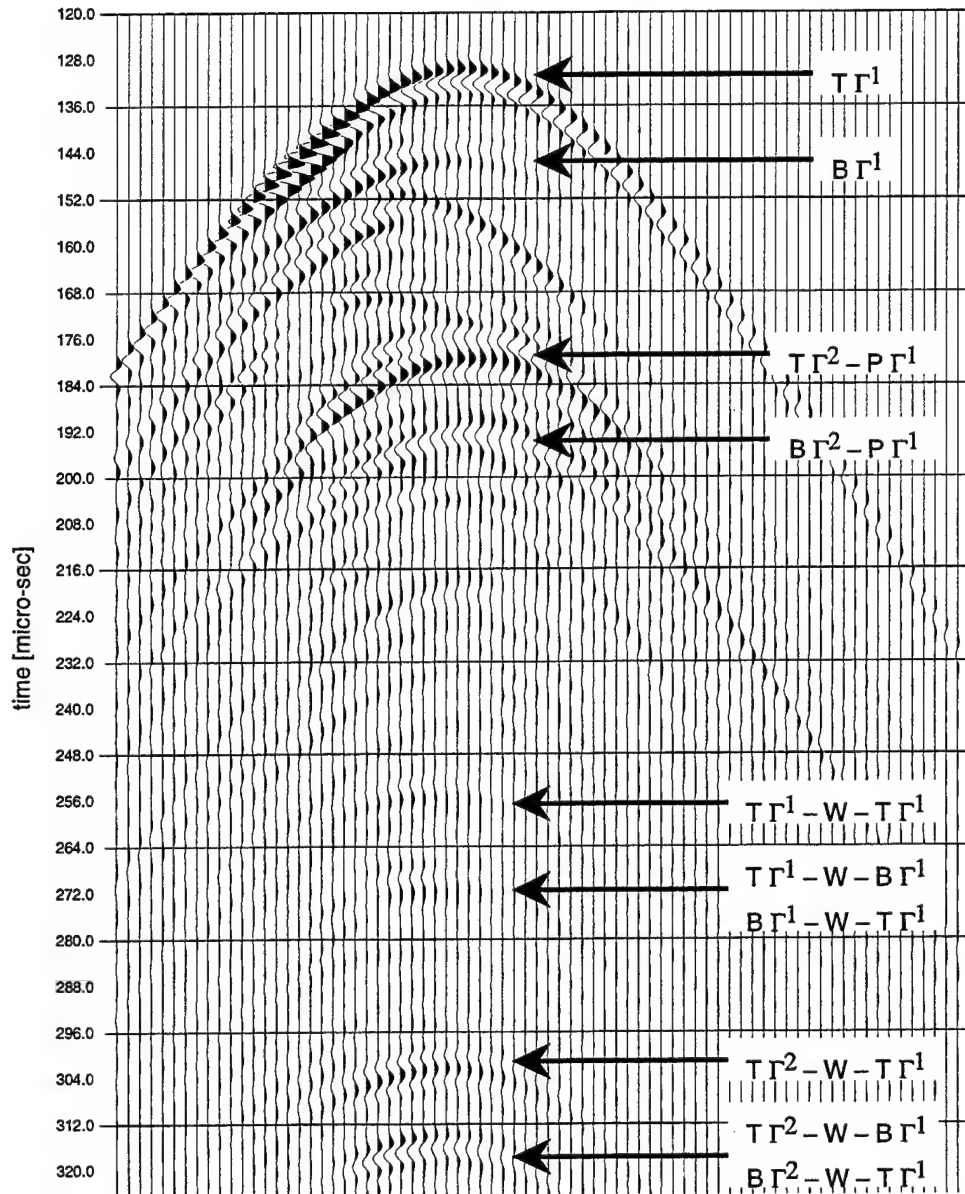
Figure 9: Syncline model: The scattered field emanated by Γ^1. The events around $180\,\mu s$ are reflections originating at scatterer Γ^2 but passing through scatterer Γ^1. The events at $300\,\mu s$ are reflections from Γ^2 bouncing between the surface and Γ^1. The symbol 'T' denotes a reflection from the top of the following scatterer, 'B' reflection from the bottom, 'W' reflection from the water surface, and 'P' means passes through the scatterer.
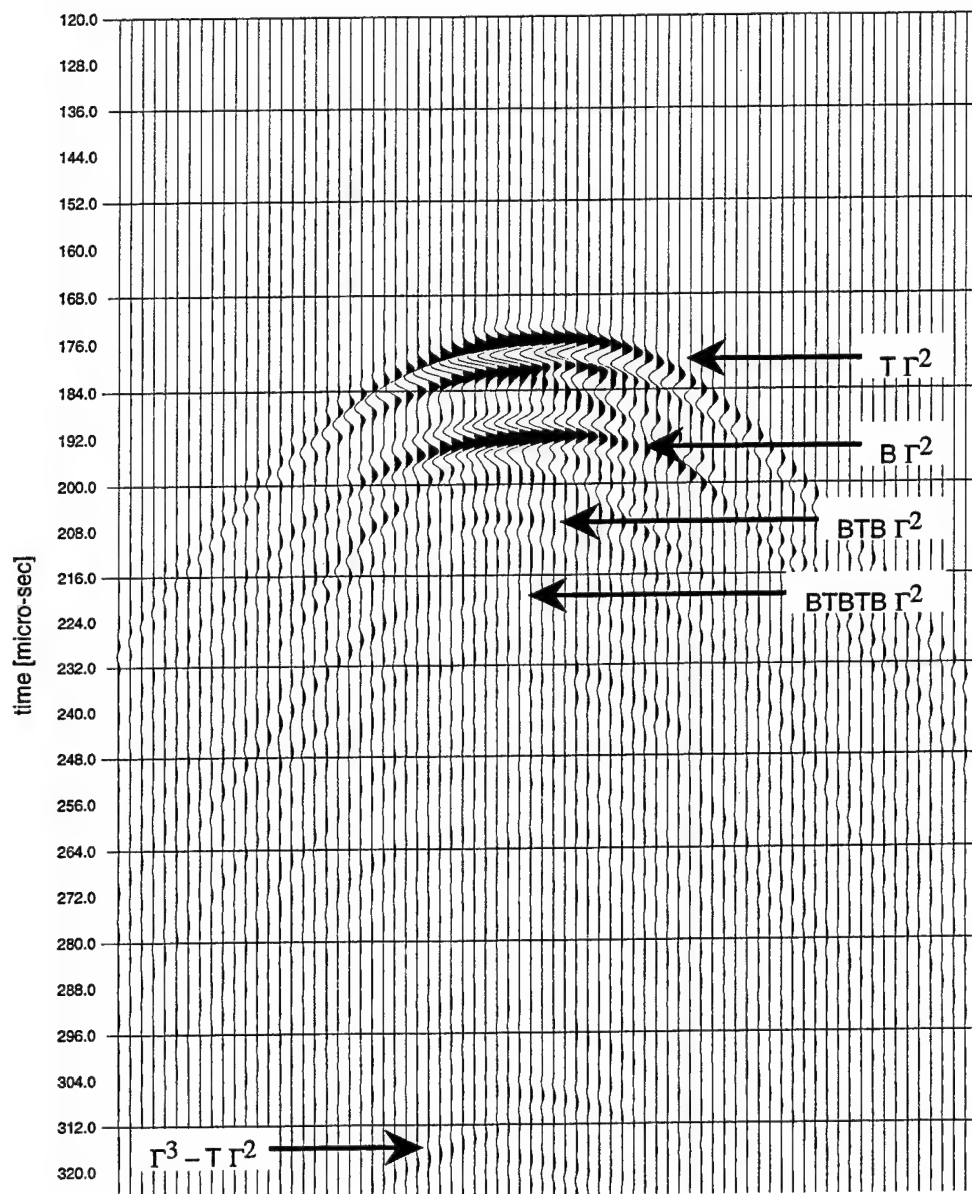
27

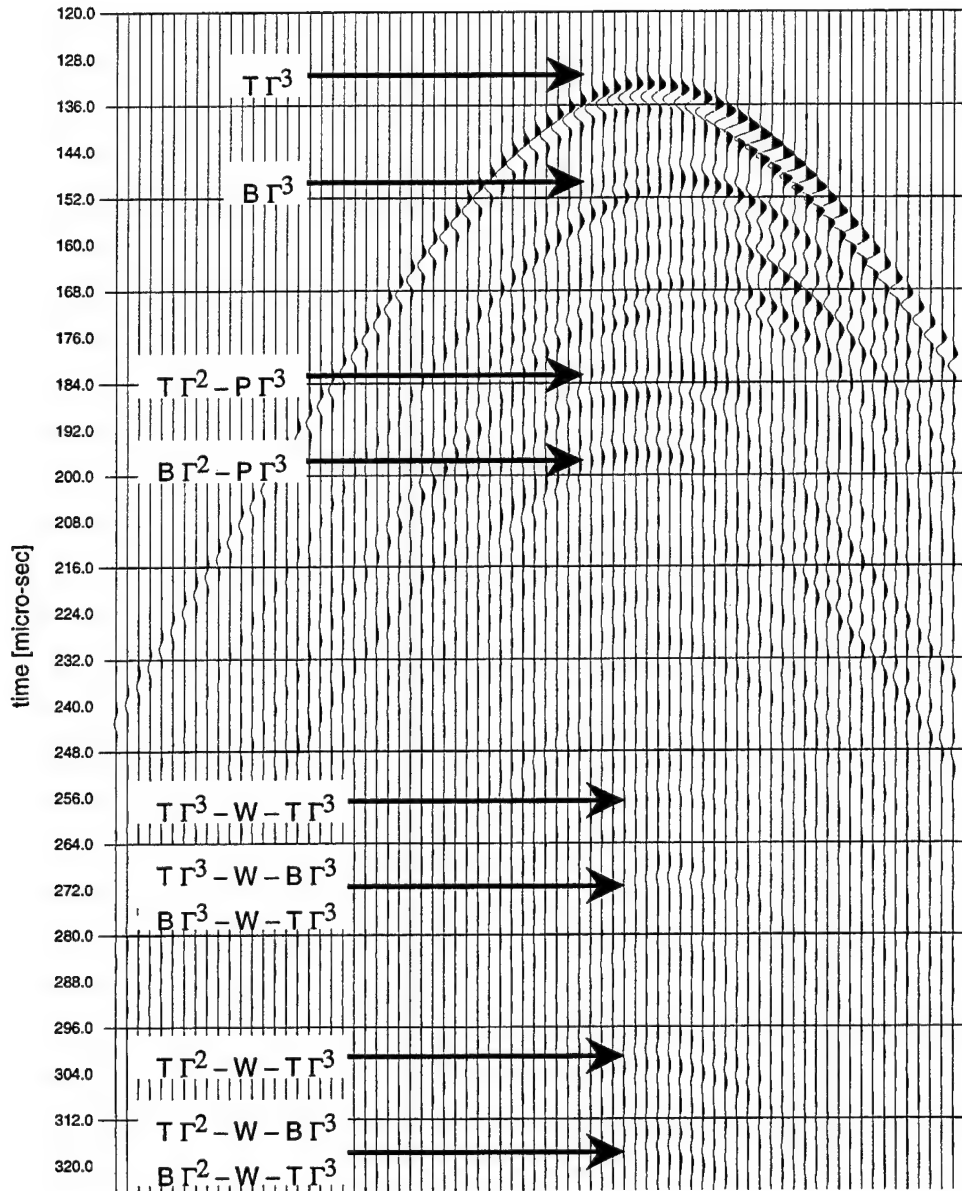Figure 10: Syncline model: The scattered field emanated by Γ^2 into the fluid.

Figure 11: Syncline model: The scattered field emanated by Γ^3. The events around $180\,\mu s$ are reflections from scatterer Γ^2 passing through scatterer Γ^3. The events at $260\,\mu s$ are reflections from Γ^3 bouncing between the water surface and scatterer Γ^3. The events at $300\,\mu s$ are reflections from scatterer Γ^2 bouncing between the surface and scatterer Γ^3.
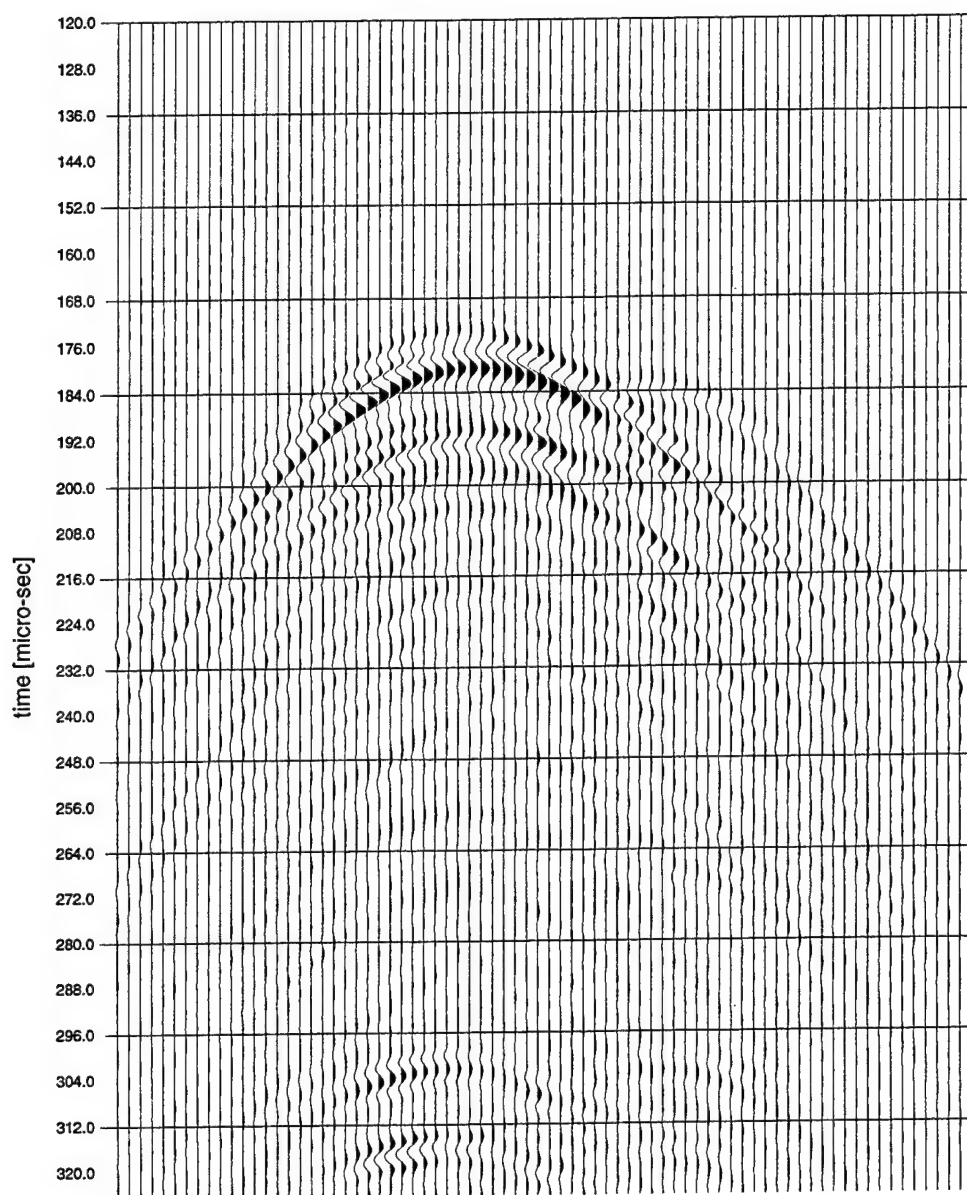
Figure 12: Syncline model: The residual field between the complete MMP solution (Figure 8) and the three scattered wavefields calculated for each rod separately.
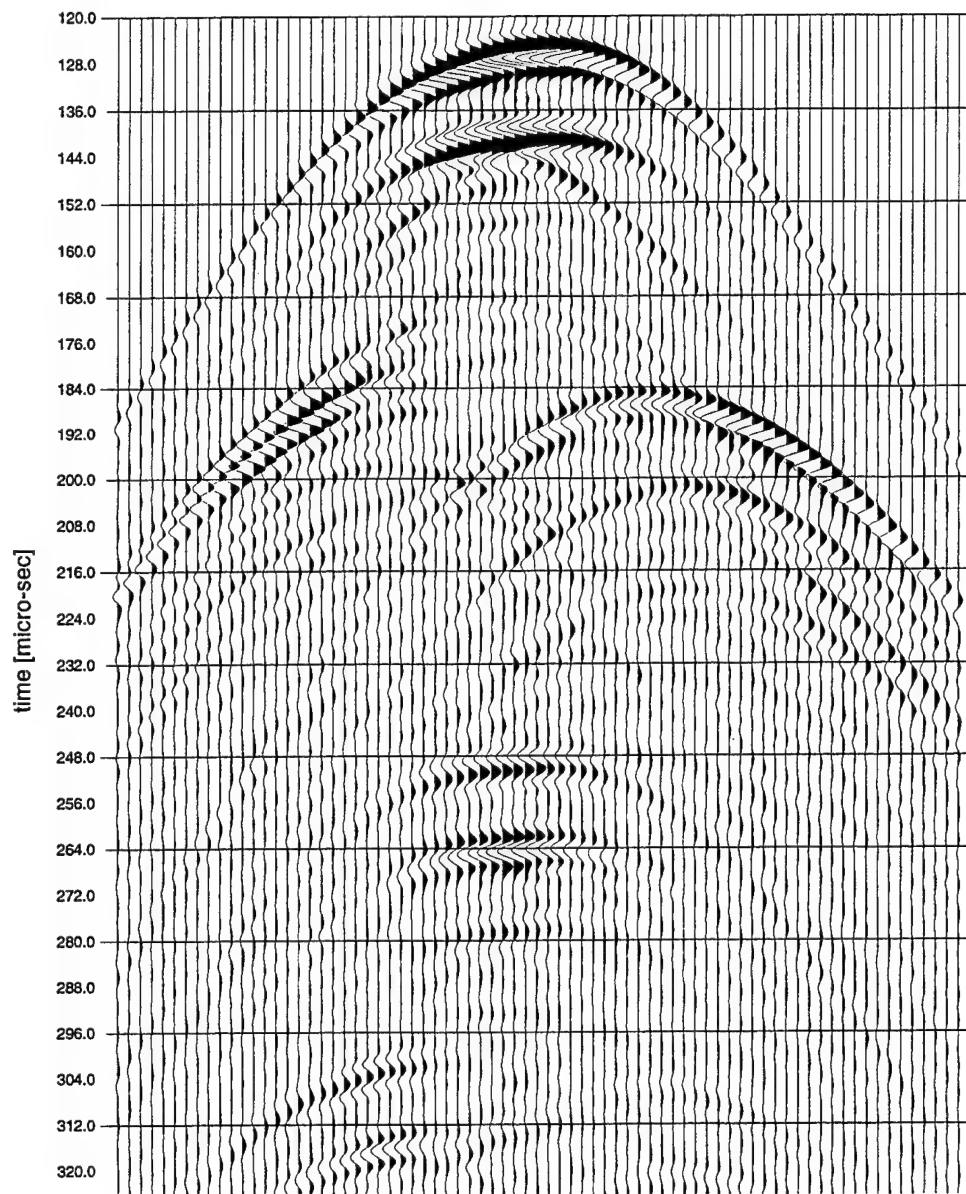
Figure 13: The seismogram for the anticline model defined in Figure 2 as calculated by the MMP method.
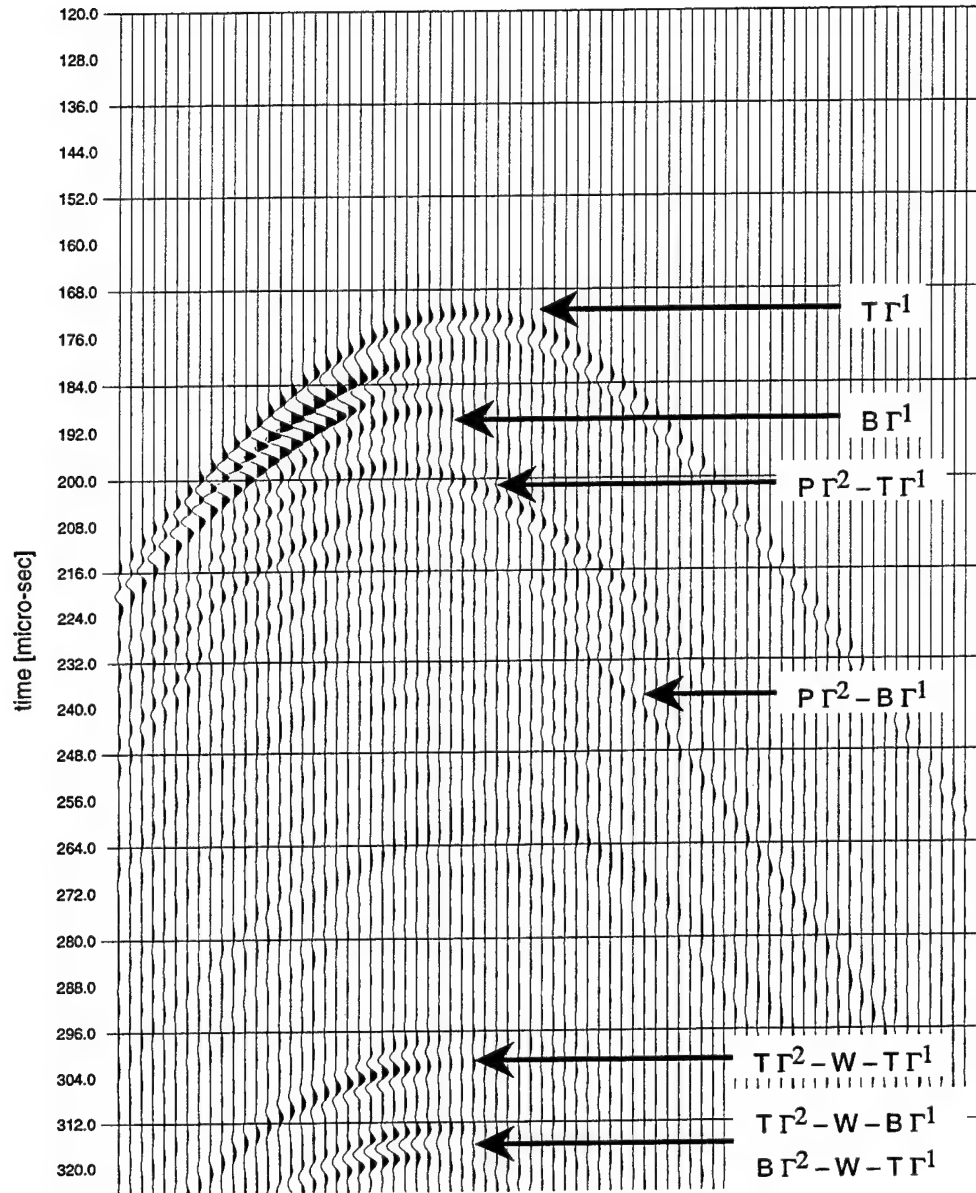
Figure 14: Anticline model: The scattered field emanated by Γ^1. The events at $300\,\mu s$ are reflections from Γ^2 bouncing between the surface and scatterer Γ^1. The symbol 'T' denotes a reflection from the top of the following scatterer, 'B' reflection from the bottom, 'W' reflection from the water surface, and 'P' means passes through the scatterer.

32
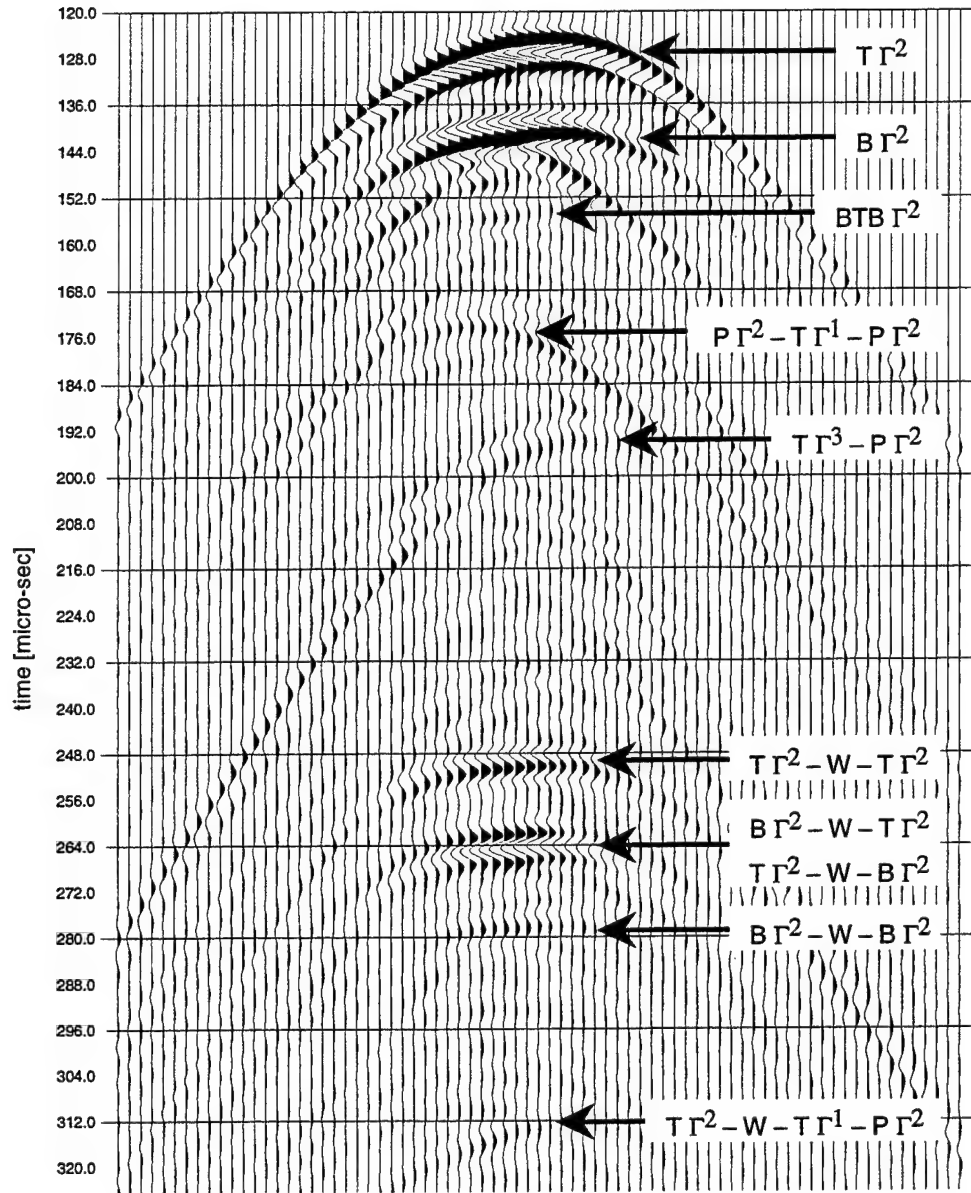
Figure 15: Anticline model: The scattered field emanated by Γ^2 into the fluid. The events at $170\,\mu$s and $190\,\mu$s are the reflections from Γ^1, respectively Γ^3, being transmitted through Γ^2.
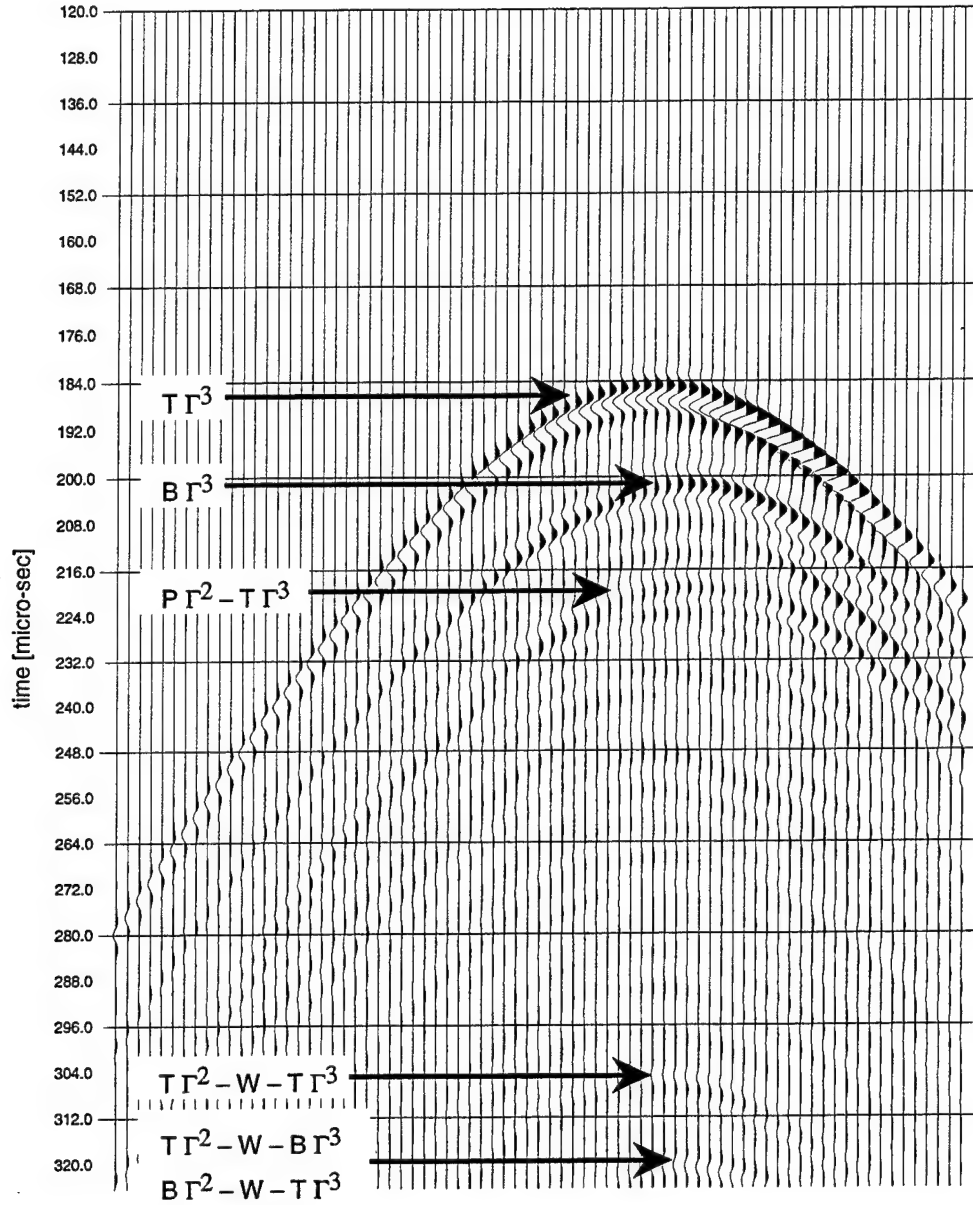
Figure 16: Anticline model: The scattered field emanated by Γ^3. The events at $300\,\mu s$ are reflections from scatterer Γ^2 bouncing between the surface and scatterer Γ^3.
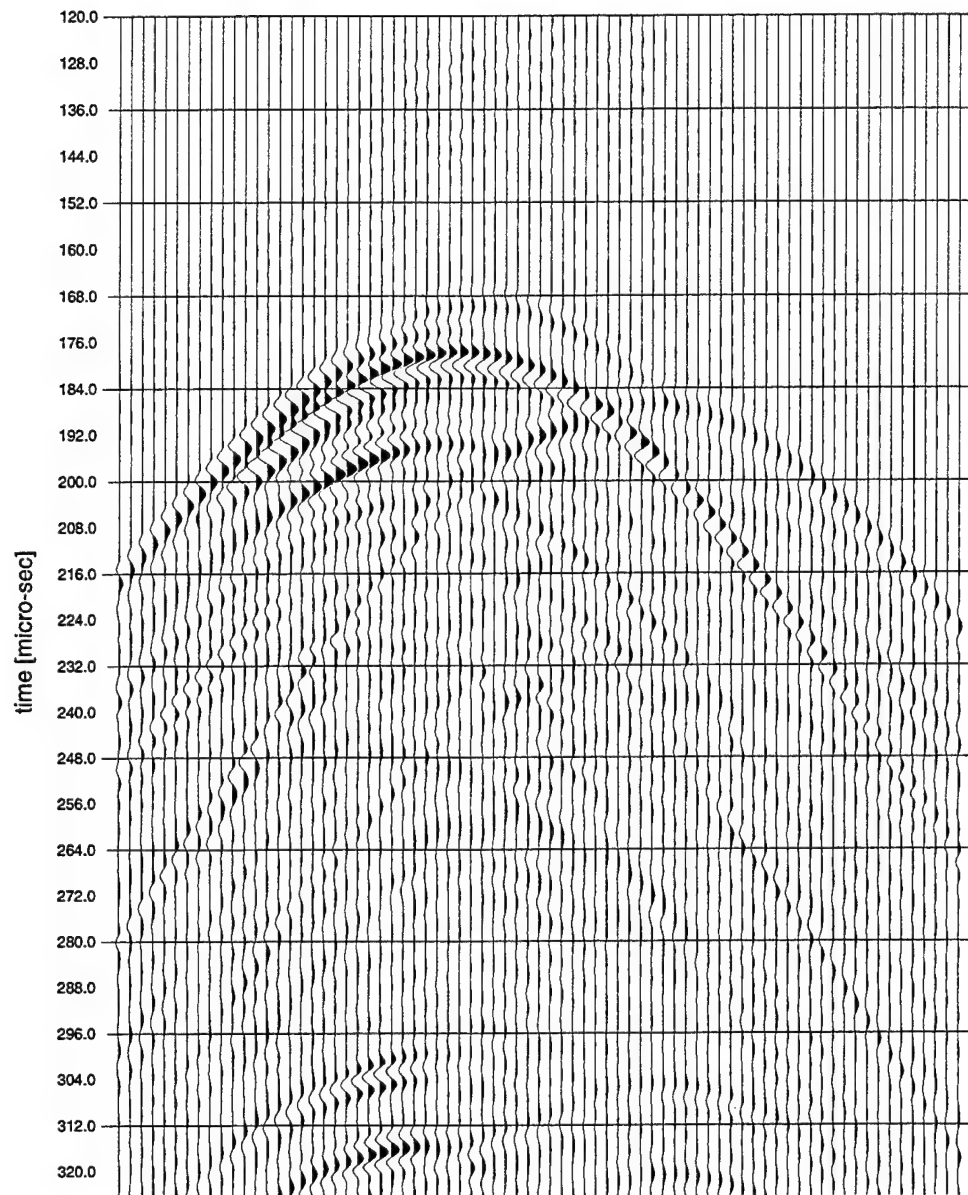
Figure 17: Anticline model: The residual field between the complete MMP solution (Figure 13) and the three scattered wavefields calculated for each rod separately.

Seismic Radiation From Explosively Loaded Cavities in Isotropic and Transversely Isotropic Media[*]

R. L. Gibson, Jr., M. N. Toksöz, and W. Dong[†]

Earth Resources Laboratory

Department of Earth, Atmospheric, and Planetary Sciences

Massachusetts Institute of Technology

Cambridge, MA 02139

Abstract

We analyze the influence of cavity shape on far-field seismic wave radiation from small explosion sources in isotropic and transversely isotropic media using the indirect boundary element method (BEM). The analysis utilizes two possible mathematical models for the pressure fields generated by the explosion in the acoustic medium inside the cavity. One simple model for the source is a volume injection (explosion) point source inside the cavity, which generates a pressure field that arrives approximately instantaneously at each point on the cavity wall. The amplitude of the field decays at a rate inversely proportional to propagation distance. We use this model to compare results with finite differences solutions, and the test confirms the accuracy of the BEM implementation. Strong compressional and shear signals propagate into the far-field from the source cavity, and the compressional wave amplitude depends strongly on direction of propagation. The behavior is similar at frequencies up to 200 Hz, including those typical of regional seismic wave propagation (1 to 10 Hz).

A second model of the source, one that has been applied in previous analytical and numerical work, is to assume that the explosion will instantaneously and *uniformly* pressurize the source cavity. This approach yields a radiation pattern that is very different from the point source model. The compressional wave radiation patterns have a large variation in signal strength and very strong shear waves when frequencies up to 200 Hz are included, but seismograms computed for frequency ranges of interest in regional wave propagation (around 1 Hz) have a nearly isotropic compressional wave radiation pattern and a much smaller shear wave. This shear wave is largest for long, tunnel-like cavities or short, disk-like cavities. When the cavity is located in a transversely isotropic medium, quasi-shear waves are generated, but, for the media we consider, their magnitude *decreases* for long, tunnel-like cavities and is larger for more equidimensional cavities. These somewhat counterintuitive results show that anisotropy can actually cause a radiation pattern to appear more isotropic

than the corresponding wavefields in an isotropic medium.

Introduction

Analysis of seismic waves generated by nuclear explosions is complicated by several factors. For example, spall and tectonic release processes contribute strongly to far-field seismic wave signals, and the classic explosion source model, which yields an isotropic compressional wave radiation pattern, cannot reproduce observed waveforms (e.g., Wallace et al., 1983, 1985; Priestley *et al.*, 1990; Patton, 1991; Schlittenhardt, 1991). Changes in source cavity shape and source location within the cavity also can influence the radiation pattern of the explosion. Zhao and Harkrider (1992) developed solutions for the displacement field created by an explosion source located off-center within a solid sphere embedded in an infinite solid medium, a model of a fully tamped explosion. Here the loss of symmetry causes shear waves to be generated, even with the spherical cavity. Other analyses have examined instead the effect of varying the cavity shape. Glenn et al. (1985, 1986), Rial and Moran (1986) and Glenn and Rial (1987) considered ellipsoidal and cylindrical cavity shapes, and, applying a combination of numerical and approximate analytical methods, obtained estimates of far-field radiation patterns. They suggested that the P-wave radiation would be strongest perpendicular to an ellipsoidal cavity and that a fairly strong S-wave would be generated as the cavity aspect ratio (ratio of length to diameter) became large. Stevens *et al.* (1991) also examined an ellipsoidal cavity. However, in contrast with the earlier results, they concluded that at the frequencies of interest for regional wave propagation, the P-wave radiation pattern would be fairly isotropic and S-wave amplitudes comparatively small.

We continue these investigations by using the indirect boundary element method (BEM) to simulate the seismic wavefields generated by explosions in cylindrical cavities. The BEM is a method for the computation of full waveform synthetic seismograms that discretizes boundaries in an earth model into elements and then replaces them with fictitious, secondary

sources (Chew, 1990). It has recently been applied to seismic exploration problems where a source is located inside infinite and semi-infinite cylindrical boreholes (e.g., Bouchon, 1993; Dong, 1993; Dong *et al.*, 1995; Dong and Toksöz, 1995). One major advantage of this approach is that unlike finite difference schemes it does not require discretization of the entire earth model and can therefore be used to compute wavefields at large distances from a comparatively small borehole. We have now extended the method to apply to a cylindrical explosion source cavity of finite length. This cavity model could represent, for example, a horizontal tunnel or a vertical shaft containing an explosive device. The cavity is assumed to be filled with an acoustic medium, and it is embedded within an infinite, homogeneous elastic medium. This elastic material can be either isotropic or transversely isotropic with the axis of symmetry parallel to the cavity axis. Once velocities and elastic constants are specified for the two media, the BEM gives full waveform synthetic seismograms corresponding to the seismic wavefields produced by a source inside the cavity and receivers in the elastic formation. Assuming the the explosion is a small, fully decoupled event, we can apply this linear simulation to the computation of far-field synthetic seismograms.

After describing the BEM in more detail below, we present computational results using two different mathematical models for the cavity source. First, we examine the far-field seismic waves generated by a volume injection point source located on the axis of the cavity. A major incentive for using this source model is that it was available in existing finite difference codes and therefore allowed a straightforward calibration of the BEM. A comparison of results from the two methods shows that our implementation of the BEM is accurate. We next present radiation patterns varying both cavity shape and location of the source within the cavity, noting that the strength of the incident pressure field depends on distance from the source. Radiation patterns show strong variations in P-wave amplitude and strong S-waves at all frequencies considered.

The second source model we consider makes the assumption that the explosion instantaneously and uniformly pressurizes the cavity, so that the source location within the cavity

is no longer a relevant parameter. This model is probably a more realistic description of the explosion process, and it has been applied frequently in the past (e.g., Stevens *et al.*, 1991; Patton, 1991). It also yields radiation patterns that are quite different from the point source model. The results we present below show that at low frequencies (1 Hz) the source creates a more nearly isotropic P-wave radiation pattern and that the S-wave is relatively small, though it depends on cavity aspect ratio. The solutions from this low frequency range up to 200 Hz are similar to the results of Stevens *et al.*(1991), and they suggest that placing a source inside a tunnel instead of a more equidimensional source cavity may not generate very strong variations in far-field seismic waves. Continuing with the instantaneous pressurization model, we apply it to the computation of radiation patterns for both hard and soft rock formations to show the dependency of the wavefields on formation properties. In addition, we also present the radiation patterns for hard and soft transversely isotropic media. The solutions for these media demonstrate that the quasi-shear wave generated by an explosion source can actually be smaller than the analogous results for isotropic formations when the cavity has a large aspect ratio. Hence we make the somewhat surprising prediction that an explosion in an anisotropic medium may generate less shear energy than the equivalent source located in an isotropic formation, a result that can be explained by considering equivalent moment tensor representations of the sources.

Boundary Element Method

The indirect boundary element method (BEM) has recently been applied to the calculation of acoustic and elastic wavefields in and around infinite boreholes in both homogeneous and plane layered media (Bouchon, 1993; Dong, 1993; Dong *et al.*, 1995; Dong and Toksöz, 1995). In addition, the method has been extended for application to semi-infinite cavities to model the radiation from seismic sources on or near the bottom end of a borehole (Dong *et al.*, 1995). The basic idea of this approach is that the effects of the diffracting boundary on the

displacement fields in the elastic medium can be represented by a set of fictitious sources located on the boundary, the cavity wall. Once these fictitious sources and the Green's functions for the elastic medium are known, the wavefield generated by the source inside the cavity can be calculated for a point outside the cavity. Our work extends these earlier results to include the second end of the cylindrical cavity, allowing synthesis of the displacement fields generated by an explosion source located inside a tunnel.

Considering a point source in the acoustic medium on the axis of the cavity, the displacement field can be related to the following potential (Dong et $al.$, 1995):

$$\phi(\mathbf{x}) = \phi_i + \int_B dS' g(\mathbf{x}, \mathbf{x}') \psi(\mathbf{x}') \tag{1}$$

Here ϕ_i is the potential created by the point source, $g(\mathbf{x}, \mathbf{x}')$ is the scalar Green's function for the acoustic medium, and $\psi(\mathbf{x}')$ is an acoustic source distribution along the cavity wall. The integrand is evaluated on the cavity surface B. Equation (1) yields the displacement field $\mathbf{u}(\mathbf{x}, \omega)$ or pressure field $p(\mathbf{x}, \omega)$ anywhere in the cavity or on the cavity wall via

$$\mathbf{u}(\mathbf{x}, \omega) = \nabla \phi(\mathbf{x}, \omega), \qquad p(\mathbf{x}, \omega) = -\lambda \nabla^2 \phi(\mathbf{x}, \omega) \tag{2}$$

Similarly, the displacement field $\mathbf{U}(\mathbf{x})$ in the elastic medium surrounding the cavity is given by

$$\mathbf{U}(\mathbf{x}) = \int_B dS' \mathbf{G}(\mathbf{x}, \mathbf{x}') \cdot \mathbf{\Psi}(\mathbf{x}'). \tag{3}$$

Here $\mathbf{G}(\mathbf{x}, \mathbf{x}')$ is the Green's tensor for the medium, which in our implementation can be either isotropic or transversely isotropic with the axis of symmetry parallel to the cylinder axis (Dong et $al.$, 1995). The vector force source on the cavity wall is denoted by $\mathbf{\Psi}(\mathbf{x}')$ and consists of two components in the vertical and radial directions. Because of the axial symmetry inherent in the prescribed geometry of the source and cylindrical cavity, the third component of the force vector is identically zero.

The numerical algorithm begins by discretizing the wall of the cylindrical cavity into rings on the cylinder and into circular annuli on the top and bottom capping surfaces (Figure 1).

42

In general, there must be at least 3 elements within the smallest wavelength involved in the calculation. The sources are assumed to be constant on each element, and the magnitudes of these acoustic and force sources are determined by enforcing boundary conditions on each element. These conditions are the continuity of the normal components of stress and displacement and the vanishing of the tangential stress in the solid at the boundary between the acoustic and elastic media. By writing these equations in matrix form, we obtain a system which can be solved for the source strengths on each of the N_e elements:

$$\sum_{i=1}^{N_e} A_{ji}^f V_i^f + \sum_{i=1}^{N_e} A_{ji}^v F_i^v + \sum_{i=1}^{N_e} A_{ji}^r F_i^r = D_j^u \tag{4}$$

$$\sum_{i=1}^{N_e} B_{ji}^f V_i^f + \sum_{i=1}^{N_e} B_{ji}^v F_i^v + \sum_{i=1}^{N_e} B_{ji}^r F_i^r = D_j^{\sigma_{rr}} \tag{5}$$

$$\sum_{i=1}^{N_e} C_{ji}^v F_i^v + \sum_{i=1}^{N_e} C_{ji}^r F_i^r = D_j^{\sigma_{rz}} \tag{6}$$

A_{ji}^f, A_{ji}^v, and A_{ji}^r are the displacement fields at the jth element created by the volume injection, vertical force and radial force sources, respectively, on the ith element. They are determined by integrating the Green's functions over each element. In the same way, the quantities B and C are the radial and tangential stresses on each element. The variables D, following similar notation conventions, are the exciting fields, or incident wavefields generated by the acoustic source, on each element. There are a total of $3N_e$ equations, which can be solved for the acoustic sources V_i^f and force sources F_i^r, F_i^v once the different acoustic and elastic displacement and stress fields are known. These are computed using discrete wavenumber methods to evaluate integrals over horizontal wavenumber for the three types of media involved in our simulations (acoustic, isotropic and transversely isotropic) (Dong et al., 1995).

In our calculations, we have utilized two different models of the exciting wavefields D. The first approach was to consider a point source inside the cavity. The incident pressure and displacement can then be computed using a discrete wavenumber integral solution. When

the acoustic velocity in the cavity is very high, the arrival time differences of the wavefield along the cavity wall will be negligible, though the amplitude will inversely proportional to distance from the source. A second model of the source field is to assume instantaneous pressurization of the cavity by the explosion so both the amplitude and the arrival time of the pressure signal are constant. This assumption is commonly made in the analysis of nuclear explosions in spherical cavities (e.g., Patton, 1991). To apply this source model, we simply set $D_j^u = D_j^{\sigma_{rz}} = 0$ and $D_j^{\sigma_{rr}} = 1.0$ as the source condition. Below we show results for both source models, demonstrating the accuracy of the BEM and also highlighting the difference in radiation patterns predicted by the two different methods.

Radiation Pattern Results

Point Source

We applied the indirect BEM to point sources in cylindrical cavities in a hard rock medium with P-wave velocity 4000 m/s, S-wave velocity 2200 m/s, and density 2200 kg/m^3. The acoustic velocity and density of the cavity filling material were set to 10000 m/s and 0.129 kg/m^3, respectively, to model a rapid pressure wave generated by an explosion. A comparison of BEM results with finite difference simulations provides a useful demonstration of the accuracy and rapid computation speed of the BEM, and we implemented this test with a cylindrical cavity model of length 160 m and radius 40 m (with aspect ratio, the ratio of length to diameter, therefore equal to 2). Receivers were located at a constant distance of 1250 m from the cavity center, these locations covering the entire range of angles from along the cavity axis to perpendicular to this axis in order to estimate radiation patterns. This comparatively small distance of the receivers was used to make computation time with the finite difference algorithm practical, since a relatively fine discretization of the model is required to accurately model the source cavity. A major disadvantage of finite differ-

44

ence methods for modeling source behavior is this discretization requirement, as increasing source/receiver distances to more realistic values greatly increases computation times. Because this distance was so small, we also set the center frequency of the source time wavelet to 8 Hz to obtain far-field radiation patterns. Comparisons of the synthetics seismograms from the two algorithms show that the results are essentially identical (Figure 2), but with these parameters, the finite difference simulation required about 13 hours to computed 1 sec time series on a Digital Alpha workstation, compared to about 2 hours 45 minutes for the BEM. The latter computation computed frequency domain results up to 34 Hz, yielding synthetic seismograms 3.75 sec in length. For this modeling task, the BEM clearly is a more useful tool than finite differences.

Another important advantage of BEM not revealed by this comparison is that it provides the complete solution with no auxiliary computations. Other approaches to modeling radiation from source cavities couple two methods, one for near source propagation, another for propagation to the far-field. For example, the representation theorem can be used to estimate far-field solutions after an initial computation with finite differences or finite elements (e.g., Glenn *et al.*, 1985; Stevens *et al.*, 1991). The BEM avoids a second step by directly computing the wavefields at an arbitrary distance.

Radiation patterns were estimated for the BEM and finite difference seismograms by rotating the vertical and horizontal traces into components parallel and perpendicular to the propagation direction to isolate the compressional and shear waves, respectively, on different traces. The amplitudes were then estimated by taking the maxima of the envelopes of the individual traces. While there are some slight differences in these radiation patterns, the results are clearly very close and this test confirms that the BEM works accurately (Figure 3).

In order to explore the dependence of the radiation pattern on cavity size, we computed radiation patterns for a several cavity shapes using the BEM (Figure 4). Each cavity model had a length of 80 m, and the radius of the cavity was increased in order to decrease the aspect ratio. The source was at the center of the cavity. Receivers were located at a distance

45

of 10000 m to examine far-field radiation patterns, and the frequency domain response was convolved with a wavelet having a dominant frequency of 1 Hz. As the aspect ratio diminishes, the P-wave pattern tends to become more isotropic, while the S-wave amplitude decreases relative to the P-wave. For larger aspect ratios, which might be more realistic models of tunnel source cavities, the S-wave is as large as the compressional wave signal.

Variations in aspect ratio clearly yield significant changes in radiation pattern, but another important variable for the point source explosion model is the location of the volume injection source within the cavity. Though the method as currently implemented requires the source to be on the axis of the cavity, we are free to move it anywhere along this axis. In Figure 5, we show radiation patterns for the cavity with an aspect ratio of 5 where the source is located at several different points between the center of the cavity and one end. As the source approaches the end of the cavity, the radiation pattern becomes essentially identical to that of a single point force in an infinite elastic medium. This variation in the far-field signals generated by the source is caused by the variation of incident amplitude with distance from the source. Since the amplitude is inversely proportional to distance, the incident field at the far end of the cavity is almost two orders of magnitude smaller than that at the near end when the source is located 1 m from the end. Hence, the reradiation of energy by the closer end of the cavity dominates the wavefields.

Instantaneous Pressurization Source

Like the point source, the instantaneous cavity pressurization source model will be a function of cavity aspect ratio, though the position of the explosive device within the cavity is obviously irrelevant. In Figure 6 we compare the spectra from 0.1 to 200 Hz of the far-field displacements computed with the volume injection point source and cavity pressurization models. Spectra were computed for angles of 3, 45 and 87 degrees from the axis of symmetry in order to avoid slight numerical instabilities inherent in the method for the angles of 0 and

46

90 degrees. The results in Figure 6A show that the spectrum for the pressurization model displays a flat response out to a corner frequency that depends on the direction of observation. This corner frequency, around 50 Hz, is larger for propagation perpendicular to the cavity axis than along that axis. In addition, most of the difference in amplitudes is found at frequencies well over 10 Hz. Similar results were obtained by Glenn *et al.* (1985, 1986) and Stevens *et al.* (1991). However, the point source spectrum shows a linear behavior for frequencies from 0.1 to approximately 50 Hz, (Figure 6B) and the difference in amplitudes is fairly constant throughout the frequency range displayed in the figure.

One very important feature of the instantaneous pressurization spectra (Figure 6A) is that most of the directional variation occurs for frequencies larger than 50 Hz. The radiation pattern for the step function response does predict a large variation in amplitude of the P-wave with observation direction relative to the cavity axis, much like the point source (Figure 7). The shear wave amplitude is also relatively large compared to the compressional signal. However, when the synthetic seismograms are produced by convolving the spectral domain response with a Ricker wavelet of 1 Hz to examine the lower frequencies that are more typical of regional or teleseismic wave propagation, the S-wave strength is reduced compared to the P-wave and the compressional wave amplitude is nearly independent of propagation direction (Figure 8). In this situation, the point source still shows a strong shear wave, but the pressurization source model now displays a uniform P-wave radiation pattern and a much smaller S-wave.

Behavior of the pressurization source is further demonstrated in Figure 9, where we show compressional and shear wave radiation patterns obtained by convolving the frequency domain displacement field with a Ricker wavelet with a 1 Hz center frequency for several aspect ratios. Computations for this figure used a constant cavity radius of 4 m and varied the length to assess the effect of changing aspect ratio. The shear wave is smallest relative to the P-wave for aspect ratio near 1.

47

Low Velocity Formation

The radiation pattern of the pressurization source will have some dependence on the velocity of the surrounding elastic medium as well as on the shape of the cavity. Radiation patterns for a soft rock formation are similar to those obtained for the hard rock formation (Figure 10). The P and S-wave velocities of the soft rock medium are 2290 m/s and 980 m/s, respectively, and the density is 2250 kg/m^3. These velocities are approximately those of the Pierre Shale, which is actually transversely isotropic (White *et al.*, 1983). The principal difference between these patterns and those in Figure 9 is that the radiated fields in the shale are much larger. If we were to represent the cavity source by an equivalent moment tensor source, the far-field amplitude of the displacement field would be inversely proportional to the cubed velocity of the formation, which explains the larger amplitudes in the slow medium (Ben-Menahem *et al.*, 1991). At the same time, the interaction of the cavity with the medium will change, leading to a different equivalent moment tensor solution. The largest P-wave amplitudes compared to S-waves are found for aspect ratio 1.25 in the hard rock formation and for aspect ratio 2.5 in the soft rock. Hence, it is clear that the equivalent moment tensors in the two media are somewhat different, leading to subtle differences in seismic wave radiation.

Transversely Isotropic Media

Aligned Fractures

A medium containing aligned cracks is a realistic example of a material that is effectively anisotropic for long wavelengths (Hudson, 1980, 1981). This transversely isotropic medium can be incorporated in the BEM calculations when the axis of symmetry is parallel to the cylindrical cavity axis, which occurs when the cracks are perpendicular to the axis. If the cavity represents a horizontal tunnel, then the aligned fractures would all be vertical.

We estimated the elastic constants of such a material using the theory of Hudson (1980,

1981), in which the effective elastic constants of the anisotropic medium are given in terms of the isotropic parameters of the unfractured rock plus perturbation terms accounting for the effects of the aligned cracks. We used the velocities of the isotropic material from the radiation pattern computations shown above for the background parameters. The perturbations were computed using a crack density $\xi = na^3 = 0.05$ (n=number density of cracks, a=radius of the penny-shaped cracks) and assuming dry (empty) cracks. Table 1 displays the elastic constants of both the isotropic material and the composite medium with cracks, while Figure 11 shows the phase velocity variations of the three wave types, the quasi-compressional wave (qP), the fast quasi-shear wave (qS$_2$) and the slow quasi-shear wave (qS$_1$). If the cavity axis is defined as the z−axis, then the qS$_1$-wave is polarized in the vertical plane containing the ray from source to observation point and will be called the qSV wave for simplicity.

The qP-wave radiation patterns for the explosion source are very similar in magnitude and shape to those obtained for the isotropic formation (Figure 12). However, the qSV radiation patterns show different amplitude variations than the isotropic case. Figure 13 emphasizes this point by directly comparing radiation patterns for the isotropic and anisotropic media at aspect ratios of 5 and 1.25. The most interesting point is that the minimum qSV amplitude is found for the largest aspect ratio value of 5, and the relative amplitude increases monotonically with decreasing aspect ratio.

This result is at first somewhat counter-intuitive, since computations of radiation patterns using the classic, point source explosion model (three equal, mutually perpendicular dipoles) show comparatively large quasi-shear wave amplitudes (Mandal and Toksöz, 1991; Ben-Menahem *et al.*, 1991). However, this difference can be easily explained. The radiation patterns for the isotropic medium (Figure 9) correspond to the far-field radiation of a source consisting of two, equal and perpendicular horizontal dipoles and a smaller vertical dipole

49

(e.g., Glenn *et al.*, 1986; Rial and Moran, 1986). This moment tensor has the form

$$\mathbf{M} = \begin{bmatrix} D_h & 0 & 0 \\ 0 & D_h & 0 \\ 0 & 0 & D_v \end{bmatrix}, \tag{7}$$

where D_h and D_v are the magnitudes of the horizontal and vertical dipoles, respectively. The relative magnitudes of these two dipoles for the isotropic medium are straightforwardly estimated from the amplitudes of P-waves propagating in the horizontal and vertical directions, since all other factors affecting amplitudes are constant with direction. The amplitudes of the dipoles can also be measured for the anisotropic medium, but the variation in geometrical spreading with direction must be considered (Ben-Menahem *et al.*, 1991). Simple ray tracing procedures can be used to compute the spreading values for horizontal and vertical directions (e.g., Gibson *et al.*, 1991), showing that the moment tensors are almost identical for the isotropic and fractured media. For example, when cavity aspect ratio is 5, we find $D_v = 0.9D_h$. Computation of ray theoretical radiation patterns with this moment tensor representation confirm that the some moment tensor yields the radiation patterns in Figures 9 and 12.

This moment tensor representation of the source allows a simple explanation of the variations in qSV-wave amplitudes (Figure 12). In the anisotropic medium, there is a weaker dipole acting in the vertical direction, but at the same time, the material is "softer" in this direction (compare C_{11} and C_{33}, Table 1). Hence, it yields more easily to the applied source, and the overall response of the medium is nearly isotropic, at least compared to the isotropic hard rock medium, which displays the effects of the unequal dipoles in the source representation.

Transversely Isotropic Shale Formation

Another type of anisotropic medium that might occur in a nuclear test site is the transverse isotropy frequently observed in shale formations. Since the axis of symmetry in these formations is generally vertical, our simulation of the radiation from a finite length source cavity would correspond to a model of a vertical shaft in the shale formation. An example of such a formation is the Pierre Shale, in which White *et al.* (1983) performed a VSP experiment to estimate the five elastic constants of the medium. One of their estimates is shown in Table 2, and the phase velocities corresponding to these elastic constants are shown in Figure 14. Unlike the hypothetical fractured medium considered above, the quasi-shear wave polarized in the plane containing the cavity axis is faster than the horizontally polarized SH mode for angles less than approximately 30 degrees. In other words, for slowness vector angles within 30 degrees of the cylinder axis, the observed qSV-wave will correspond to the faster of the two shear wave velocities (qS_2). For larger angles, the qSV-wave will be associated with the slower phase velocity (qS_1).

Radiation patterns for the cavity source in the Pierre Shale display some of the same trends as did the source in the fractured medium (Figure 15). In particular, the S-wave amplitude increases with decreasing cavity aspect ratio. Like the cavities in the fractured medium, the moment tensor representations of the sources (equation (7)) are almost identical in the isotropic low velocity formation and the anisotropic shale. A comparison of the patterns for the isotropic and anisotropic shales also shows that the P-wave radiation pattern is slightly less isotropic for the anisotropic shale, with a somewhat diamond-like shape (Figure 16). The most significant difference from the patterns computed for the material with aligned fractures (Figure 12) is that the qSV-wave radiation pattern is larger relative to the qP-wave pattern. Another, more subtle, feature of the radiation patterns for the Pierre Shale is that the qSV-wave radiation patterns for aspect ratio 5 show small lobes oriented in the near vertical direction (Figure 15).

51

Discussion

The results presented above for the isotropic medium are, in general, similar to far-field displacement fields obtained in earlier work. Glenn *et al.*(1985) used finite element methods to solve for displacement fields on an ellipsoidal cavity surface and applied the representation theorem to determine the far-field displacements. Subsequent work continued this effort with an analytic model, finding that when aspect ratio is 10, the cylindrical and ellipsoidal cavities yield essentially the same radiation patterns (Glenn *et al.*, 1986). Likewise, Rial and Moran (1986) developed an analytical formulation representing the source as a set of dipoles (i.e., a moment tensor of the form shown in equation (7)). The relative amplitudes were described as a function of aspect ratio, so that as the aspect ratio approached one, all dipoles had the same magnitude ($D_v = D_h$) to yield the classical result for the spherical cavity. However, Glenn *et al.*(1986) and Rial and Moran (1986) both found for large aspect ratios that $D_v = 2/3D_h$. As discussed above, the BEM results for aspect ratio 5 correspond to $D_v = 0.9D_h$, a much weaker difference. The reason for this disagreement is not clear. It should also be noted that like Rial and Moran (1986), we find that the radiation patterns do not change significantly for aspect ratios over 5.

A result more similar to ours was obtained by Stevens *et al.* (1991), who simulated wavefields radiated from ellipsoidal cavities of aspect ratio 4 by coupling a non-linear, near-field finite difference computation with the representation theorem. Applying a pressure step to the cavity wall, they found a radiation pattern that showed strong variations in P-wave strength when frequencies up to 100 Hz were considered. However, filtering the signals with an anelastic attenuation operator to replicate results more relevant to regional observations yielded signals with almost no variation in amplitude with direction. This behavior is very similar to our results obtained with the BEM for cylindrical cavities.

Non-linear effects, which are neglected in the BEM computation, may also strongly influence the far-field radiation pattern of an explosion source. Stevens *et al.* (1991) showed

that the non-linear interactions of an air shock with the medium surrounding the cavity generated a P-wave radiation pattern that was even more isotropic than the pattern generated by the pressure step simulation. This suggests that the BEM results for the instantaneous pressurization model of the explosion should be considered an upper bound for the deviation of the radiation pattern from that of the isotropic, spherical source.

The neglect of non-linear effects in the BEM simulation could be worse when we consider the point source explosion model, especially when the source is near the end of the cavity (Figure 5). It is difficult to predict what the effect of such non-linearities on the radiation patterns might be, but the results discussed above for the sources centered in the cavity suggest that effect might be to reduce signal strength variations. Some data is available which helps to support this conclusion. Although field data where source cavity shape (for non-spherical cavities), source location and waveforms are all available are rather scarce, data from Russian experiments in the 1960's has recently become available (Murphy *et al.*, 1995). Several decoupling tests were conducted in a mine in the Tywya Mountains of Kirghizia, and the sources were located in both spherical and elongated cavities. The charges, chemical explosives, were also located at various points within the source cavities. Yields of the explosions were 0.1, 1 and 6 tons. Analysis of the data shows that there is little variation in peak displacement fields with changing cavity shape or source location (Murphy *et al.*, 1995). This suggests that numerical results predicting a relatively small dependence on cylindrical cavity aspect ratio are good.

Conclusions

The BEM is a useful approach for simulating the far-field radiation of explosion sources located in cylindrical cavities. We have applied it to the computation of radiation patterns for two different explosion models, a volume injection point source and an instantaneous, uniform pressurization of the cavity. While the wavefield generated by the point source

53

strikes the cavity wall at almost constant time, the amplitude of the incident field is inversely proportional to the distance from the source. Our computations show that the resulting radiation patterns are sensitive to both the cavity aspect ratio and to the position of the source along the cavity axis. When the source is near the end of the cavity, that reradiation of energy from this near end dominates the far-field signature and the resulting radiation pattern resembles that of a point force.

On the other hand, the instantaneous, uniform pressurization model of the source generates radiation patterns that are similar to the calculation results of Stevens *et al.* (1991) in that high frequency simulations yield P-wave radiation patterns with strong variations in amplitude. The corner frequency of the spectra changes with direction of observation. However, results filtered to frequencies more typical of regional wave propagation (1 Hz) have lower S-wave amplitudes and P-wave patterns that are nearly isotropic. These simulations suggest that the location of a source in a tunnel-like cavity would not have an extremely strong effect on regional seismograms. Application of this model to two transversely isotropic media shows that the predicted radiation patterns are fairly similar to the isotropic case. The principal difference is that the qSV-wave amplitude is smallest for large aspect ratios. This result shows that anisotropy does not necessarily increase the strength of shear wave energy created by an explosion source.

Acknowledgments

References

Ben-Menahem, A., R.L. Gibson, Jr. and A.G. Sena (1991). Green's tensor and radiation patterns of point sources in general anisotropic inhomogeneous elastic media, *Geophys. J. Int.* **107**, 297–308.

Bouchon, M. (1993). A numerical simulation of the acoustic and elastic wavefields radiated by a source in a fluid-filled borehole embedded in a layered medium, *Geophysics 58*, 475–481.

Chew, W.C. (1990). *Waves and fields in inhomogeneous media*, Van Nostrand Reinhold, New York.

Dong, W. (1993). Elastic wave radiation from borehole seismic sources in anisotropic media, Ph.D. thesis, Massachusetts Institute of Technology.

Dong, W., M. Bouchon, and M. N., Toksoz (1995). Borehole seismic source radiation in layered isotropic and anisotropic media: boundary element modeling, *Geophysics 60*, 735-747.

Dong, W., and M. N., Toksoz (1995). Borehole seismic source radiation in layered isotropic and anisotropic media: real data analysis, *Geophysics 60*, 748-758.

Gibson, Jr., R.L., A.G., Sena, and M.N. Toksöz (1991). Paraxial ray tracing in 3D inhomogeneous, anisotropic media, *Geophys. Prosp. 39*, 473–504.

Glenn, L. A., A. J. C. Ladd, B. Moran and K. A. Wilson (1985). Elastic radiation from explosively-loaded ellipsoidal cavities in an unbounded medium, *Geophys. J. R. astr. Soc., 81*, 231-241.

Glenn, L.A., B. Moran, A.J.C. Ladd, K. Wilson, J.A. Rial (1986). Elastic radiation from explosively-loaded axisymmetric cavities, *Geophys. J. R. astr. Soc.,, 86*, 119–136.

Glenn, L.A. and J.A. Rial (1987). Blast wave effects on decoupling with axisymmetric cavities, *Geophys. J.R. astr. Soc.* **91**, 229–239.

Hudson, J.A. (1980). Overall properties of a cracked solid, *Math. Proc. Camb. Phil. Soc.* **88**,

371–384.

Hudson, J.A. (1981). Wave speeds and attenuation of elastic waves in material containing cracks, *Geophys. J. R. astr. Soc.* **64**, 133–150.

Mandal, B. and M.N. Toksöz (1991). Effects of an explosive source in an anisotropic medium, in S.R. Taylor, H.J. Patton, and P.G. Richards (eds.), *Explosion Source Phenomenology*, American Geophysical Union, Washington, D.C., pp. 261–268.

Murphy, J.R., I.O. Kitov, N. Rimer, D.D. Sultanov, B.W. Barker, and J.L. Stevens (1995). Analyses o fthe seismic characteristics of U.S. and Russian cavity decoupled explosions, *in* J.F. Lewkowicz, J. M. McPhetres, D.T. Reiter, eds., Proceedings of the 17th Annual Seismic Research Symposium on Monitoring a Comprehensive Test Ban Treaty, PL-TR-95-2108, Phillips Laboratory, Hansom AFB, Massachusetts, ADA310037.

Patton, H.J. (1991). Seismic moment estimation and the scaling of the long-period explosion source spectrum, in S.R. Taylor, H.J. Patton, and P.G. Richards (eds.), *Explosion Source Phenomenology*, American Geophysical Union, Washington, D.C., pp. 171–184.

Priestley, K. F., W. R. Walter, V. Martynov and M. V. Rozhkov (1990). Regional seismic recordings of the Soviet nuclear explosion of the joint verification experiment, *Geophys. Res. Lett., 17*, 179-182.

Rial, J. A. and B. Moran (1986). Radiation patterns for explosively-loaded axisymmetric cavities in an elastic medium: analytic approximations and numerical results, *Geophys. J. R. astr. Soc., 86*, 855-862.

Schlittenhardt, J. (1991). The effects of spall on teleseismic P-waves: an investigation with theoretical seismograms, in S.R. Taylor, H.J. Patton, and P.G. Richards (eds.), *Explosion Source Phenomenology*, American Geophysical Union, Washington, D.C., pp. 141–150.

Stevens, J.L., N Rimer., J. Murphy, T.G. Barker, E. Bailey, E.J. Halda, W.J. Proffer, S.H. Rogers and B. Shkoller (1991). Simulation of seismic signals from partially coupled nuclear explosions in spherical and ellipsoidal cavities, MAXWELL S-CUBED Division, SSS-FR-91-12735, Final Report on Contract No. 90-N3039000-000.

56

Wallace, T.C., D.V. Helmberger, and G.R. Engen (1983). Evidence of tectonic release from underground nuclear explosions in long-period P waves, *Bull. Seism. Soc. Am., 73*, 593–613.

Wallace, T.C., D.V. Helmberger, and G.R. Engen (1985). Evidence of tectonic release from underground nuclear explosions in long-period S waves, *Bull. Seism. Soc. Am., 75*, 157–174.

White, J.E., Martineau-Nicoletis, L., and Monash, C. (1983). Measured anisotropy in Pierre Shale, *Geophys. Prosp.*, **31**, 709–725.

Zhao, L., and Harkrider, D.G. (1992). Wavefields from an off-center explosion in an embedded solid sphere, *Bull. Seis. Soc. Amer.*, **82**, 1927–1955.

Parameter	Background Value (GPa)	Perturbed Value (GPa)
C_{11}	35.2 GPa	33.8 GPa
C_{33}	35.2	26.0
C_{13}	13.9	10.3
C_{44}	10.6	9.53
C_{66}	10.6	10.6
ρ	2.2 g/cm^3	2.2

Table 1: Background elastic constants and perturbed values computed using the theory of Hudson (1980, 1981). Density is also shown. The background parameters correspond to P and S-wave velocities of 4000 m/s and 2200 m/s, respectively, and the perturbed values were obtained using a crack density of 0.05.

Parameter	Value
C_{11}	11.8 GPa
C_{33}	9.68
C_{13}	7.09
C_{44}	1.62
C_{66}	2.16
ρ	2.25 g/cm^3

Table 2: Elastic constants and density of Pierre Shale (White *et al.*, 1983).
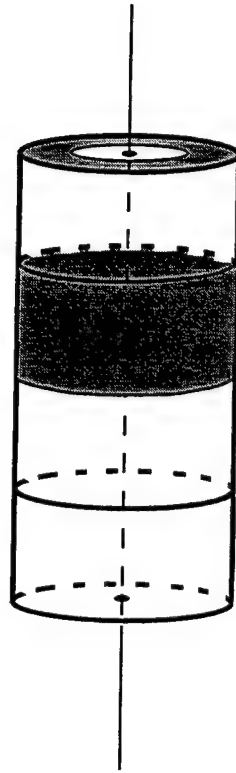
Figure 1: Schematic illustration of model discretization for the BEM. In general, both the ends and the cylindrical portion of the cavity are discretized as shown here. An example of an annulus element on the cavity end and a ring element on the cylinder are shaded in the figure.

FINITE DIFFERENCE

BEM

RADIAL COMPONENT

RADIAL COMPONENT

TANGENTIAL COMPONENT

TANGENTIAL COMPONENT
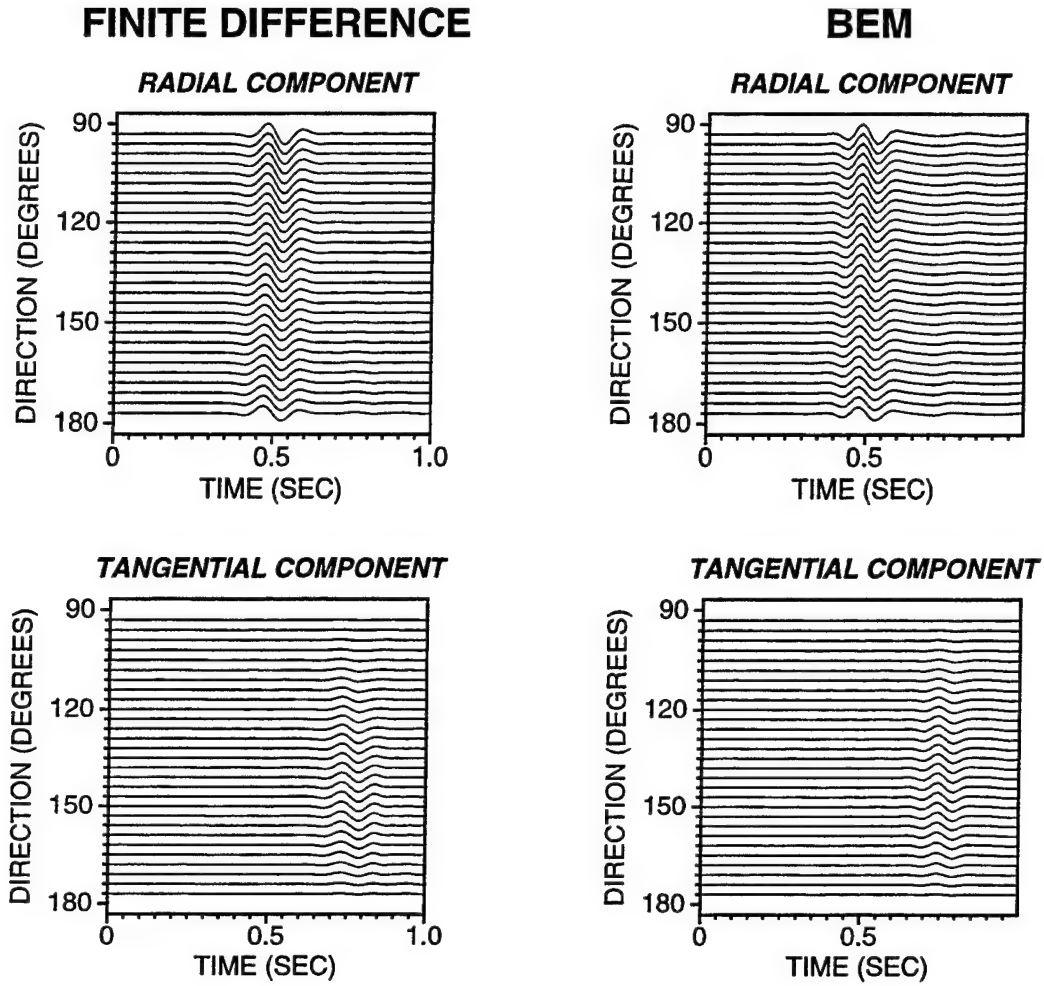
Figure 2: Synthetic seismograms computed for a cylindrical cavity in a hard rock isotropic formation with P-wave velocity 4000 m/s and S-wave velocity 2200 m/s. Other parameters are described in the text. Results obtained with the finite difference algorithm are shown in the left hand column, while BEM results are on the right. The observation angle for these seismograms ranges from 90 degrees (perpendicular to the cavity) to 180 degrees (along the cavity axis). P-wave signals are seen on the radial component, while the S-wave appears on the tangential component.

60
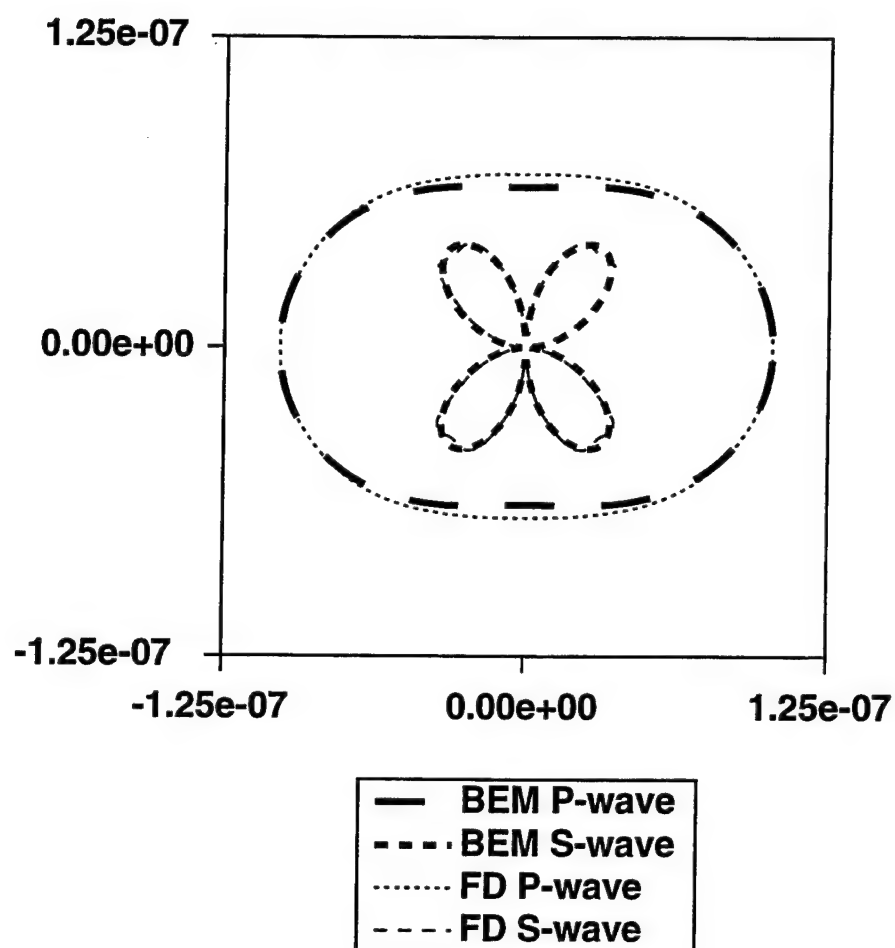
Figure 3: Comparison of radiation patterns computed using finite differences and the BEM (Figure 2). Cavity orientation in this figure is vertical.
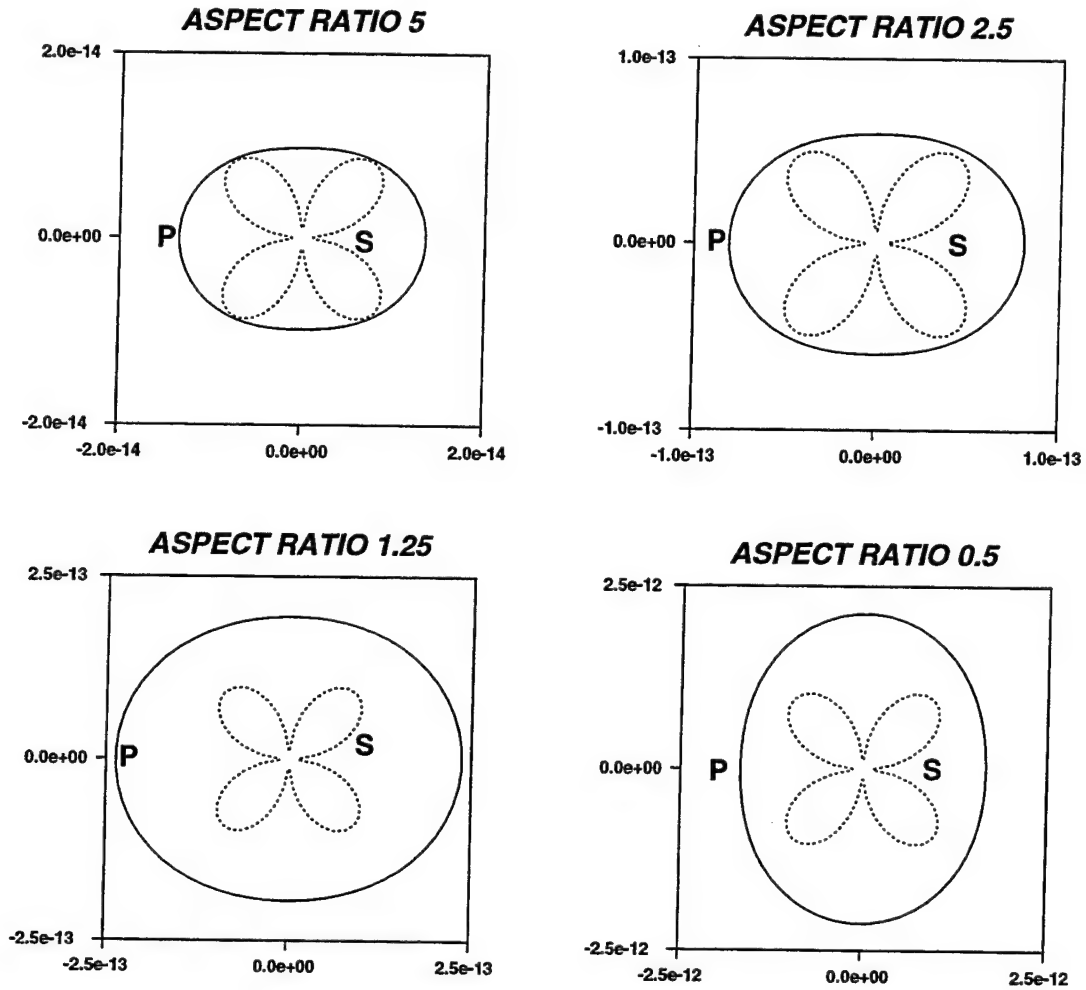
Figure 4: Radiation patterns created by a volume injection point source at the center of cavities of varying aspect ratio located in the hard rock isotropic formation (velocities in Figure 2). Since the dominant source frequency was specified to be 1 Hz, these patterns are representations of energy variations that might be observed at regional distances.
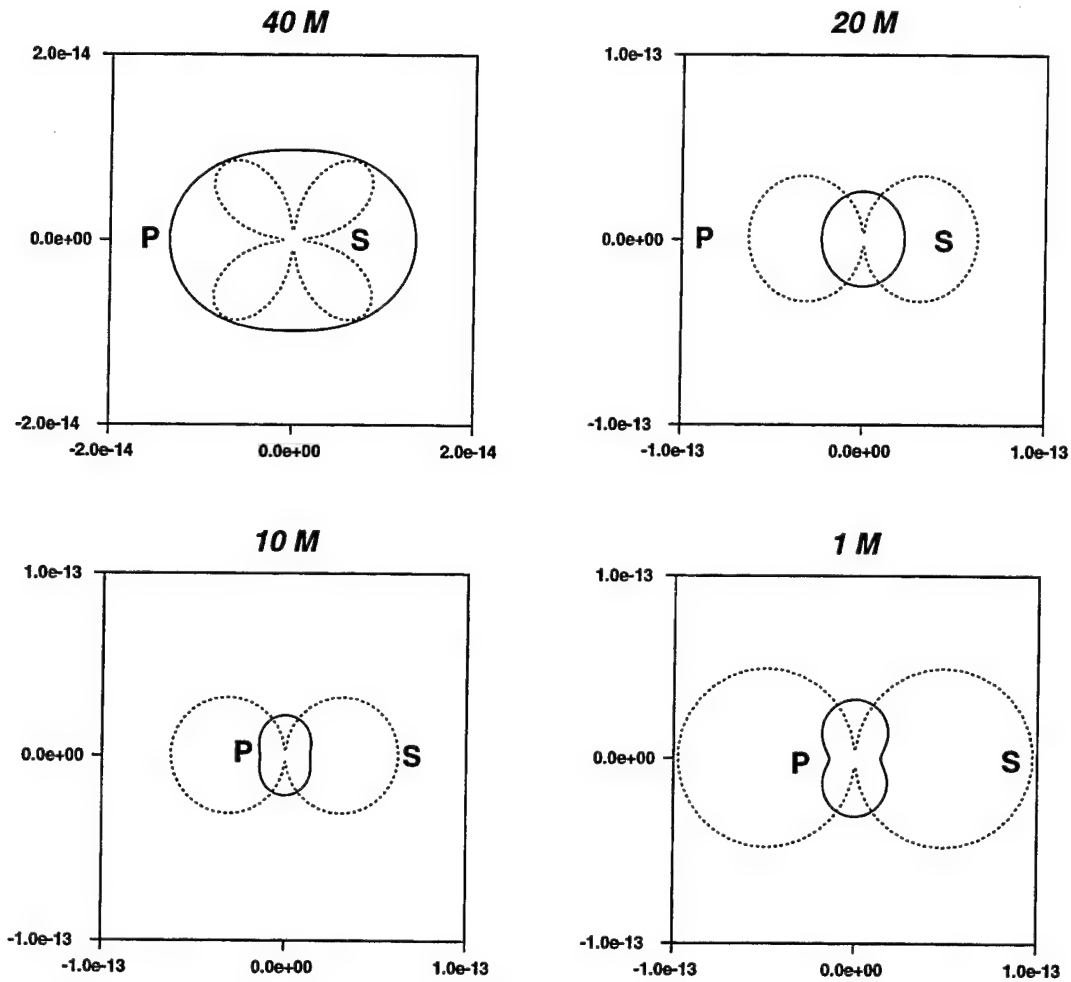
Figure 5: Radiation patterns created by a volume injection point source at varying positions along the axis of an 80 m long cavity with aspect ratio 5. The medium is the hard rock formation (medium properties are specified in Figure 2). The numbers at the top of each plot show the distance of the source from the end of the cavity. Therefore, the pattern at the upper left corresponds to the source at the center of the cavity and is identical to the plot in the upper left corner of Figure 4.

63
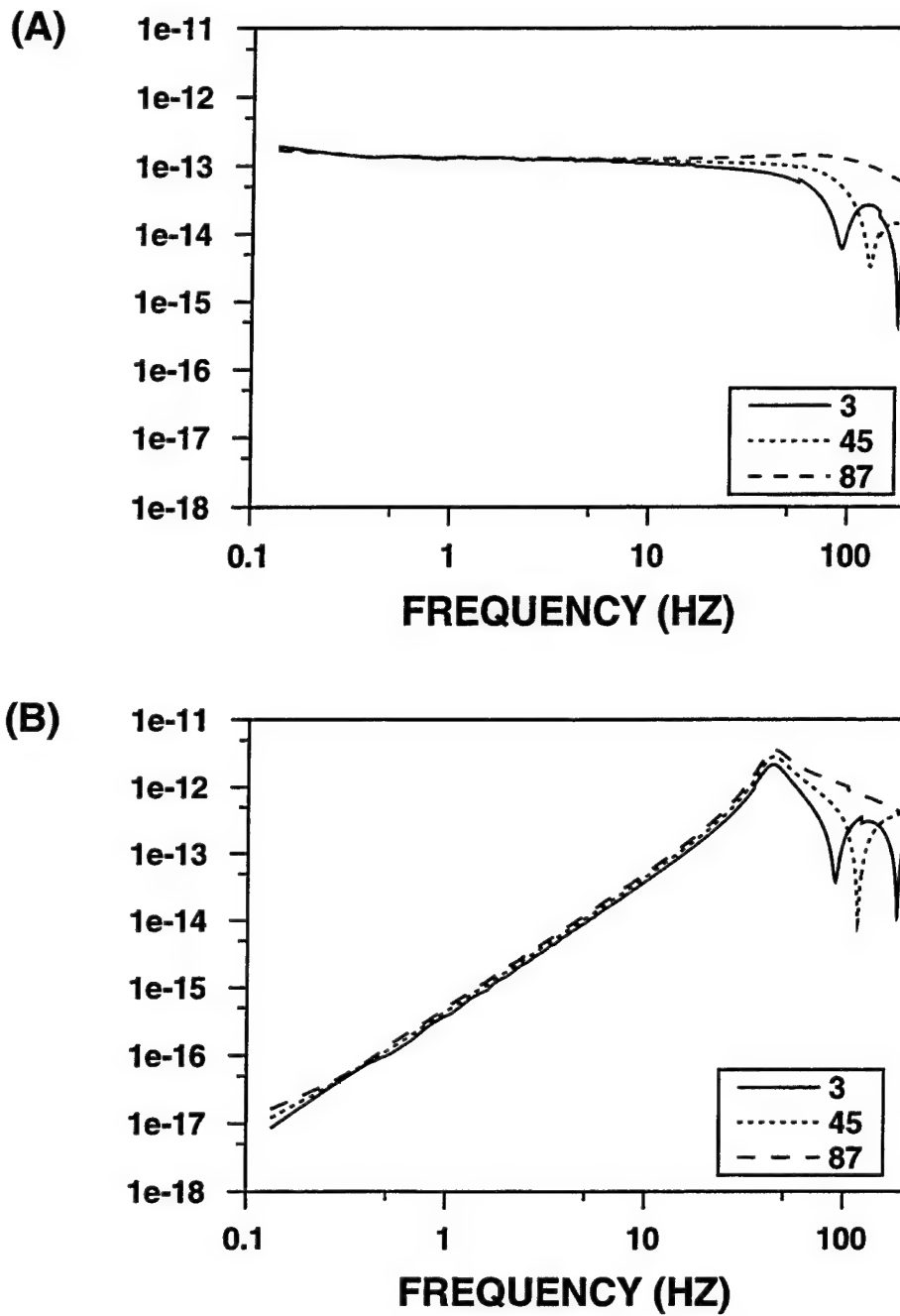
Figure 6: Log-log plot of the spectra of the wavefields generated by the (A) instantaneous pressurization and (B) volume injection point source models in the cavity of aspect ratio 5 (isotropic formation). The volume injection source was centered in the cavity. The hard rock formation velocities are given in Figure 2. Each plot shows the spectrum observed at 3, 45 and 87 degrees from the cavity axis.
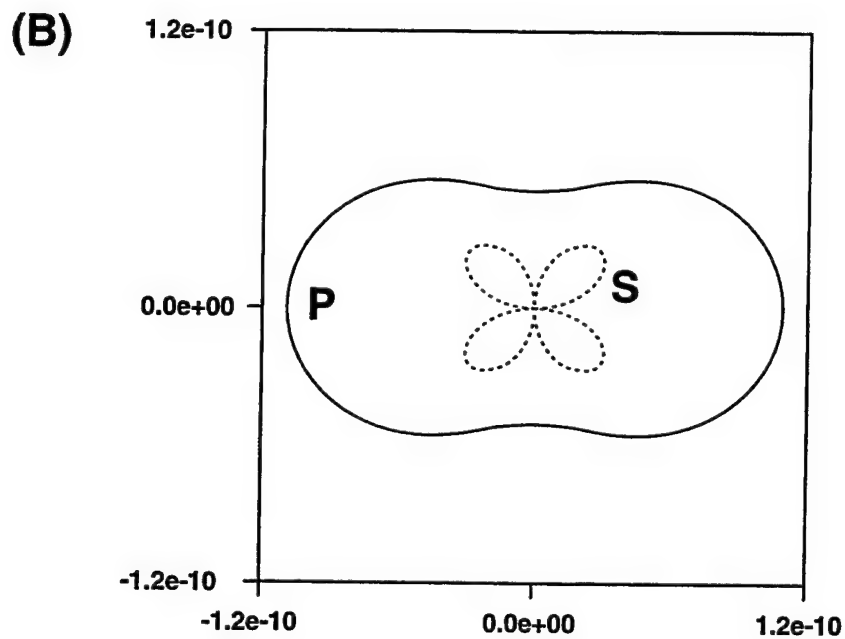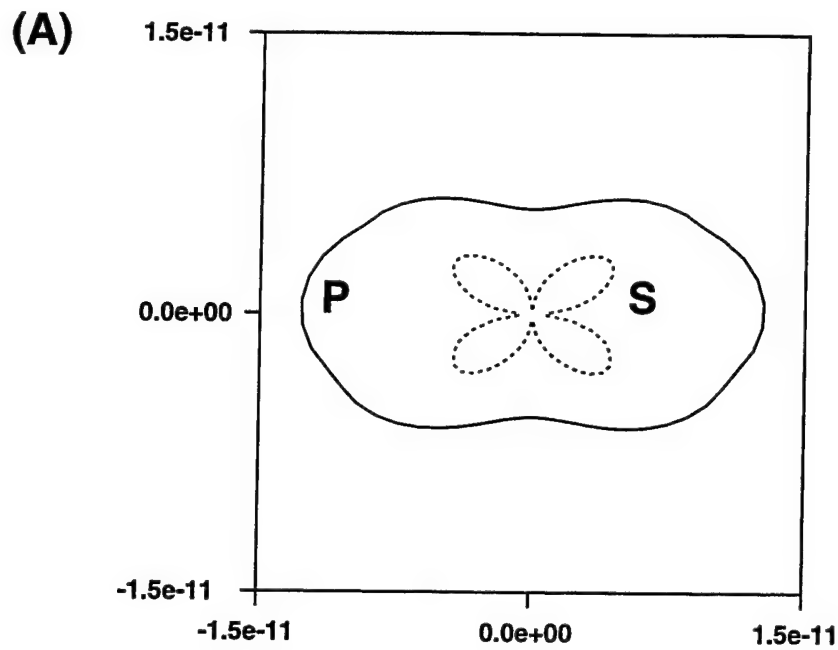
Figure 7: High frequency radiation patterns of the (A) instantaneous pressurization and (B) point source sources in a cavity of aspect ratio 5 located inside the hard rock isotropic formation (length 40 m, radius 4 m). The cavity is oriented vertically in the figure. This figure shows the amplitude variation in synthetic seismograms computed using a source having a step function time dependence, including frequencies up to 100 Hz.
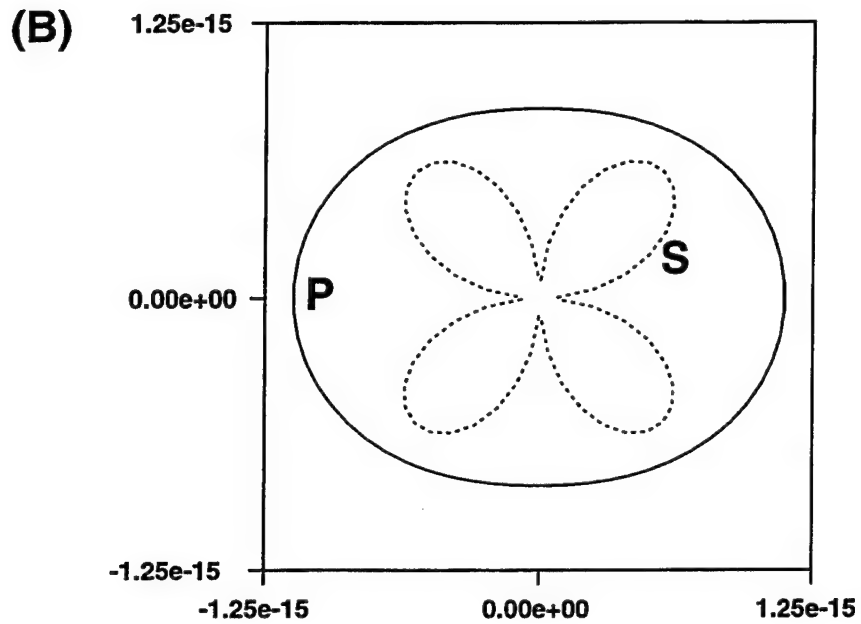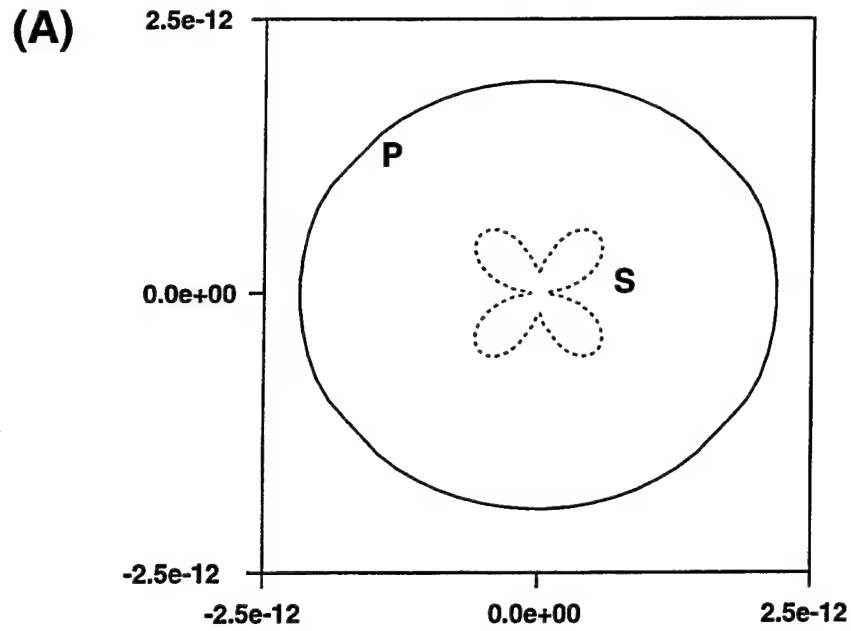
Figure 8: Low frequency radiation patterns of the (A) instantaneous pressurization and (B) point source sources in a cavity of aspect ratio 5 located inside the hard rock isotropic formation (length 40 m, radius 4 m). The cavity is oriented vertically in the figure. This figure shows the amplitude variation in synthetic seismograms computed using a Ricker wavelet with a dominant frequency of 1 Hz.
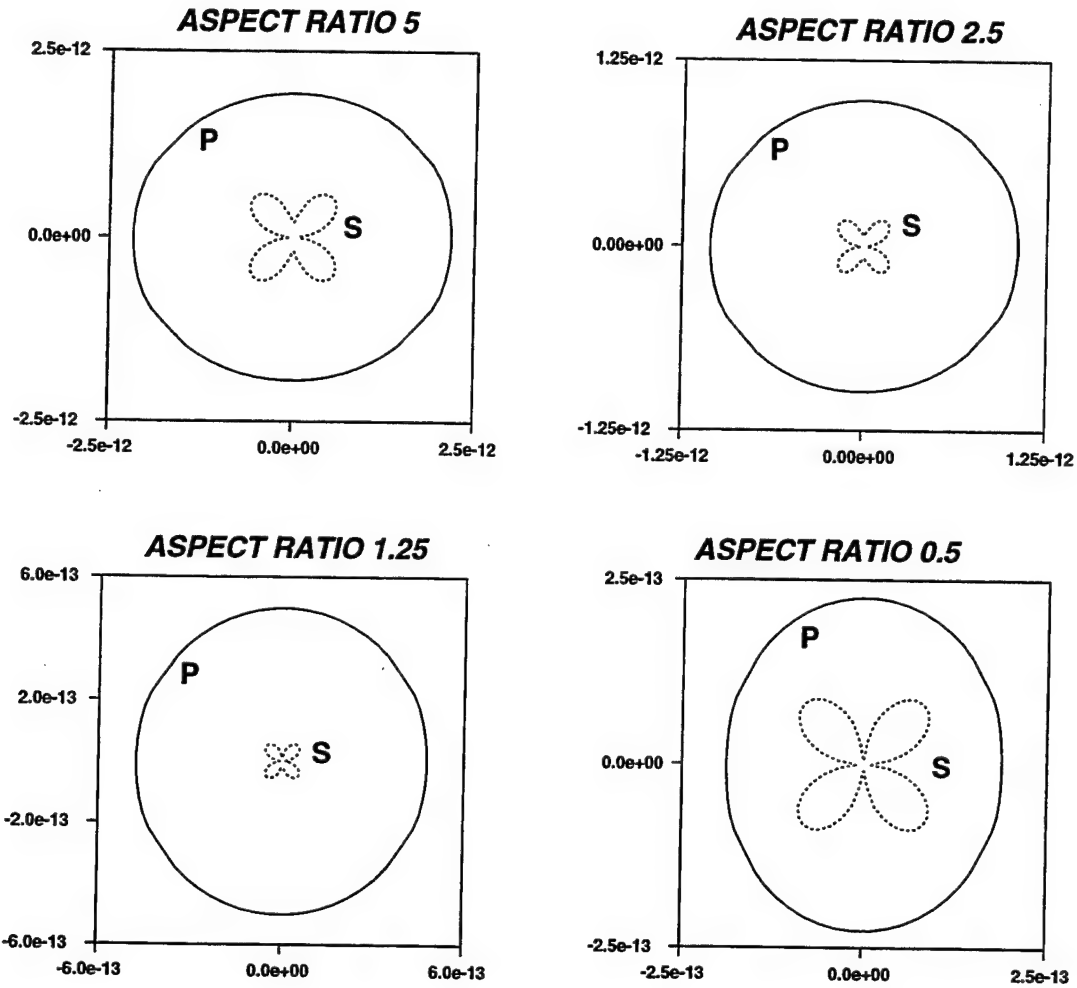
Figure 9: Radiation patterns for the instantaneous pressurization model in cavities located in the hard rock isotropic formation (velocities in Figure 2). In all cases, the cavity length was 40 m, and it is oriented vertically in the figures. The frequency domain results were convolved with a Ricker wavelet of 1 Hz to simulate the frequency ranges seen at regional distances.
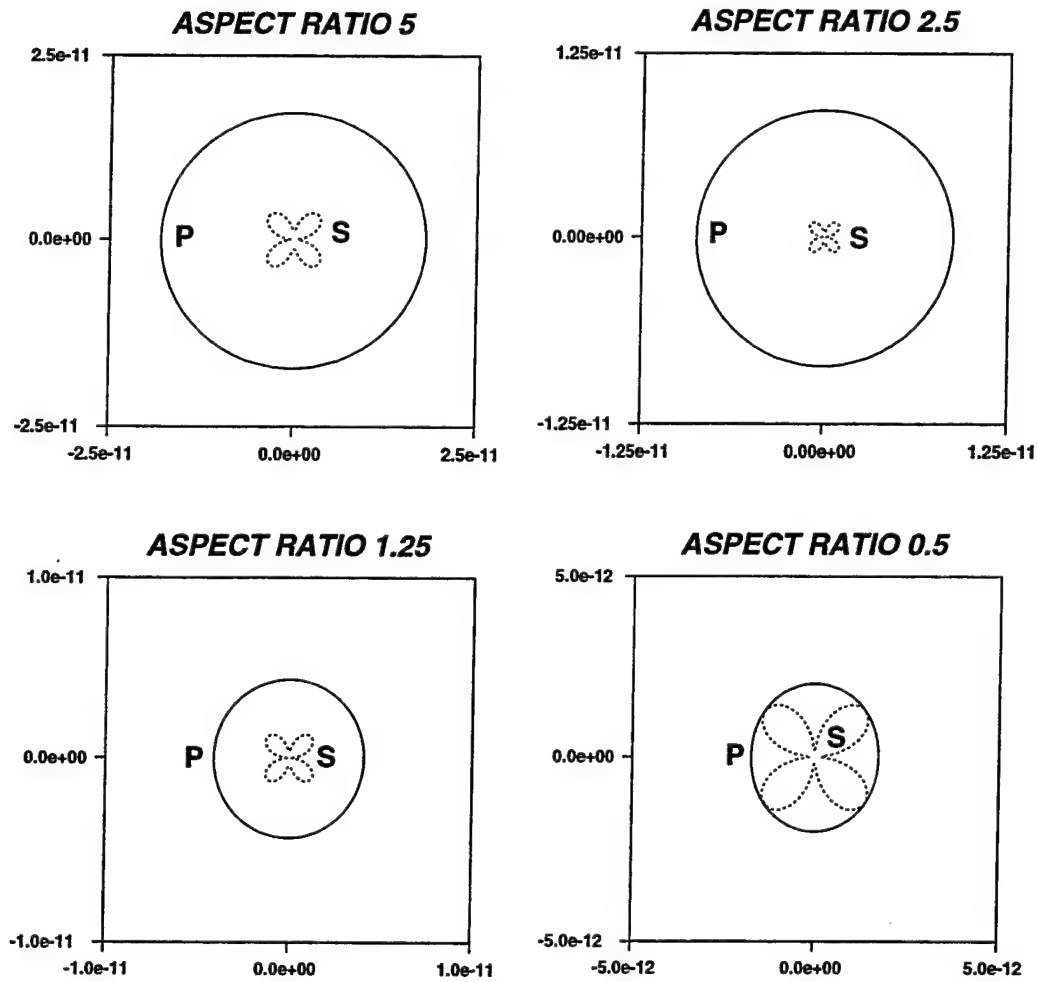
67

Figure 10: Radiation patterns for the low velocity isotropic shale. The figure format and cavity dimensions are as in Figure 9. Note that the range of values on the axes has been chosen to facilitate direction comparison with results for the analogous anisotropic shale (Figure 15). P-wave velocity of this soft rock formation is 2290 m/s, S-wave velocity is 980 m/s and density is 2250 kg/m^3.
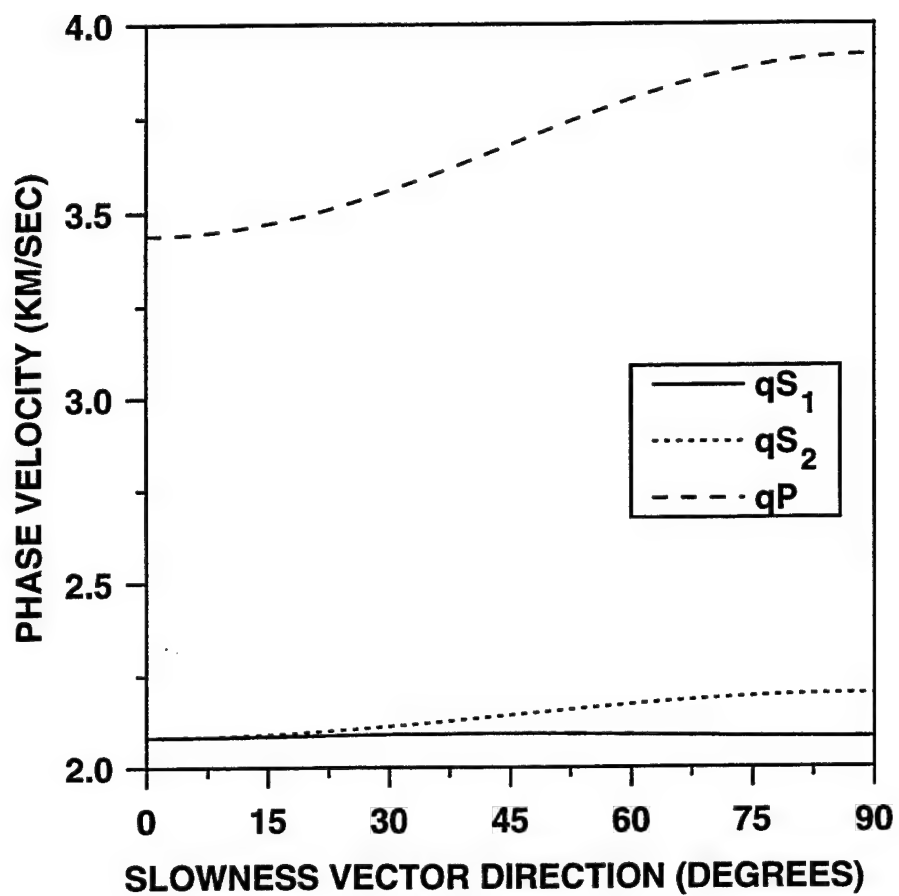
68

Figure 11: Phase velocities of the fractured, transversely isotropic medium with elastic constants in Table 1. The angle of the slowness vector is measured from the z−axis, the axis of symmetry of the medium.
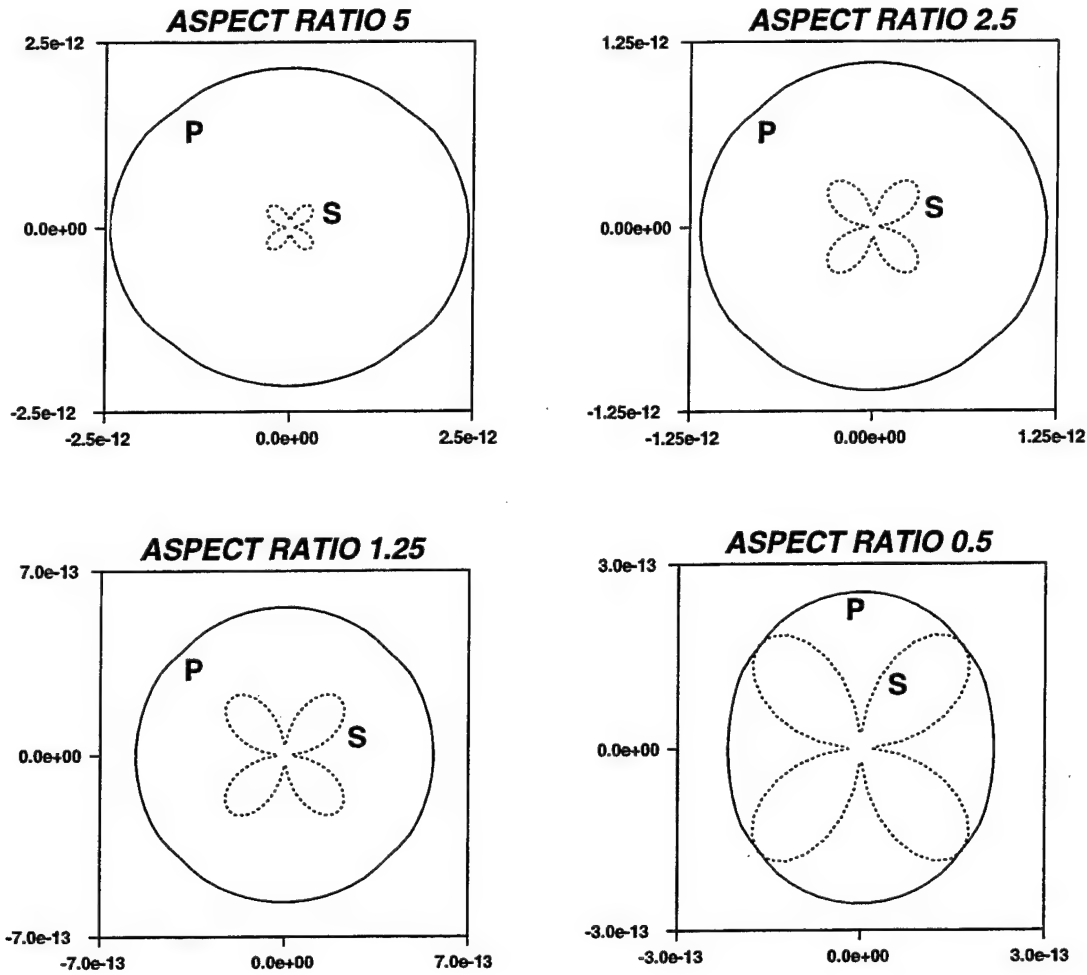
Figure 12: Radiation patterns for the instantaneous pressurization source model located in the fractured, transversely isotropic formation. Aspect ratio of the cavity was varied as indicated in the figure. Medium parameters for the material surrounding the cavity are given in Table 1. Note that the fractures are aligned perpendicular to the cavity. Because the background elastic constants used to compute the elastic constants for the medium were those of the isotropic formation considered above, a comparison of these radiation patterns with those in Figure 9 shows the influence of aligned fractures on the generation of quasi-compressional and quasi-shear wave energy by the explosion source.
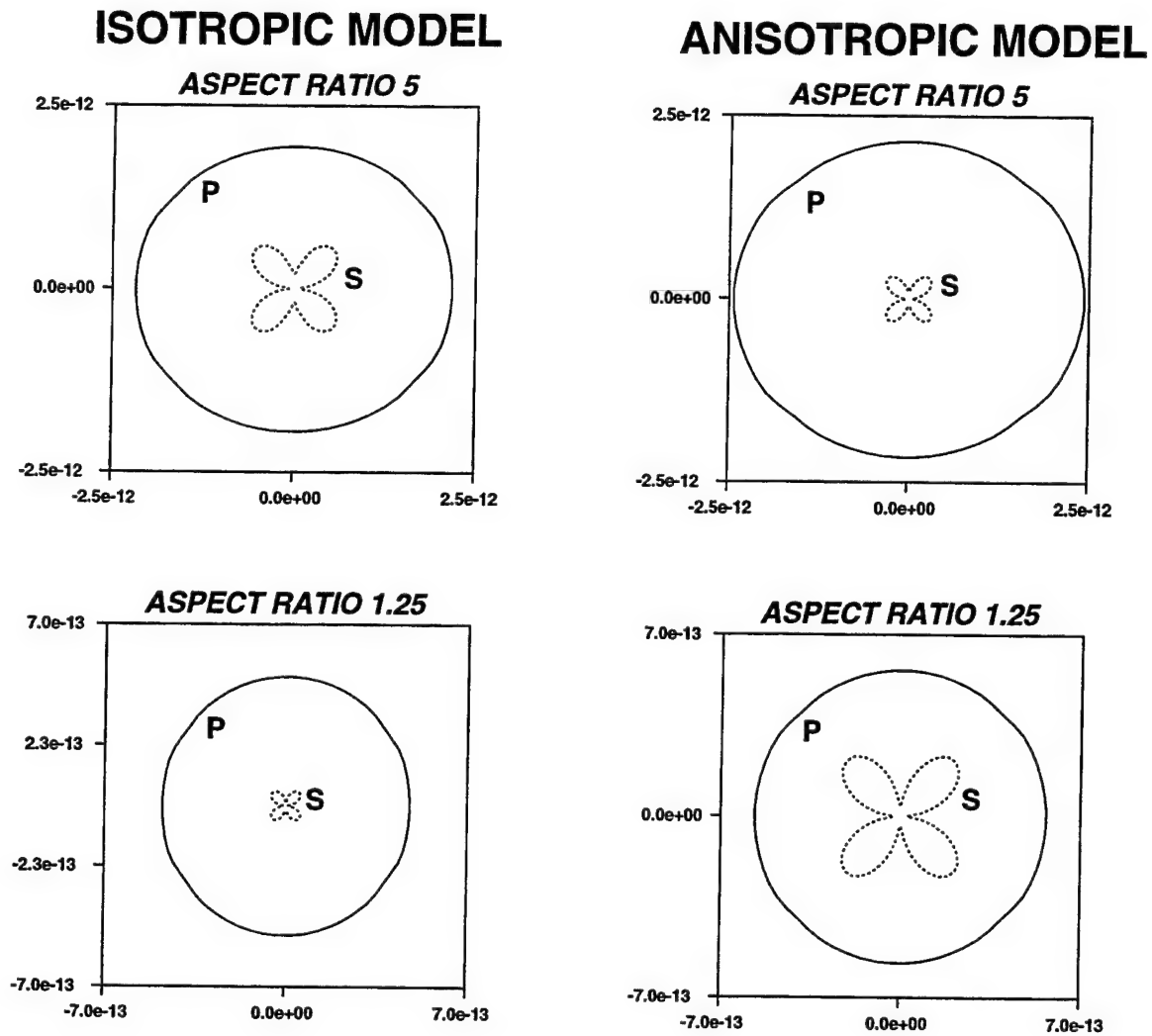
ISOTROPIC MODEL

ANISOTROPIC MODEL

Figure 13: Comparison of radiation patterns in isotropic hard rock formation (left) and anisotropic, fractured equivalent (right).
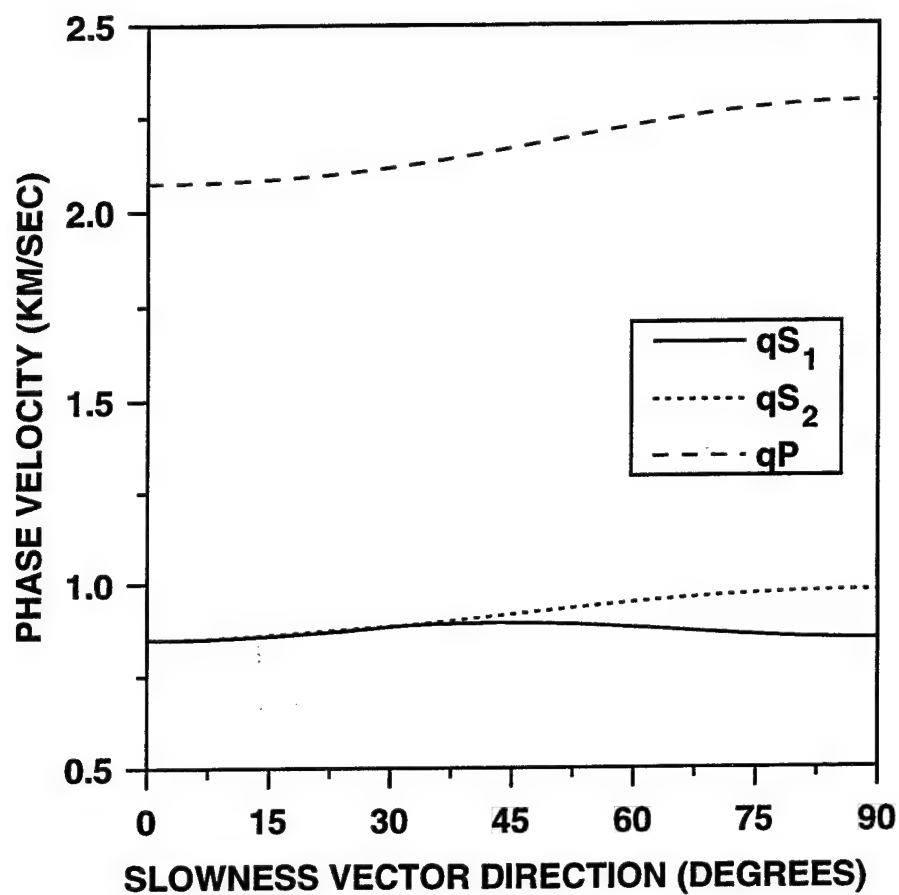
71

Figure 14: Phase velocity variation in the transversely isotropic Pierre shale. Elastic constants were estimated by White et al. (1983) using VSP data (see Table 2). The angle of the slowness vector is measured from the $z-$axis, the axis of symmetry.
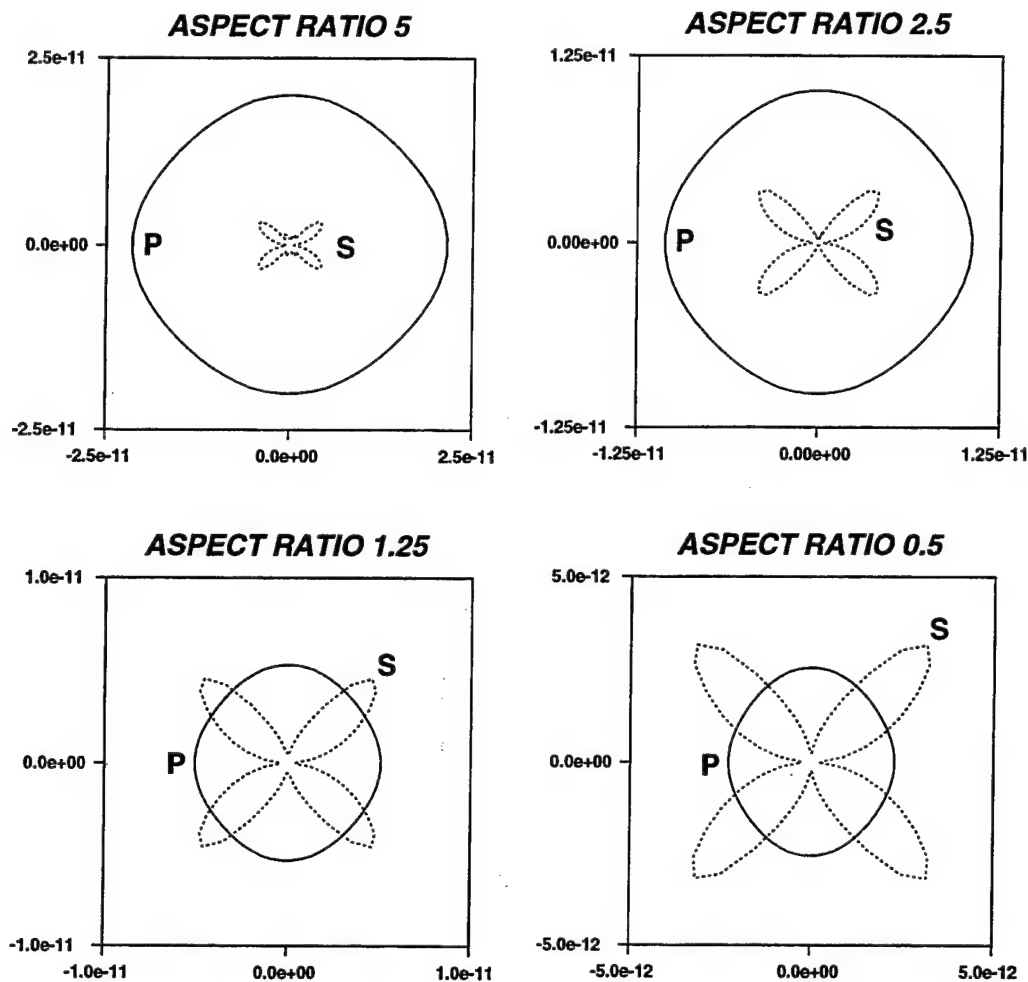
Figure 15: Radiation patterns for the instantaneous pressurization source model located in cavities insie the Pierre Shale. Aspect ratio of the 40 m long cavity varied as shown in the figure. Medium properties are specified in Table 2.
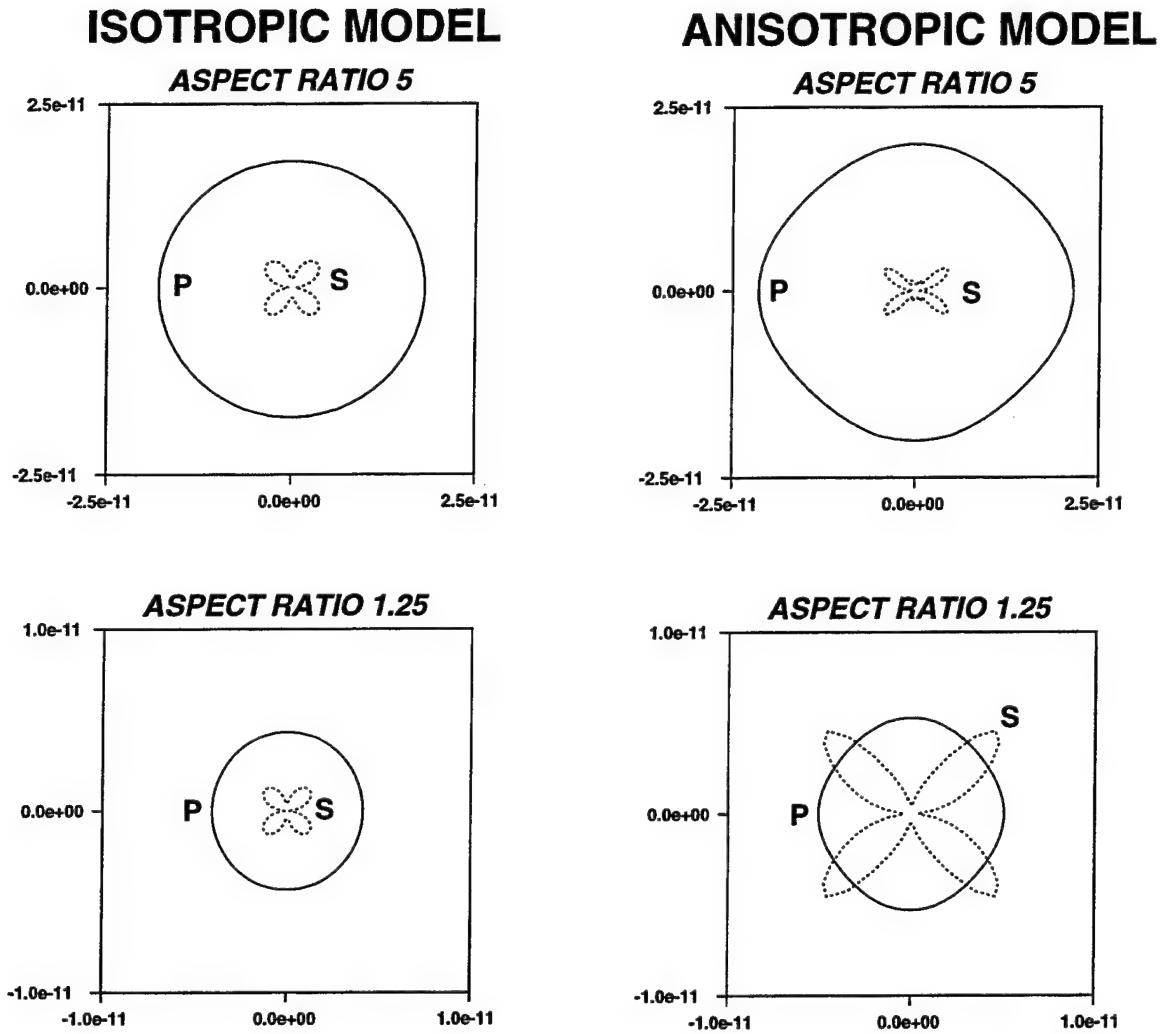
Figure 16: Comparison of radiation patterns in isotropic low velocity formation formation (left) and anisotropic shale (right). The velocities in the isotropic formation (P-wave velocity 2290 m/s, S-wave velocity 980 m/s) are of the same general magnitude as those in the anisotropic shale (see Figure 14).

74

THOMAS AHRENS
SEISMOLOGICAL LABORATORY 252-21
CALIFORNIA INSTITUTE OF TECHNOLOGY
PASADENA, CA 91125

RALPH ALEWINE
NTPO
1901 N. MOORE STREET, SUITE 609
ARLINGTON, VA 22209

SHELTON ALEXANDER
PENNSYLVANIA STATE UNIVERSITY
DEPARTMENT OF GEOSCIENCES
537 DEIKE BUILDING
UNIVERSITY PARK, PA 16801

MUAWIA BARAZANGI
INSTITUTE FOR THE STUDY OF THE CONTINENTS
3126 SNEE HALL
CORNELL UNIVERSITY
ITHACA, NY 14853

RICHARD BARDZELL
ACIS
DCI/ACIS
WASHINGTON, DC 20505

T.G. BARKER
MAXWELL TECHNOLOGIES
P.O. BOX 23558
SAN DIEGO, CA 92123

DOUGLAS BAUMGARDT
ENSCO INC.
5400 PORT ROYAL ROAD
SPRINGFIELD, VA 22151

THERON J. BENNETT
MAXWELL TECHNOLOGIES
11800 SUNRISE VALLEY DRIVE SUITE 1212
RESTON, VA 22091

WILLIAM BENSON
NAS/COS
ROOM HA372
2001 WISCONSIN AVE. NW
WASHINGTON, DC 20007

JONATHAN BERGER
UNIVERSITY OF CA, SAN DIEGO
SCRIPPS INSTITUTION OF OCEANOGRAPHY IGPP, 0225
9500 GILMAN DRIVE
LA JOLLA, CA 92093-0225

ROBERT BLANDFORD
AFTAC
1300 N. 17TH STREET
SUITE 1450
ARLINGTON, VA 22209-2308

STEVEN BRATT
NTPO
1901 N. MOORE STREET, SUITE 609
ARLINGTON, VA 22209

RHETT BUTLER
IRIS
1616 N. FORT MEYER DRIVE
SUITE 1050
ARLINGTON, VA 22209

LESLIE A. CASEY
DOE
1000 INDEPENDENCE AVE. SW
NN-40
WASHINGTON, DC 20585-0420

CATHERINE DE GROOT-HEDLIN
SCRIPPS INSTITUTION OF OCEANOGRAPHY
UNIVERSITY OF CALIFORNIA, SAN DIEGO
INSTITUTE OF GEOPHYSICS AND PLANETARY PHYSICS
LA JOLLA, CA 92093

STANLEY DICKINSON
AFOSR
110 DUNCAN AVENUE, SUITE B115
BOLLING AFB
WASHINGTON, D.C. 20332-001

SEAN DORAN
ACIS
DCI/ACIS
WASHINGTON , DC 20505

DIANE I. DOSER
DEPARTMENT OF GEOLOGICAL SCIENCES
THE UNIVERSITY OF TEXAS AT EL PASO
EL PASO, TX 79968

RICHARD J. FANTEL
BUREAU OF MINES
DEPT OF INTERIOR, BLDG 20
DENVER FEDERAL CENTER
DENVER, CO 80225

JOHN FILSON
ACIS/TMG/NTT
ROOM 6T11 NHB
WASHINGTON, DC 20505

1

MARK D. FISK
MISSION RESEARCH CORPORATION
735 STATE STREET
P.O. DRAWER 719
SANTA BARBARA, CA 93102-0719

LORI GRANT
MULTIMAX, INC.
311C FOREST AVE. SUITE 3
PACIFIC GROVE, CA 93950

I. N. GUPTA
MULTIMAX, INC.
1441 MCCORMICK DRIVE
LARGO, MD 20774

JAMES HAYES
NSF
4201 WILSON BLVD., ROOM 785
ARLINGTON, VA 22230

MICHAEL HEDLIN
UNIVERSITY OF CALIFORNIA, SAN DIEGO
SCRIPPS INSTITUTION OF OCEANOGRAPHY IGPP, 0225
9500 GILMAN DRIVE
LA JOLLA, CA 92093-0225

EUGENE HERRIN
SOUTHERN METHODIST UNIVERSITY
DEPARTMENT OF GEOLOGICAL SCIENCES
DALLAS, TX 75275-0395

VINDELL HSU
HQ/AFTAC/TTR
1030 S. HIGHWAY A1A
PATRICK AFB, FL 32925-3002

RONG-SONG JIH
PHILLIPS LABORATORY
EARTH SCIENCES DIVISION
29 RANDOLPH ROAD
HANSCOM AFB, MA 01731-3010

LAWRENCE LIVERMORE NATIONAL LABORATORY
ATTN: TECHNICAL STAFF (PLS ROUTE)
PO BOX 808, MS L-200
LIVERMORE, CA 94551

LAWRENCE LIVERMORE NATIONAL LABORATORY
ATTN: TECHNICAL STAFF (PLS ROUTE)
PO BOX 808, MS L-221
LIVERMORE, CA 94551

ROBERT GEIL
DOE
PALAIS DES NATIONS, RM D615
GENEVA 10, SWITZERLAND

HENRY GRAY
SMU STATISTICS DEPARTMENT
P.O. BOX 750302
DALLAS, TX 75275-0302

DAVID HARKRIDER
PHILLIPS LABORATORY
EARTH SCIENCES DIVISION
29 RANDOLPH ROAD
HANSCOM AFB, MA 01731-3010

THOMAS HEARN
NEW MEXICO STATE UNIVERSITY
DEPARTMENT OF PHYSICS
LAS CRUCES, NM 88003

DONALD HELMBERGER
CALIFORNIA INSTITUTE OF TECHNOLOGY
DIVISION OF GEOLOGICAL & PLANETARY SCIENCES
SEISMOLOGICAL LABORATORY
PASADENA, CA 91125

ROBERT HERRMANN
ST. LOUIS UNIVERSITY
DEPARTMENT OF EARTH & ATMOSPHERIC SCIENCES
3507 LACLEDE AVENUE
ST. LOUIS, MO 63103

ANTHONY IANNACCHIONE
BUREAU OF MINES
COCHRANE MILL ROAD
PO BOX 18070
PITTSBURGH, PA 15236-9986

THOMAS JORDAN
MASSACHUSETTS INSTITUTE OF TECHNOLOGY
EARTH, ATMOSPHERIC & PLANETARY SCIENCES
77 MASSACHUSETTS AVENUE, 54-918
CAMBRIDGE, MA 02139

LAWRENCE LIVERMORE NATIONAL LABORATORY
ATTN: TECHNICAL STAFF (PLS ROUTE)
PO BOX 808, MS L-207
LIVERMORE, CA 94551

LAWRENCE LIVERMORE NATIONAL LABORATORY
ATTN: TECHNICAL STAFF (PLS ROUTE)
LLNL
PO BOX 808, MS L-175
LIVERMORE, CA 94551

LAWRENCE LIVERMORE NATIONAL LABORATORY
ATTN: TECHNICAL STAFF (PLS ROUTE)
PO BOX 808, MS L-208
LIVERMORE, CA 94551

LAWRENCE LIVERMORE NATIONAL LABORATORY
ATTN: TECHNICAL STAFF (PLS ROUTE)
PO BOX 808, MS L-202
LIVERMORE, CA 94551

LAWRENCE LIVERMORE NATIONAL LABORATORY
ATTN: TECHNICAL STAFF (PLS ROUTE)
PO BOX 808, MS L-195
LIVERMORE, CA 94551

LAWRENCE LIVERMORE NATIONAL LABORATORY
ATTN: TECHNICAL STAFF (PLS ROUTE)
PO BOX 808, MS L-205
LIVERMORE, CA 94551

THORNE LAY
UNIVERSITY OF CALIFORNIA, SANTA CRUZ
EARTH SCIENCES DEPARTMENT
EARTH & MARINE SCIENCE BUILDING
SANTA CRUZ, CA 95064

ANATOLI L. LEVSHIN
DEPARTMENT OF PHYSICS
UNIVERSITY OF COLORADO
CAMPUS BOX 390
BOULDER, CO 80309-0309

DONALD A. LINGER
DNA
6801 TELEGRAPH ROAD
ALEXANDRIA, VA 22310

LOS ALAMOS NATIONAL LABORATORY
ATTN: TECHNICAL STAFF (PLS ROUTE)
PO BOX 1663, MS F659
LOS ALAMOS, NM 87545

LOS ALAMOS NATIONAL LABORATORY
ATTN: TECHNICAL STAFF (PLS ROUTE)
PO BOX 1663, MS F665
LOS ALAMOS, NM 87545

LOS ALAMOS NATIONAL LABORATORY
ATTN: TECHNICAL STAFF (PLS ROUTE)
PO BOX 1663, MS D460
LOS ALAMOS, NM 87545

LOS ALAMOS NATIONAL LABORATORY
ATTN: TECHNICAL STAFF (PLS ROUTE)
PO BOX 1663, MS C335
LOS ALAMOS, NM 87545

GARY MCCARTOR
SOUTHERN METHODIST UNIVERSITY
DEPARTMENT OF PHYSICS
DALLAS, TX 75275-0395

KEITH MCLAUGHLIN
MAXWELL TECHNOLOGIES
P.O. BOX 23558
SAN DIEGO, CA 92123

BRIAN MITCHELL
DEPARTMENT OF EARTH & ATMOSPHERIC SCIENCES
ST. LOUIS UNIVERSITY
3507 LACLEDE AVENUE
ST. LOUIS, MO 63103

RICHARD MORROW
USACDA/IVI
320 21ST STREET, N.W.
WASHINGTON, DC 20451

JOHN MURPHY
MAXWELL TECHNOLOGIES
11800 SUNRISE VALLEY DRIVE SUITE 1212
RESTON, VA 22091

JAMES NI
NEW MEXICO STATE UNIVERSITY
DEPARTMENT OF PHYSICS
LAS CRUCES, NM 88003

JOHN ORCUTT
INSTITUTE OF GEOPHYSICS AND PLANETARY PHYSICS
UNIVERSITY OF CALIFORNIA, SAN DIEGO
LA JOLLA, CA 92093

PACIFIC NORTHWEST NATIONAL LABORATORY
ATTN: TECHNICAL STAFF (PLS ROUTE)
PO BOX 999, MS K6-48
RICHLAND, WA 99352

PACIFIC NORTHWEST NATIONAL LABORATORY
ATTN: TECHNICAL STAFF (PLS ROUTE)
PO BOX 999, MS K7-34
RICHLAND, WA 99352

PACIFIC NORTHWEST NATIONAL LABORATORY
ATTN: TECHNICAL STAFF (PLS ROUTE)
PO BOX 999, MS K6-40
RICHLAND, WA 99352

PACIFIC NORTHWEST NATIONAL LABORATORY
ATTN: TECHNICAL STAFF (PLS ROUTE)
PO BOX 999, MS K7-22
RICHLAND, WA 99352

PACIFIC NORTHWEST NATIONAL LABORATORY
ATTN: TECHNICAL STAFF (PLS ROUTE)
PO BOX 999, MS K5-72
RICHLAND, WA 99352

PACIFIC NORTHWEST NATIONAL LABORATORY
ATTN: TECHNICAL STAFF (PLS ROUTE)
PO BOX 999, MS K6-84
RICHLAND, WA 99352

PACIFIC NORTHWEST NATIONAL LABORATORY
ATTN: TECHNICAL STAFF (PLS ROUTE)
PO BOX 999, MS K5-12
RICHLAND, WA 99352

FRANK PILOTTE
HQ/AFTAC/TT
1030 S. HIGHWAY A1A
PATRICK AFB, FL 32925-3002

KEITH PRIESTLEY
DEPARTMENT OF EARTH SCIENCES
UNIVERSITY OF CAMBRIDGE
MADINGLEY RISE, MADINGLEY ROAD
CAMBRIDGE, CB3 0EZ UK

JAY PULLI
RADIX SYSTEMS, INC.
6 TAFT COURT
ROCKVILLE, MD 20850

PAUL RICHARDS
COLUMBIA UNIVERSITY
LAMONT-DOHERTY EARTH OBSERVATORY
PALISADES, NY 10964

DAVID RUSSELL
HQ AFTAC/TTR
1030 SOUTH HIGHWAY A1A
PATRICK AFB, FL 32925-3002

CHANDAN SAIKIA
WOOODWARD-CLYDE FEDERAL SERVICES
566 EL DORADO ST., SUITE 100
PASADENA, CA 91101-2560

SANDIA NATIONAL LABORATORY
ATTN: TECHNICAL STAFF (PLS ROUTE)
DEPT. 5704
MS 0979, PO BOX 5800
ALBUQUERQUE, NM 87185-0979

SANDIA NATIONAL LABORATORY
ATTN: TECHNICAL STAFF (PLS ROUTE)
DEPT. 5791
MS 0567, PO BOX 5800
ALBUQUERQUE, NM 87185-0567

SANDIA NATIONAL LABORATORY
ATTN: TECHNICAL STAFF (PLS ROUTE)
DEPT. 9311
MS 1159, PO BOX 5800
ALBUQUERQUE, NM 87185-1159

SANDIA NATIONAL LABORATORY
ATTN: TECHNICAL STAFF (PLS ROUTE)
DEPT. 5704
MS 0655, PO BOX 5800
ALBUQUERQUE, NM 87185-0655

SANDIA NATIONAL LABORATORY
ATTN: TECHNICAL STAFF (PLS ROUTE)
DEPT. 5736
MS 0655, PO BOX 5800
ALBUQUERQUE, NM 87185-0655

THOMAS SERENO JR.
SCIENCE APPLICATIONS INTERNATIONAL
CORPORATION
10260 CAMPUS POINT DRIVE
SAN DIEGO, CA 92121

AVI SHAPIRA
SEISMOLOGY DIVISION
THE INSTITUTE FOR PETROLEUM RESEARCH AND
GEOPHYSICS
P.O.B. 2286, NOLON 58122 ISRAEL

ROBERT SHUMWAY
410 MRAK HALL
DIVISION OF STATISTICS
UNIVERSITY OF CALIFORNIA
DAVIS, CA 95616-8671

MATTHEW SIBOL
ENSCO, INC.
445 PINEDA COURT
MELBOURNE, FL 32940

DAVID SIMPSON
IRIS
1616 N. FORT MEYER DRIVE
SUITE 1050
ARLINGTON, VA 22209

BRIAN SULLIVAN
BOSTON COLLEGE
INSITUTE FOR SPACE RESEARCH
140 COMMONWEALTH AVENUE
CHESTNUT HILL, MA 02167

NAFI TOKSOZ
EARTH RESOURCES LABORATORY, M.I.T.
42 CARLTON STREET, E34-440
CAMBRIDGE, MA 02142

GREG VAN DER VINK
IRIS
1616 N. FORT MEYER DRIVE
SUITE 1050
ARLINGTON, VA 22209

TERRY WALLACE
UNIVERSITY OF ARIZONA
DEPARTMENT OF GEOSCIENCES
BUILDING #77
TUCSON, AZ 85721

JAMES WHITCOMB
NSF
NSF/ISC OPERATIONS/EAR-785
4201 WILSON BLVD., ROOM785
ARLINGTON, VA 22230

JIAKANG XIE
COLUMBIA UNIVERSITY
LAMONT DOHERTY EARTH OBSERVATORY
ROUTE 9W
PALISADES, NY 10964

OFFICE OF THE SECRETARY OF DEFENSE
DDR&E
WASHINGTON, DC 20330

TACTEC
BATTELLE MEMORIAL INSTITUTE
505 KING AVENUE
COLUMBUS, OH 43201 (FINAL REPORT)

PHILLIPS LABORATORY
ATTN: GPE
29 RANDOLPH ROAD
HANSCOM AFB, MA 01731-3010

JEFFRY STEVENS
MAXWELL TECHNOLOGIES
P.O. BOX 23558
SAN DIEGO, CA 92123

DAVID THOMAS
ISEE
29100 AURORA ROAD
CLEVELAND, OH 44139

LAWRENCE TURNBULL
ACIS
DCI/ACIS
WASHINGTON, DC 20505

FRANK VERNON
UNIVERSITY OF CALIFORNIA, SAN DIEGO
SCRIPPS INSTITUTION OF OCEANOGRAPHY IGPP, 0225
9500 GILMAN DRIVE
LA JOLLA, CA 92093-0225

DANIEL WEILL
NSF
EAR-785
4201 WILSON BLVD., ROOM 785
ARLINGTON, VA 22230

RU SHAN WU
UNIVERSITY OF CALIFORNIA SANTA CRUZ
EARTH SCIENCES DEPT.
1156 HIGH STREET
SANTA CRUZ, CA 95064

JAMES E. ZOLLWEG
BOISE STATE UNIVERSITY
GEOSCIENCES DEPT.
1910 UNIVERSITY DRIVE
BOISE, ID 83725

DEFENSE TECHNICAL INFORMATION CENTER
8725 JOHN J. KINGMAN ROAD
FT BELVOIR, VA 22060-6218 (2 COPIES)

PHILLIPS LABORATORY
ATTN: XPG
29 RANDOLPH ROAD
HANSCOM AFB, MA 01731-3010

PHILLIPS LABORATORY
ATTN: TSML
5 WRIGHT STREET
HANSCOM AFB, MA 01731-3004

5

PHILLIPS LABORATORY
ATTN: PL/SUL
3550 ABERDEEN AVE SE
KIRTLAND, NM 87117-5776 (2 COPIES)